

DISS. ETH NO. 27836

**DECIPHERING THE ASSEMBLY OF MITOCHONDRIAL
RIBOSOMAL LARGE SUBUNIT**

A thesis submitted to attain the degree of
DOCTOR OF SCIENCES of ETH ZURICH

(Dr. sc. ETH Zurich)

presented by

MATEUSZ JASKOŁOWSKI

*M.Sc., Biotechnology
University of Gdańsk, Poland*

born on *15.05.1991*

citizen of Poland

accepted on the recommendation of

*Prof. Dr. Nenad Ban
Prof. Dr. Rudolf Glockshuber
Prof. Dr. Raimund Dutzler*

2021

I dedicate this thesis to my parents

Joanna and Jacek

and to my brother

Marcin

Preface and acknowledgments

*“Men wanted for hazardous journey...
...Small wages. Bitter cold. Long months of complete darkness. Constant
danger. Safe return doubtful. Honour and recognition in case of success.”*

*Newspaper advertisement popularly attributed to
Sir Ernest Henry Shackleton for one of his Antarctic Expeditions.*

For me, science is a passion. A hobby that can be done for a living. A way to explore the unexplored and an adventure to discover and understand the unknown. This is probably why the above-mentioned quote resonates with me so strongly. I saw it for the first time on the website of the Ban laboratory and although I was already excited by the group’s research, the message made me want to join it all the more.

According to my parents, I have always been hard to convince and constantly questioned everything. That is probably the reason why I am so attracted to structural biology. After all, seeing is believing, right? Structural biology plays a crucial role in understanding the way that proteins work and in drug and therapeutic design. I am grateful for the opportunity to work in this field.

I thank Prof. Dr. Nenad Ban for giving me a chance to do doctoral work in his laboratory. I believe that challenging projects and the independent nature of the work in his group made me a better scientist. While difficult at times, it shaped me to think and plan for myself and to ask mindful questions. I also would like to thank Prof. Dr. Rudi Glockshuber and Prof. Dr. Raimund Dutzler for being members of my doctoral committee and their guidance throughout my PhD.

I think I would not make it that far without my previous experience from Prof. Dr. Tony Kossiakoff laboratory at the University of Chicago, where I performed a practical part of my Master’s thesis. I had an immense pleasure to work there under the supervision of not only Prof. Kossiakoff but also Dr. Elena Davydova and Dr. Luke Bailey, who showed me what it means to pursue science with passion and shaped me as a young scientist.

Prof. Nenad Ban laboratory was a perfect fit for me. A friendly atmosphere and awesome people made me feel at home immediately. Big thanks to Dr. Ahamd Jomaa who has been a great colleague and a friend, a person with whom I could share exciting results late at night and discuss career possibilities on Saturdays spent in the lab. It was a pleasure working with Ahmad and a great privilege to get to know him for

the last few years. I am sure we will stay in touch long after leaving the Ban laboratory. On a similar note, I would like to thank Dr. Simone Mattei who joined the lab later in my PhD, but showed great support for my project from the very beginning. We shared the same room and, fortunately enough, the same sense of humor. It has been a delight to work with him, especially in more challenging moments, as we could always find a reason to laugh. Besides joking around and having silly conversations, we also had serious talks about science, academic career and the scientific community. This thesis would also not be possible without Dr. Tea Lenarčič. I joined Tea's project and had a blast working together. Never before have I had so much fun while working under pressure on a time-sensitive and highly competitive project. The shared sense of humor, related cultures and linguistic similarities (although not so obvious at times!) made a fun combination and a great friend. I would also like to thank Dr. Marc Leibundgut with whom I work on a particularly challenging, long and at times, frustrating, project. His expertise and experience were welcome and greatly appreciated. I also appreciate all the career advice he gave me during our occasional coffee talks. Gratitude to Dr. Daniel Boerhringer who trained me on the FEI Morgani and FEI Tecnai F20 transmission electron microscopes and special thanks to Dr. Philipp Bieri for support and help during my PhD thesis. Big thanks to all other present and former members of the Ban laboratory: Alain Scaiola for patience, help with Linux computing and a great deal of laughter; Denis Yudin for insightful, although sometimes lengthy, scientific conversations; Dr. Eva Krummer for insights into the academic career; Katharina Schubert, Tanja Schönhut, Blanca Echeverria and Adrian Bothe for being part of the fun H2 group; Dr. Min Jin; Anne Ries; Martin Saurer; Pramod Bhatt; Armin Piccioni; Dr. David Ramrath; Dr. Christopher S. Aylett; Dr. Jendrik Hentschel; Dr. Melanie Weisser; Sonja Rutz, Viktorija Sukyte, Simon Eitzinger, Remo Jost, Claudia Zurcher and all the others with whom I crossed paths.

And at the end, big thank you to the people who made me who I am today - my family and my friends. My parents, Joanna and Jacek, and their love and continued support. For their patience with me in my youth and insightful advice in my adulthood. To my brother, Marcin, who is always there, who supports me and motivates me to do better. And to my friends; Rafał Zdanowicz and Paweł Joachimiak, best friends since university together; Dawid Żyła and Sara Przytocka, with whom I could go full-polish and nobody judged; Silvia Napolitano and Gianluca Janka, my traveling buddies and

Ola Fergin, with whom I could always grab a burger and a beer or go for a movie with an over-priced popcorn.

Gratitude to many others who have made my life in Zurich and my PhD studies a whole lot better!

Table of Contents

Preface and acknowledgments	V
Table of Contents	IX
Summary	XIII
Zusammenfassung	XV
Introduction	1
Structure and function of the ribosome.....	1
Ribosomes are macromolecules that perform protein synthesis.....	1
Ribosomes are composed of RNA and proteins	3
Mitochondria retained their ribosome	4
Despite common origin structures of mitochondrial ribosomes differ significantly	6
Maturation of the ribosome.....	8
Information required for the assembly of both subunits is encoded in the	
ribosomal components.....	9
Maturation of the ribosome <i>in vivo</i> occurs much faster and involves many	
assembly factors.....	12
Current understanding of the bacterial ribosome assembly.....	15
Mitoribosome assembly is subject of intense investigation	18
Aim of the thesis.....	21
Chapter 1. Structural insights into the mechanism of mitoribosomal large subunit	
biogenesis.....	23
Statement of contribution	23
Summary.....	25
Introduction	26
Results	28
Cryo-EM analysis of trypanosomal mitoribosomes reveals two native assembly	
intermediates of the large subunit.....	28
Comparison of the assembly intermediates suggests the order of maturation ..	31
GTPases form a network of interactions.....	33
mt-LAF2 is a DEAD-box helicase that interacts with the 12S rRNA.....	37
Maturation of the peptidyl transferase center involves multiple assembly factors	
.....	39
A methyltransferase binds to a conserved site of rRNA modification in the A-loop	
.....	42
A novel ACP-LYRm module binds and changes the conformation of the L1 stalk	
.....	43

Discussion	44
Acknowledgments	48
Author contributions	48
Declaration of interests.....	48
STAR★Methods	49
Key Resources Table	49
Resource Availability	50
Experimental Model and Subject Details	51
Method Details	51
References	58
Supplemental Information	63
Chapter 2. Stepwise maturation of the peptidyl transferase region of human mitoribosomes.....	73
Statement of contribution	73
Abstract	75
Introduction	76
Results	77
Structure of assembly intermediates of the human mitoribosomal large subunit77	
NSUN4-MTERF4 stabilizes rRNA in a conformation that exposes the active site region.....	78
MRM2 methylates the U3039 in the A loop before it adopts mature conformation	80
MTG2 and NSUN4 interact with the P loop in a tweezer-like manner.....	81
Stepwise maturation of the human mitochondrial large subunit.....	84
Methods	85
References	92
Supplementary materials.....	95
Conclusions and future perspectives.....	105
Mitoribosome maturation is both similar to and different from the bacterial ribosome assembly.....	105
Cryo-EM revolutionized the field of structural biology	107
Cryo-EM has potential to position structural biology at the frontline of molecular biology	108
There are still aspects of cryo-EM that can be improved	109
Subtomogram averaging cryo-ET allows for structural investigation of protein complexes without the need for purification.....	110

The future of structural biology is full of exciting possibilities	111
Appendix I	112
Cryo-electron microscopy.....	112
Invention and the design of electron microscope.....	112
Single particle cryo-EM.....	115
Use of cryo-EM and its limitations.....	117
References	118
Curriculum vitae	135

Summary

Ribosome is a universally conserved macromolecular machine responsible for protein synthesis. It is a ribonucleoprotein complex composed of two subunits and built of multiple proteins and ribosomal RNAs. The small subunit decodes the information stored within the messenger RNA (mRNA) whereas the large subunit catalyses the peptide bond formation in a growing polypeptide. Despite being universally conserved, ribosome composition differs significantly between prokaryotes and eukaryotes.

Interestingly, eukaryotes possess more than one type of ribosomes. Beside the cytoplasmic ones, they also contain ribosomes specific to mitochondria (and chloroplasts, in case of plants). Mitochondria are double-membrane bounded cellular organelles that originated from α -proteobacteria in an endosymbiotic event and play a crucial role in production of cellular chemical energy and regulation of cellular metabolism. Mitochondrial ribosomes (mitoribosomes) are required for a proper function of mitochondria and defects in mitoribosomes are associated with a range of severe disorders in humans.

Despite sharing a common ancestor, the structure of mitoribosomes differs significantly from their bacterial counterparts. In general, they contain a larger number of proteins, often specific to a given organism, and their ribosomal RNA is either reduced (humans and trypanosomes) or extended (fungi and plants). Nevertheless, the architecture of the ribosomes and the key functional regions in both subunits remain virtually unchanged and are similar to those observed in the bacterial ribosome.

Assembly of ribosomes is a crucial and complex process that involves multiple steps and components. Over the years it has been studied both in bacteria and eukaryotes. However, our understanding on the mitoribosome assembly is still lacking. In my thesis I investigated the process of mitoribosome assembly by determining multiple structures of mitoribosomal large subunit assembly intermediates from *Homo sapiens* as well as human parasite *Trypanosoma brucei*. The structures reveal numerous assembly factors and explain their mechanism of action. In conclusion, results presented in this thesis provide structural insights into the complex and biomedically relevant process of mitoribosome assembly.

Zusammenfassung

Das Ribosom ist ein universell konserviertes Makromolekül und ist für die Proteinbiosynthese verantwortlich. Der proteinribonukleare Komplex besteht aus zwei Untereinheiten, die aus verschiedenen Proteinen und ribosomalen RNAs aufgebaut sind. Die kleine Untereinheit entschlüsselt die in der Boten- oder *messenger*-RNA (mRNA) gespeicherten Informationen, während die große Untereinheit die Bildung der Peptidbindung im wachsenden Polypeptid katalysiert. Obwohl Ribosomen universell konserviert sind, unterscheidet sich die Ribosomenzusammensetzung im Detail signifikant zwischen den Prokaryoten und Eukaryoten.

Interessanterweise besitzen Eukaryoten mehr als eine Art von Ribosomen. Sie enthalten neben den zytoplasmatischen auch solche Ribosomen, welche spezifisch für Mitochondrien (und im Fall von Pflanzen Chloroplasten) sind. Mitochondrien sind doppelmembranbegrenzte Zellorganelle, die in einem endosymbiotischen Ereignis aus α -Proteobakterien hervorgegangen sind. Sie spielen eine entscheidende Rolle bei der Produktion von zellulärer chemischer Energie und der Regulierung des Zellstoffwechsels. Mitochondriale Ribosomen (Mitoribosomen) sind für eine ordnungsgemäße Funktion der Mitochondrien erforderlich, und Defekte der Mitoribosomen werden mit einer Reihe schwerer Erkrankungen beim Menschen in Verbindung gebracht.

Obwohl sie einen gemeinsamen Vorfahren haben, unterscheidet sich die Struktur der Mitoribosomen erheblich von ihren bakteriellen Gegenstücken. Generell enthalten sie eine größere Anzahl von Proteinen, oft spezifisch für einen bestimmten Organismus, und ihre ribosomale RNA ist entweder reduziert (Mensch und Trypanosomen) oder erweitert (Pilze und Pflanzen). Dennoch bleiben die Architektur der Ribosomen und die wichtigsten funktionellen Regionen in beiden Untereinheiten praktisch unverändert und ähneln denen in bakteriellen Ribosomen.

Der Zusammenbau von Ribosomen ist ein entscheidender und komplexer Prozess, der mehrere Schritte und Komponenten umfasst. Im Laufe der Jahre wurde dieser sowohl in Bakterien als auch in Eukaryoten untersucht. Allerdings fehlt uns ein Verständnis über den Zusammenbau von Mitoribosomen. In meiner Dissertation untersuchte ich den Prozess der Mitoribosomen-Assemblierung, indem ich mehrere Strukturen von mitoribosomalen Zwischenprodukten der Assemblierung großer Untereinheiten von *Homo sapiens* sowie dem humanen Parasiten *Trypanosoma*

brucei ermittelte. Die Strukturen offenbaren zahlreiche Assemblierungsfaktoren und erklären deren Wirkmechanismus. Zusammenfassend geben die in dieser Dissertation präsentierten Ergebnisse strukturelle Einblicke in den komplexen und biomedizinisch relevanten Prozess der Mitoribosomen-Assemblierung.

Introduction

Structure and function of the ribosome

Proteins are one of the main “building blocks” of life on Earth. They fulfill a variety of different roles in cells where they act as structural components, transporters, messengers, enzymes, antibodies and more. Made of amino acids linked together by a peptide bond, they can vary significantly in size, from small ones built of several dozen amino acids and a molecular weight of around 5 kilodaltons (5 kDa) to enormous ones that are composed of thousands of amino acids, with molecular weight measured in millions of daltons (MDa). The biggest known protein is titin. Made of more than 34 thousand amino acids, it has a molecular weight of approximately 3.8 MDa. It is one of the main components of human muscles and accounts for ~10% of their protein mass. Consequently, an average adult human carries approximately 0.5 kg of titin¹.

Ribosomes are macromolecules that perform protein synthesis

Most of the proteins are synthesized by the ribosome, a protein-RNA complex that plays a crucial role in translation during which the genetic information is translated into the sequence of amino acids linked by peptide bonds. Ribosomes were observed for the first time in 1955 by George Emil Palade who used electron microscopy to visualize the inside of a eukaryotic cell and described ribosomes as “small particulate components of the cytoplasm”². Palade’s description of the cellular architecture was one of the most important findings in the field of cell biology at that time, for which Palade was awarded the Nobel Prize in Physiology or Medicine in 1974, together with Albert Claude and Christian de Duve. Improvements in biochemical and biophysical methods over the following years enabled scientists to discover the role of ribosomes in protein synthesis and investigate their structure and function.

Using approaches such as comparative DNA sequence analysis, differential centrifugation and small-angle X-ray scattering, it was shown that the ribosome is composed of ribosomal RNA (rRNA) and proteins (hence called ribosomal proteins, r-proteins)³⁻⁶. Position of the individual ribosomal proteins on the ribosome has been studied using r-protein specific antibodies and immuno-electron microscopy^{7,8}, chemical cross-linking⁹ and neutron scattering¹⁰. The size of a fully assembled

ribosome was deduced from negative stain electron microscopy to be approximately 200 Å, while its eukaryotic counterpart was measured at 250-300 Å¹¹. Although beneficial for the general visualization of the ribosome, negative stain electron microscopy has its drawbacks and cannot be used to obtain detailed structural information¹².

At that time, however, x-ray crystallography was widely used for structure determination of various proteins and biological macromolecules with great success. X-ray crystallography is a method that enables visualization of a protein structure at atomic resolution by analyzing a diffraction pattern recorded after a crystallized molecule is exposed to an x-ray beam. Noteworthy, growing a protein crystal is not a trivial task. It requires high concentration of homogeneous sample and enormous efforts in finding the right crystallization conditions, which, among others, include sample concentration, buffer composition and temperature. Usually the only way to find the right conditions for crystallization is through screening methods. It is often at this stage that a project with an aim to elucidate a structure of a given protein fails. In addition, ribosomes themselves, due to their nature, represented an immense challenge for X-ray crystallography. Their heterogeneous character of a complex composed of rRNA and proteins as well as relatively high flexibility required for its function made the task of growing crystals even more difficult. Furthermore, because of its size, ribosomes create massive symmetry units, which makes phasing the X-ray diffraction pattern exceptionally difficult. It took great effort and time to obtain the first ribosome crystals^{13,14}. Even after that, it took another 13 years of optimization and phasing calculations to produce X-ray crystallographic maps that led to an atomic structure of the bacterial small subunit at 3 Å¹⁵ and the large subunit at 2.4 Å¹⁶. In 2009, Venkatraman Ramakrishnan, Thomas A. Steitz and Ada E. Yonath received the Nobel Prize in Chemistry “for studies of the structure and function of the ribosome”.

At that time, single particle cryo electron microscopy (cryoEM) was also used for structure determination. Described in greater detail in appendix 1, this method is based on illuminating isolated biological molecules or assemblies embedded within a layer of vitreous ice with a beam of accelerated electrons. Obtained images of individual protein complexes represent 2D projections and can be used, with a help of computer algorithms, to reconstruct a 3D map of the studied complex, however, at that time reconstructions in the mid-range resolution of approximately 8 Å were possible¹⁷⁻²⁰. In recent years cryo-electron microscopy became the dominant method in structural

biology for high resolution structure determination of large cellular assemblies, including ribosomes. The advances, fueled by the improved direct detectors for recording micrographs and more advanced computational tools, now allow for structure determination of very heterogeneous and flexible samples. Therefore, all structural investigations of mitoribosomal assembly intermediates presented in this thesis were carried out using cryo-EM.

Ribosomes are composed of RNA and proteins

Ribosomes are present in all known kingdoms of life, but their composition varies depending on the organism. Nevertheless, all ribosomes are composed of two subunits - small and large. Ribosome and their subunits are often referred to by their sedimentation coefficient under high g-force (gravitational force equivalent) expressed

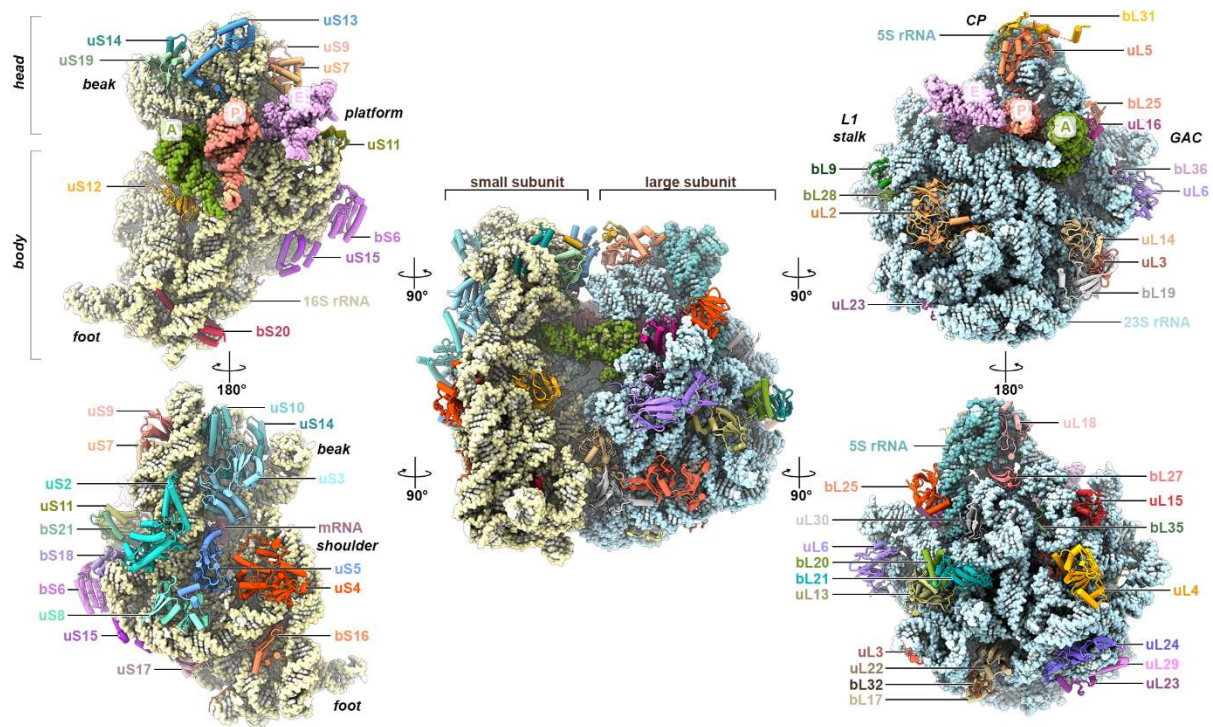


Figure 1. Structure of a bacterial ribosome.

Atomic structure of a bacterial ribosome together with the three tRNAs is shown in the middle. Both subunits are indicated. Small subunit as seen from the intersubunit side is presented on the top left together with the solvent exposed side shown below. Similarly, the large subunit is displayed on the right, with the intersubunit and solvent exposed view shown on top and bottom, respectively. All proteins are colored and labeled individually. SSU 16S rRNA is presented in beige, LSU 23S rRNA in light blue and 5S rRNA in dark cyan. mRNA is colored orchid and the A-, P- and E-site tRNAs, labeled as A, P and E, are shown in green, salmon and plum respectively. The displayed structure is a chimaera of a complete ribosome with A- and P-site tRNA (PDB:7K00) and E-site tRNA from PDB:5UQ7.

in Svedberg unit (S). In *Escherichia coli*, the small subunit (30S) is composed of 16S rRNA molecule (1540 nucleotides) and 21 ribosomal proteins. In contrast, the large subunit (50S) is composed of two rRNAs, 23S and 5S (2904 and 120 nucleotides, respectively) and 33 ribosomal proteins. The two subunits associate to form the ribosome with a sedimentation coefficient of 70S in bacteria (**Figure 1**). In eukaryotes, the small subunit (40S) is comprised of a rRNA (18S, 1869 nucleotides in *H. sapiens*) and 33 ribosomal proteins, while large subunit (60S) is made of three rRNA molecules (28S, 5.8S and 5S; 5070, 156 and 120 nucleotides in *H. sapiens*, respectively) and 46 ribosomal proteins. The eukaryotic ribosome is termed 80S.

Even though the composition of the ribosome varies depending on the organism, the architectural organization remains the same. The small subunit can be divided into a head and a body region, which can be further subdivided into the shoulder, platform and foot. The region between the body and the head domain is often referred to as the neck. The large subunit has a crown shape with a ridge part on which a central protuberance (CP) and two stalks are located (L1 and bL12) (**Figure 1**).

The most fundamental functions of ribosomal subunits are highly conserved. The small subunit binds and deciphers messenger RNA (mRNA), while the large subunit binds amino-acylated transfer RNAs (tRNAs) and catalyses the peptide bond formation. Ribosomes produce proteins with an high fidelity and efficiency by incorporating, for example in *E. coli*, 15 amino acids per second into a growing polypeptide chain²¹.

Mitochondria retained their ribosome

Mitochondria are double-membrane bounded cellular organelles in which the aerobic respiration takes place, producing energy in the form of ATP. They are present in all eukaryotic organisms, except for one known exception of *Monocercomonoides exilis*, an amitochondrial eukaryote²². In addition to the energy conversion that takes place in mitochondria, it has also been shown that other crucial processes that are essential for the cell prosperity and survival also take place in mitochondria. These include biosynthesis of macromolecule precursors, catabolization of nutrients, maintenance of redox homeostasis and metabolic waste management (reviewed in

Spinellin and Haigis, 2018²³). It is therefore not surprising that properly functioning mitochondria are of crucial importance for the eukaryotic organism²⁴.

Under a light microscope, mitochondria appear as homogeneous bodies separated from the rest of the cytoplasm. A more detailed structure of the mitochondria was described by G. E. Palade in 1953²⁵, just two years before he discovered the cytoplasmic ribosomes. Using electron microscopy and newly developed sample preparation and staining techniques, he was able to visualize the double-membrane organization of the mitochondria and cristae on the inner membrane. Intriguingly, few years later it was shown that mitochondria are able to incorporate amino acids into proteins²⁶. Even though the exact function of the already discovered ribosomes was still not known at that time, it was nevertheless proposed that the protein synthesis in mitochondria is carried out by ribosomes similar to those observed in cytoplasm²⁷. Visual proof of mitochondrial specific ribosomes came few years later, when ribosome-like particles and DNA components were observed by electron microscope within the mitochondria of yeast, chicken, mouse and human HeLa cells²⁸. It did not take long to purify and analyze ribosomes of mitochondria from fungi²⁹ and mammals³⁰. At the same time, the endosymbiotic theory for the evolution of mitochondria, proposed initially at the beginning of the 20th century, gained interest again³¹ (**Figure 2**). Today, results of thousands of sequencing and proteomics data of eukaryotic organisms clearly show that the mitochondria have an α -proteobacterial origin³², although their exact phylogenetic position among the α -proteobacterial species is still a matter of debate³³.

Evolution of mitochondria involved notable reduction of their genome, with most of the genes either lost or transferred into the nuclear genome. Proteomics data show that only 10-20% of proteins within the mitochondria originated from the α -proteobacteria³⁴. Moreover, studies of multiple unicellular, multicellular, photosynthetic and anaerobic eukaryotes have shown that the mitochondrial genome and proteome evolved independently in different eukaryotic organisms³⁴. As a result of such divergence, on one side there are members of jakobid genera that possess the most ancestral mitochondrial genome known to date which encodes more than 65 proteins³⁵ and on the other side *Plasmodium falciparum*, with the smallest known mitochondrial genome that encodes just 3 proteins³⁶. In turn, human mitochondria contain 13 protein genes, all encoding enzymes of an oxidative phosphorylation (OXPHOS) metabolic pathway³⁷.

The ENDOSYMBIOTIC THEORY

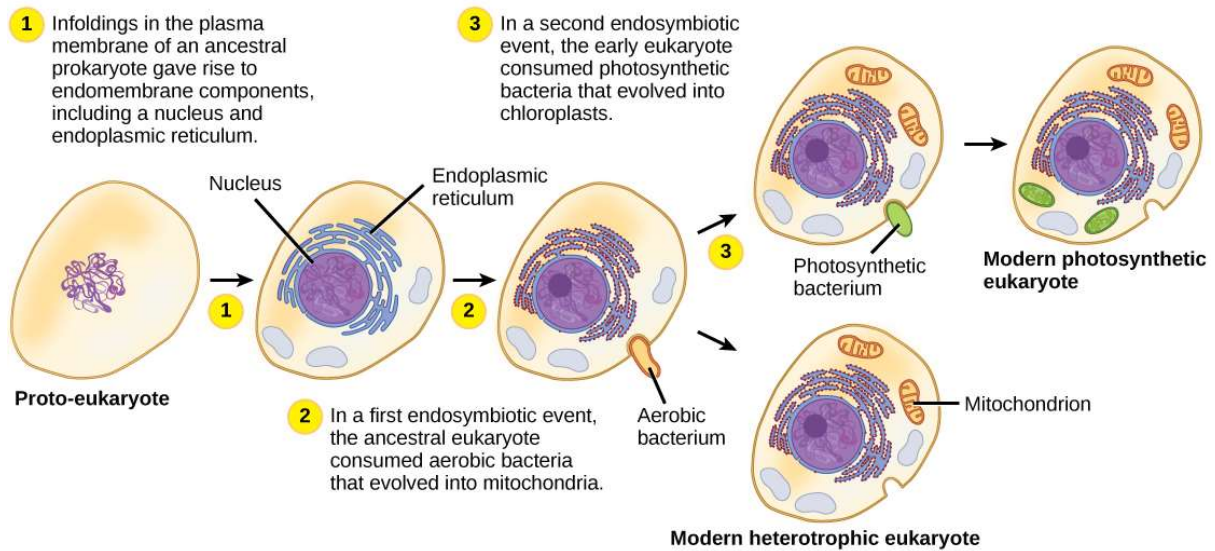


Figure 2. The endosymbiotic theory explains the origin of mitochondria and chloroplasts.

According to the endosymbiotic theory eukaryotes originated from an ancestral prokaryote that underwent membrane proliferation and infolding, leading to compartmentalization and creation of a nucleus and an endoplasmic reticulum. Next, in a first endosymbiotic event, these cells engulfed aerobic prokaryotes and established an endosymbiotic relationship with them, which led to mitochondria and origin of modern heterotrophic eukaryotes. Modern photosynthetic eukaryotes originated from a second endosymbiotic event, when early eukaryotes consumed a photosynthetic bacterium, which led to chloroplasts. Image by Phil Schatz, CC BY-SA 4.0 <<https://creativecommons.org/licenses/by-sa/4.0/>>, via Wikimedia Commons.

Despite common origin structures of mitochondrial ribosomes differ significantly

Although the number of protein genes within the mitochondrial genome varies, the ribosomal RNA of the mitochondrial ribosome (mitoribosome) is always encoded by the mitochondrial DNA. However, as mentioned above, majority of the mitoribosomal proteins are encoded within the nuclear genome and therefore need to be imported into the mitochondria after translation on the cytoplasmic ribosomes. Such evolution of the mitochondrial genome and the resulting need to coordinate the transcription of the rRNA within mitochondria with the translation and import of mitoribosomal proteins from the cytoplasm also affected the architecture of the mitoribosome. Initial biochemical studies that analyzed the mitoribosome had already shown that it is composed of shorter rRNAs and has a different sedimentation value as compared to its bacterial counterpart³⁰. Interestingly, just like in the case of

mitochondrial genome, mitoribosomes also differs significantly between eukaryotic organisms. First structural data of the mammalian mitoribosome obtained by cryo-EM at low resolution confirmed that reduced rRNA content appears to be partially compensated for by additional mitoribosome-specific proteins³⁸. High resolution structures obtained of the mitoribosome from mammals^{39,40}, yeast⁴¹, kinetoplastids⁴², ciliates⁴³ and plants⁴⁴ allowed for full appreciation of how distinct mitoribosomes are compared to bacterial counterparts and how remarkably divergent they are among different eukaryotic organisms (**Figure 3**).

Nevertheless, the mitoribosome is still composed of two subunits, although in some cases (trypanosomes and ciliates) the small subunit is bigger in size than the large subunit. Regardless of the size, the role of the subunits is still the same – the small subunit decodes the message on the mRNA and the large subunit catalyzes the peptide bond formation. However, mitoribosomes changed considerably in terms of composition. In general, mitoribosomes contain more proteins in comparison to the

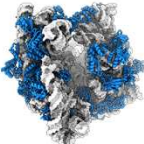
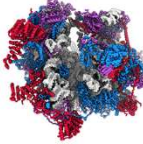
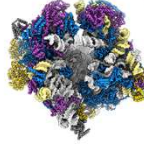
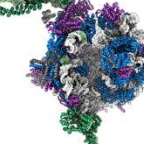
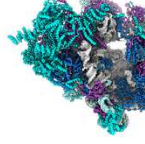

	prokaryotic ribosome	eukaryotic mitoribosome				
						
organism	<i>E. coli</i>	<i>S. scrofa</i>	<i>S. cerevisiae</i>	<i>A. thaliana</i>	<i>T. thermophila</i>	<i>T. brucei</i>
taxonomic group	bacteria	mammals	fungi	plants	ciliates	kinetoplastids
number of r-proteins	52	82	75	86	92	~122
length of rRNA	4482 nucleotides	2606 nucleotides	5021 nucleotides	4183 nucleotides	4703 nucleotides	1800 nucleotides
molecular weight	2.5 MDa	2.7 MDa	~3.3 MDa	~3.5 MDa	~4 MDa	~4.5 MDa
sedimentation coefficient	70S	55S	74S	78S	80S	50S

Figure 3. Diversity of the mitochondrial ribosome from different organisms.

Atomic models of the mature mitochondrial ribosomes together with the bacterial ribosome shown on the left. Origin and details about the composition are listed in the table. The images were generated by Eva Kummer in ChimeraX using PDB: 5MRC for *S. cerevisiae*, PDB: 6GAW for *Sus scrofa* (wild boar), PDB: 6XYW for *Brassica oleracea* and PDB: 6Z1P for *Tetrahymena thermophila*. For kinetoplastid mitoribosome, the displayed structure is a chimaera between PDB: 6HIV for the *Trypanosoma brucei* SSU and PDB:7AIH for the *Leishmania tarantolea* LSU. The ciliate mitoribosome image is based on PDB: 6Z1P. Images were used with the permission from the author.

bacterial ribosome, mostly due to the acquisition of new ribosomal proteins, often specific to a given organism. Together with the shift towards protein-rich ribosomes came the adjustment of some of the intersubunit bridges. As a consequence, several interaction points between the small and large subunit changed their character from RNA-RNA to either RNA-protein or completely protein-protein³⁸⁻⁴⁴. Besides the protein enrichment, the length of rRNA also changed. In some organisms, like humans and trypanosomes, the rRNA is significantly reduced, whereas in others, like fungi, the rRNA became longer due to notable sequence insertions (**Figure 3**). Despite these changes, the key functional regions of both subunits, namely the decoding center and the peptidyl transferase center in the small and large subunit, respectively, remained composed of RNA and are virtually unchanged in their structure.

Maturation of the ribosome

Since the discovery of ribosomes² and their role in protein synthesis they have been subject of intense investigation. The atomic structure of the bacterial ribosome^{15,16,45} together with numerous biochemical, genetic and structural studies conducted in the recent years helped us to better understand translation initiation, elongation, termination and recycling of the ribosome^{46,47}. However, equally important is the question of ribosome biogenesis. How is the ribosome efficiently assembled within the cell, especially considering its exceptional complexity?

Considering the importance of ribosomes⁴⁸, it is not surprising that about $\frac{2}{3}$ of a cell's energy is spent on ribosome production and maintenance. Furthermore, in the growing cell, where the demand on protein production is exceptionally high, ribosomes comprise up to 50% of cell mass⁴⁹ (as cited in⁵⁰). At the same time, the ribosome needs to be assembled quickly and efficiently. However, because of its dual composition and the number of components involved, ribosome maturation is not a simple process. Both the ribosomal RNA and ribosomal proteins need to be transcribed and translated, respectively. Complete ribosome in *Escherichia coli* is made of 52 ribosomal proteins and three rRNA molecules amounting to a total of 4482 nucleotides. Furthermore, the rRNA needs to fold properly and the ribosome proteins need to join the maturing subunits in the correct order and assume a correct conformation. Yet, in the exponentially growing cell with a doubling time of 30 minutes, such an elaborate complex is fully assembled in just 30 to 90 seconds⁵¹. Over the past

decades, a steady progress in understanding of the ribosome maturation has been made. Nevertheless, due to the process complexity, we still lack a comprehensive understanding of this intricate process.

Information required for the assembly of both subunits is encoded in the ribosomal components

A major progress in the understanding of the bacterial ribosome maturation was made by Traub and Nomura in 1968⁵². More than a decade after the discovery of the ribosome, yet years before any structural data, their pioneering work showed that it is possible to assemble the small ribosomal subunit *in vitro* using purified 16S rRNA and crude 30S ribosomal proteins. Their work demonstrated that the information required for the correct assembly is encoded in the molecular components themselves. In the following study⁵³, they purified each of the small subunit proteins separately and showed that it is also possible to assemble the SSU from 16S rRNA and all 30S ribosomal proteins added in a correct order, although such assembly requires higher temperature and shows lower efficiency. By changing the order in which the ribosomal proteins were added to the *in vitro* assembly, they were able to determine that the binding of the proteins to the 16S rRNA is cooperative and occurs in a sequential manner. They were also able to categorize the ribosomal proteins into primary binding proteins that are required to bind to the nascent 16S rRNA first, to stabilize its conformation and create binding sites for secondary and tertiary binding proteins. Based on these experiments an assembly map was created that shows the order of ribosomal proteins binding. The map, with small modifications, is used up to this day in the field of small subunit maturation and is often referred to as the Nomura Map **(Figure 4A)**.

From their results, Nomura and colleagues suspected that “the number of sites, per rRNA chain, which can bind ribosomal proteins independently from each other (i.e. without cooperativity) is at most two to three”⁵⁴. Later work showed that indeed three such sites exist on the 16S rRNA^{55–57}. These sites correspond to the domains of 16S rRNA, which are tightly connected to the three domains of the 30S subunit. Body domain is composed of 5' rRNA and 6 proteins⁵⁵, the platform region contains central domain of rRNA and 6 proteins⁵⁷, while the head domain is made of 3' rRNA and 8 proteins⁵⁶. Such clear organization of the SSU allows for the independent domain

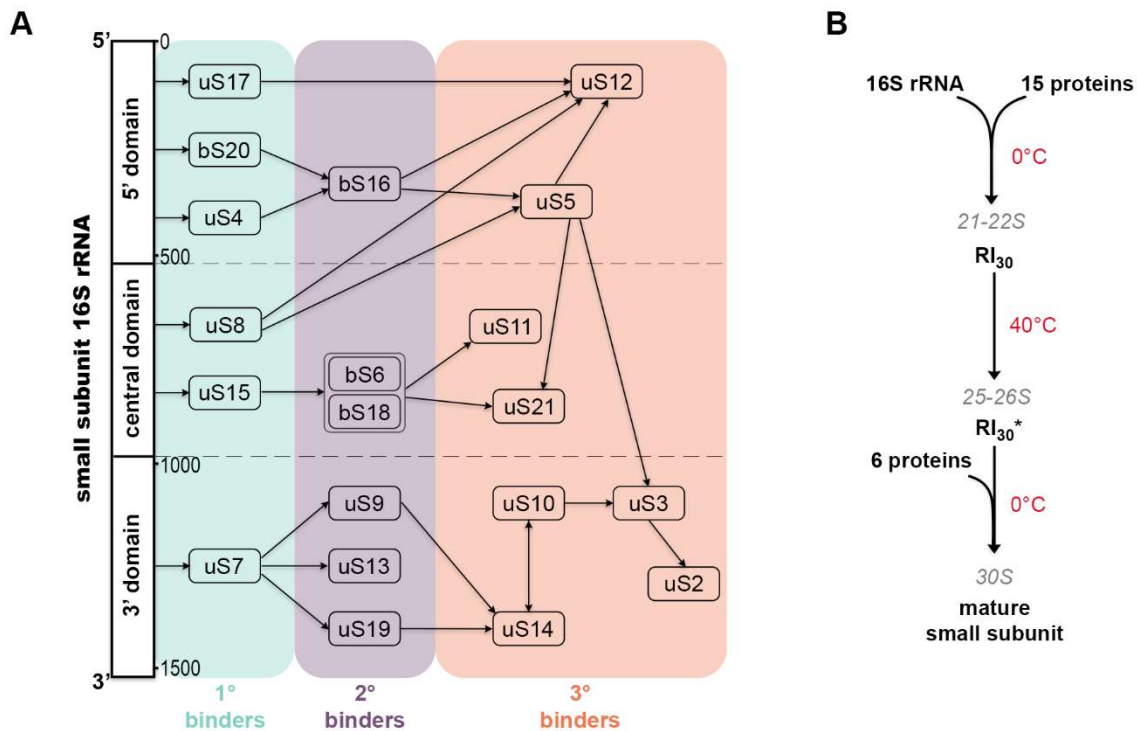


Figure 4. In vitro maturation of the bacterial small subunit.

(A) The Nomura map describing the assembly order of the bacterial small subunit. Ribosomal proteins can be divided into primary (1°), secondary (2°) and tertiary (3°) binders marked and labeled by green, purple and orange background, respectively. Three domains, which can mature independently, are also indicated with dashed lines. (B) Diagram representing the assembly of the small subunit in vitro. Particles sedimentation values at each step are depicted in grey. Temperature conditions are indicated in red.

reconstruction with each rRNA site having its specific primary binders among the ribosomal proteins (**Figure 4A**).

Interestingly, while performing the *in vitro* assembly at low temperature (0°C to 15°C) a distinct intermediate, termed reconstitution intermediate (RI), can be isolated, which sediments at 21-22S and contains 16S rRNA and 15 ribosomal proteins⁵⁴. However, RI cannot be assembled into an active SSU unless incubated at 40°C. Heating the RI is believed to cause structural rearrangements, as the newly formed RI* shows different behavior, sedimenting at 25-26S. Active 30S subunit can then be formed after addition of the remaining small subunit ribosomal protein to the RI* particles (**Figure 4B**).

As there are more components involved, determination of the steps and conditions required to reconstitute the large ribosomal subunit took more time. Fundamental work was presented in 1974 by Nierhaus and Dohme who described a

method of large subunit assembly *in vitro*⁵⁸. In contrast to the small subunit, which could be assembled in a one-step reaction in the native conditions, the large subunit assembly *in vitro* requires a two-step reaction, as well as a specific Mg^{2+} concentration and high temperature incubation. The assembly requires 23S rRNA, 5S rRNA and all large subunit ribosomal proteins⁵⁹. As in the case of the small subunit, there is no requirement for additional factors, thus the information of the 50S assembly is contained in its molecular components. Based on these experiments a map of large subunit assembly was also created, although, due to the number of components and more complex organization of the large subunit rRNA, the Nierhaus map is more intricate than the one for the small subunit (**Figure 5A**).

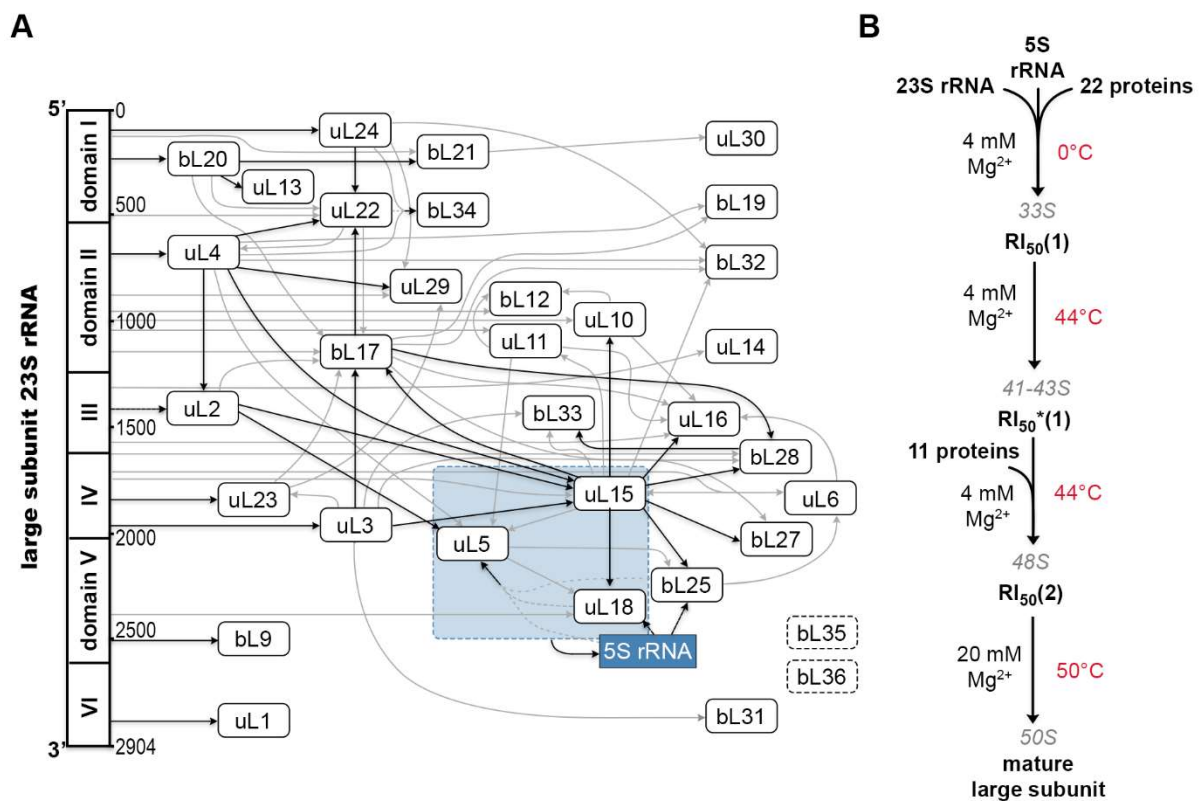


Figure 5. *In vitro* assembly of the bacterial large subunit.

(A) The Nierhaus map describing the assembly order of the bacterial large subunit. The 5S rRNA is shown with a blue background and the proteins which are necessary for its binding (uL5, uL15 and uL18) are marked with a light blue square. Black arrows indicate strong dependency, while the grey arrows indicate a weak one. Proteins presented in the dashed box (bL35 and bL36) were not included in the *in vitro* assembly. (B) Diagram representing the assembly of the small subunit *in vitro*. Particles sedimentation values at each step are written in grey. Temperature conditions are indicated in red and the Mg^{2+} concentration is indicated on the left of the arrows.

Assembly of the large subunit at low temperature yields three distinct reconstitution intermediates⁶⁰ (**Figure 5B**). First reconstitution intermediate, RI₅₀(1), is composed of two rRNA molecules, 23S and 5S, as well as 22 ribosomal proteins and sediments at 33S. At high temperatures, it transforms into a second reconstitution intermediate, RI₅₀^{*}(1), which in turn sediments at 41-43S. Upon addition of the remaining 11 proteins of the large subunit, the third reconstitution intermediate is created, RI₅₀(2). However, despite possessing all of the components of the active 50S, the RI₅₀(2) sediments at 48S and remains inactive. Only the harsh incubation at 50°C for 90 minutes at high Mg²⁺ concentration is able to transform it into an active and functional large subunit.

Maturation of the ribosome *in vivo* occurs much faster and involves many assembly factors

The ribosome assembly happens much faster *in vivo* and does not require elevated temperature or high Mg²⁺ concentration. As mentioned above, under optimal conditions, the bacterial ribosome can be assembled in just 30 seconds⁵¹. Additionally, the assembly *in vivo* is coupled with the rRNA transcription⁶¹. Both the 16S and 23S rRNA are transcribed in an immature version and possess additional nucleotides from both ends. While the pre-23S has only 3-7 and 8 nucleotides from the 5' and 3' sites, respectively, the pre-16S, termed 17S, has 115 and 33 additional nucleotides from the 5' and 3' sites, respectively. Furthermore, while the removal of additional nucleotides from pre-23S is not critical for the large subunit activity, small subunit containing non-processed 17S rRNA remains inactive^{51,62,63}. Such large differences between *in vitro* and *in vivo* assembly of course have consequences. *In vitro*, where the complete and processed rRNA is supplied, all ribosomal proteins can bind at once, while *in vivo* initially only selected binding sites for the ribosomal proteins are available as the maturation accompanies the rRNA transcription. Moreover, additional factors are necessary for rRNA cleavage and processing⁶¹. And the fact that within the cell the ribosome matures much faster than *in vitro* and does not require such harsh conditions hints at the presence of additional factors that help with the assembly. Indeed, over the years multiple trans-acting proteins have been implied to take part in the ribosome maturation⁶⁴⁻⁶⁷.

These proteins, often called assembly factors, serve different roles and their number depends on the organism. Compared to eukaryotes, which have more than

200 assembly factors⁶⁸, the prokaryotic genome encodes a comparatively small amount of assembly factors⁶⁹ (**Table 1**). However, despite the relatively low number, the exact function of some of the factors is still unclear. Based on their enzymatic activity and/or function in the ribosome maturation, all assembly factors can be divided into four groups: rRNA modifying enzymes, DEAD-box RNA helicases, ribosome dependent GTPases and general maturation factors, such as chaperones and structural factors.

Both the small and large subunit rRNAs are heavily modified. Most of the modifications occurs in the functionally important region and are strongly conserved, which implies their importance for the ribosome activity. However, our understanding of their exact function is still lacking. In *Escherichia coli*, the rRNA of the small and the large subunit undergoes 11 and 25 modifications, respectively^{69,70}. However, not all of the modifications are necessary. Krzyzosiak and colleagues showed that it is possible to assemble an active small subunit *in vitro* with an unmodified 16S rRNA⁷¹. Contrary to the 30S, at least seven modifications are required for the large subunit maturation and its activity^{72,73}. Regardless, in *Escherichia coli* at least 21 assembly factors are responsible for nucleotide modification during the ribosome maturation⁷⁴. While none of these factors are critical for cell survival, deletion of each of them causes a change in the phenotype. The current hypotheses are that the modified nucleotides act as a “molecular glue”, making sure that the functionally important regions of the ribosome retain the correct conformation, or that the modifications act as “checkpoints”, making sure that the assembly is progressing correctly.

In addition to enzymes responsible for rRNA modifications, DEAD-box helicases help unwind rRNA when it assumes a non-native secondary structure to facilitate its proper folding⁷⁵. These proteins can also act as rRNA chaperones and dissociate or rearrange RNA-protein interactions. DEAD-box helicases are characterized by a core composed of two RecA-like domains, each containing a conserved amino-acid motif aspartate, glutamate, alanine and aspartate, which in one letter code used for amino-acids reads D-E-A-D (hence the name). Proteins of that family can interact with RNA and ATP and have an RNA-dependent ATPase activity⁷⁶. They are present in all organisms and have been shown to be involved in the ribosome maturation⁷⁷. In eukaryotes their presence is necessary, while in *Escherichia coli* they are not essential, although their deletion causes a slow-growth phenotype, more pronounced at lower temperatures⁷⁸. In the ribosome maturation they are believed to

stabilize the native rRNA conformation, acting as chaperones, and unwind local rRNA secondary structures using its helicases activity⁷⁹.

While DEAD-box helicases utilize energy stored within ATP, ribosome dependent GTPases, another group of assembly factors, use GTP for their activity. Enzymes that hydrolyze GTP molecules are no stranger to the ribosome. GTPases such as EF-Tu, EF-G and IF-2 are necessary for the translation cycle of the ribosome⁴⁶. Other GTPases take part in fundamental cellular processes within the cell, like signal transduction, protein translocation and regulatory role for cell differentiation, proliferation, division and movement⁸⁰. In prokaryotes seven GTPases are involved in the ribosome assembly (**Table 1**). Despite extensive research on ribosome dependent GTPases their role in ribosome assembly is still not fully understood (reviewed in Britton, 2009⁸¹). Currently, it is hypothesized that they act as the checkpoint proteins, verifying the correctness of the ribosome assembly. It was also suggested that, because they are connected to the GTP-GDP ratio and thus the energy balance of the cell, they can halt ribosome maturation in sub-optimal conditions, where the amount of GTP molecules available to the cell is low.

Assembly of the ribosome is also dependent on other factors, which can be categorized as general maturation factors. Several studies showed that the heat shock proteins such as DnaJ, DnaK, GrpE, GroEL-GroES are involved in the ribosome maturation⁸²⁻⁸⁵. In strains with DnaJ or DnaK deletion, the assembly of the ribosome is delayed under normal conditions and completely arrested at temperatures above 42°C⁸⁶. The exact function of the heat shock proteins in the ribosome assembly is still unclear. Cold shock protein RbfA (ribosome-binding factor A) has also been implied to function as an assembly factor⁸⁷⁻⁹¹. Its role is still not fully understood, but according to several biochemical and genetical studies RbfA may be involved in several steps of small subunit maturation, aiding the 17S to 16S rRNA maturation and acting on later stages of the maturation⁹². RimM (ribosome maturation factor M) is another assembly factor that is involved in 16S rRNA maturation^{93,94}, similar to RimP (ribosome maturation factor P). Its deletion leads to decreased amount of 70S ribosome and the accumulation of small subunit containing immature 16S rRNA⁹⁵. Similar phenotype is present upon deletion of RimJ (ribosome maturation factor J)⁹⁶.

Understanding the function of assembly factors is not only interesting from the perspective of the ribosome assembly, but is also medically relevant. As some of the

assembly factors are only found in bacteria and are involved in ribosome biogenesis, critical for cell viability, they present an interesting target for new antimicrobial drugs⁶⁴.

Table 1. Assembly factors involved in the maturation of *Escherichia coli* ribosome

<i>group</i>	<i>assembly factor</i>	<i>subunit</i>	<i>reference</i>
<i>RNA modifying enzymes</i>	KsgA (RsmA)	SSU	97–100
	RsmB, RsmC, RsmD, RsmE, RsmF (YebU), RsmG	SSU	101–117
	RsuA	SSU	118–121
	RrmA (RlmA/YebH)	LSU	122–124
	RlmB, RlmC, RlmD, RlmE, RlmG, RlmL	LSU	125–137
	RluA, RluB, RluC, RluD, RluE, RluF	LSU	138–153
<i>DEAD-box helicases</i>	CsdA	LSU	154–157
	DbpA	LSU	157–164
	SrmB	LSU	165–169
	RhIE	LSU	170
<i>ribosome dependent GTPases</i>	RbgA (YlqF)	LSU	171–178
	ObgE (CgtA)	LSU	179–182
	EngB (YsxC)	LSU	183–187
	EngA (YphC / Der)	LSU	188–194
	Era	SSU	195,196
	RsgA (YjeQ)	SSU	197–205
	YqeH	SSU	206,207
<i>general maturation factors</i>	DnaK-DnaJ	SSU/LSU	83–86
	GroEL	LSU	82
	RbfA	SSU	87–92
	RimB, RimC, RimH, RimJ, RimM, RimN, RimP	SSU/ (LSU)	91,93–96,208–211
	RrmJ	LSU	212–214
	EryC	SSU/LSU	215
	YjgA	LSU	182,216
	YhbY	-	217
	YibL	-	217
	YbeB	-	217

Current understanding of the bacterial ribosome assembly

One of the first characterizations of the assembly intermediates from healthy bacterial cells comes from pulse labeling experiments, followed by sample separation on a sucrose gradient and acrylamide gel electrophoresis^{51,62,218}. These studies characterized two assembly intermediates of the small subunit and three assembly intermediates of the large subunit. They also showed that, based on the rRNA amounts, assembly intermediates account for less than 5% of all ribosomes in a growing cell. This is not a surprising result, considering that the ribosome assembles within just a few minutes⁵¹. Unfortunately, such a high speed of maturation combined

with low amount of the assembly intermediates per cell makes the task of dissecting the ribosome assembly even more challenging.

Up until recently, structural studies of the assembly intermediates were practically impossible. X-ray crystallography, the main method used for high-resolution structure determination, requires large amounts of homogeneous sample and the assembly intermediates are far from an ideal sample for that method due to their heterogeneity. However, with the recent developments in cryo-EM, the assembly intermediates at atomic resolution suddenly appeared within reach. And so, in the last few years, we witnessed an unprecedented amount of new cryo-EM maps and atomic models of assembly intermediates being reported.

One of the first studies that used cryo-EM to investigate assembly intermediates investigated small subunit particles reconstituted *in vitro* with a varying incubation times²¹⁹. This approach resulted in cryo-EM maps representing 14 distinct assembly intermediates that differed in rRNA conformation and protein composition. Although the reconstructions were limited to ~30 Å resolution, the results show that cryo-EM technique is capable of sorting multiple different subpopulation of complexes. Furthermore, the study provided additional evidence that the ribosomal assembly progress through multiple parallel pathways. Results of similar experiments with the bacterial large subunit were also recently reported²²⁰.

Analysis of *in vivo* assembly intermediates is still more challenging and thus far the main approach to accumulate the intermediates was a single/double deletion of an assembly factor or ribosomal protein. Structure of the small subunit assembly intermediates accumulating in cells lacking KsgA^{97,98}, RsgA^{221,222}, RimM^{208,209} and both RsgA and RbfA²²³ as well as the large subunit assembly intermediates accumulating in the cells lacking EngA and EngB¹⁸⁵ or RbgA^{171,174} have been determined. Some of the assembly factors were also shown to bind the mature subunits. Complexes of YjeQ²²², RbfA⁹⁰, RsgA²⁰² and Era²²⁴ with the mature small subunit, as well as EngA¹⁸⁹ with the mature large subunit have been solved. All of these factors bind to the active sites of the subunits – decoding center in the 30S or the peptidyl transferase center in 50S, and are involved in the late steps of the ribosome assembly.

Instead of assembly factors, Davis and colleagues deleted a ribosomal protein bL17²¹⁶. Assembly intermediates that accumulated under such conditions were visualized using cryo-EM and obtained maps showed multiple intermediates of the

large subunit assembly. That study not only showed that the *in vivo* maturation of the bacterial ribosome large subunit progress through multiple parallel pathways, but also proposed that the assembly happens hierarchically by incorporation of protein clusters.

In general, accumulation of assembly intermediates in cells lacking either an assembly factor or a ribosomal protein is not an ideal approach. Such conditions, albeit necessary due to a rapid nature of the ribosome maturation, are far from native and may have unforeseen effects on the ribosome maturation. Even though such studies usually account for a possibility of dead-end intermediates and validate the ability of analyzed assembly intermediates to mature into a complete, active subunit, interpretation of such obtained 3D reconstructions needs to be done with care. In line with a recent study that showed that despite the fact that a substantial portion of the assembly intermediates of the small subunit accumulating in $\Delta rimM$ and $\Delta yjeQ$ strains can mature into a 30S, the intermediates have a weak affinity for the deleted assembly factors YjeQ and RimM²¹⁰. These results imply that the accumulating assembly intermediates are not a true substrate of these factors and may represent a thermodynamically stable assembly intermediate which arose due to the absence of these assembly factors. Interestingly, such a case was not observed thus far for the large subunit, suggesting an intriguing difference in the thermodynamic stability of the small and large subunit assembly intermediates¹⁹⁷.

As an alternative to the non-native conditions of ribosome assembly in strains lacking an assembly factor or a ribosomal protein an idea of using a small molecule to slow down or completely stall the assembly of bacterial ribosome was considered. However, thus far only one such compound was discovered and successfully used²²⁵. And so, despite the astonishing progress that we witnessed in the past few years in the field of bacterial ribosome assembly, there is still much to be learned. We still only understand a fraction of the ribosome maturation process. With the continuous advances in molecular biology methods, macromolecule preparation and purification methodology as well as reduced requirements for the cryo-EM in terms of sample amounts and purity, it will soon be possible to fully decipher the cellular assembly mechanism of the bacterial ribosome.

Mitoribosome assembly is subject of intense investigation

Despite the fact that the mitoribosome evolved from the bacterial ribosome, its architecture is strikingly different²²⁶. Furthermore, because of the evolutionary shift of the mitochondrial genes into the nuclear genome, the mitoribosome assembly is expected to differ from that observed for the bacterial ribosome. Nevertheless, just like in bacteria, the rRNAs of the mitoribosome are generally transcribed as one polycistronic precursor RNA that needs to be processed^{227,228}. The extent of necessary RNA processing, however, depends on the eukaryotic species. The assembly of the mitoribosome starts co-transcriptionally and the processing and modification of the rRNA is associated with the hierarchical association of the ribosomal proteins²²⁹. Contrary to other ribosomes, the mitoribosomal rRNA is scarcely modified. There are only 10 known modifications in the human mitoribosome, compared to more than 30 in the bacterial ribosome and more than 200 in the cytoplasmic eukaryotic ribosome²²⁶. Moreover, depending on the species, most or all of the ribosomal proteins are encoded by the nuclear genome. Therefore, mitoribosome assembly requires coordination of the transcription machinery in the mitochondria and the transcription

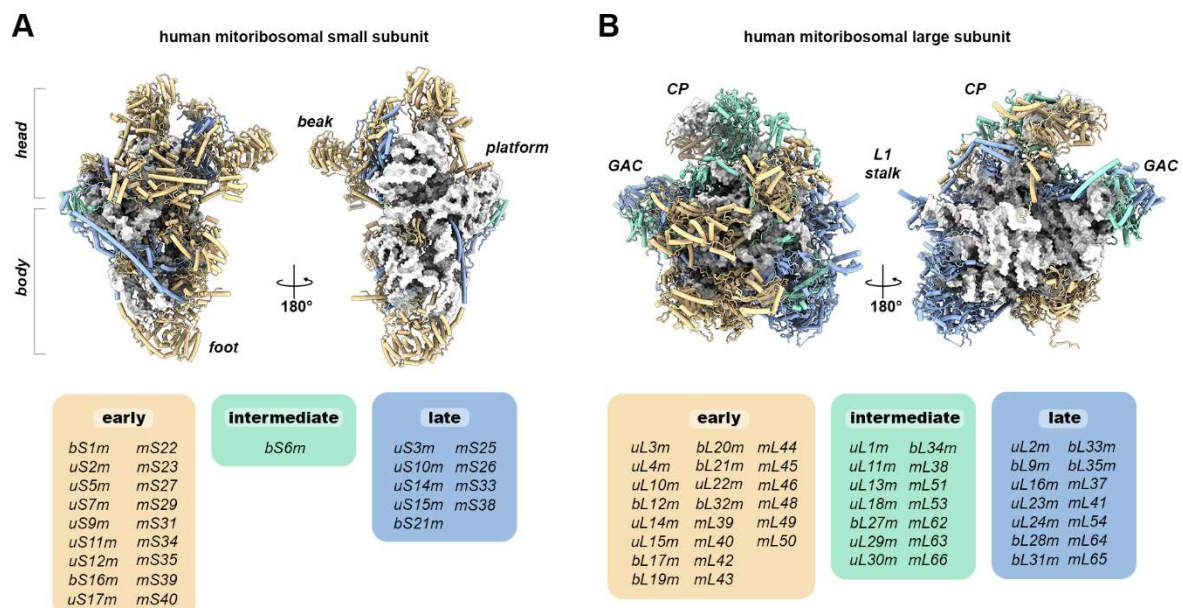


Figure 6. Order of mitoribosomal proteins association in humans.

Structure of the human mitoribosomal small (A) and large (B) subunit is presented from the solvent-exposed (left) and intersubunit (right) side (PDB: 6ZM6). Ribosomal RNA is shown in surface representation and colored silver, while the ribosomal proteins are depicted in cartoon representation and colored according to their assembly kinetics (Bogenhagen et al., 2018). The early binding ribosomal proteins are colored orange, the intermediate ones are shown in green and the late binding proteins are depicted in blue. The proteins are additionally grouped and listed below the structures.

and translation machinery in the nucleus and cytoplasm. Recent biochemical studies of the human and yeast mitoribosome maturation deciphered the order in which the mitoribosomal proteins are imported into the mitochondria²³⁰ or incorporated into the mitoribosome²³¹ (**Figure 6**). Based on these results the mitoribosomal proteins were sorted into the early, intermediate and late binders. It was also proposed that, as with the cytoplasmic prokaryotic and eukaryotic ribosomes, the mitoribosomal subunit can mature via limited parallel pathways²³¹.

Putative mitoribosomal assembly factors were also studied extensively through biochemical and genetic approaches over the years (**Table 2**). Many of these identified

Table 2. Major human mitoribosomal assembly factors. Adapted from Kummer and Ban, 2021²²⁶

group	assembly factor		subunit	reference
	H. sapiens	bacterial homolog		
RNA modifying enzymes	METTL15	RsmH	SSU	232,233
	MRM1	RlmB	LSU	234,235
	MRM2	RrmJ	LSU	235–237
	MRM3		LSU	235,237,238
	TRMT61B		LSU	239
	TFB1M	KsgA	SSU	240–242
	NSUN4	YebU	SSU/LSU	243,244
	RPUSD4		LSU	245,246
	PUSL1	TruA family	LSU	245,247
DEAD-box helicases	DDX28		LSU	227,248,249
	DDX30		SSU/LSU	227
ribosome dependent GTPases	MTG1 (GTPBP7)	RbgA	LSU	250,251
	MTG2 (GTPBP5)	ObgE	LSU	250,252–256
	GTPBP6	HflX	LSU	257
	GTPBP8		LSU	258
	OBGH2 (GTPBP10)	ObgE	(SSU)/LSU	258,259
	MTG3 (NOA1)	YqeH	SSU	260–262
	ERAL1		SSU	263–265
general maturation factors	MALSU1	RsfS	LSU	266–268
	LOR8F8 (MIEF1)		LSU	247,268
	mt-ACP		LSU	268
	RBFA	RbfA	SSU	265
	MTERF4		LSU	243,244
	MTERF3		LSU	269
	PTCD1		LSU	270
	YBEY	YbeY	SSU/(LSU)	271
	p32		SSU/LSU	272,273
	MPV17L2		SSU/LSU	274
	FASTKD2		LSU	227
CLXP		SSU	275	

factors show homology to known bacterial assembly factors. However, sequence and/or structure homology does not necessarily mean that a given assembly factors fulfills the same function in mitoribosome assembly as its homolog does in the bacterial ribosome maturation⁶⁶. With such a drastic change to the mitoribosomal architecture it is highly plausible that some of the assembly factors adjusted their role in the maturation process. Moreover, just like with the ribosomal proteins specific to mitochondria, there are several mitochondrial assembly factors which do not show any similarity to known bacterial proteins. Therefore, to better understand mitoribosomal maturation it is critical to obtain a mechanistic description of the process that requires visualization of the assembly intermediates. Understanding of the mitoribosome maturation process is also medically relevant, since defects in mitoribosomes cause problems in the production of proteins responsible for oxidative phosphorylation and lead to mitochondrial disorders²⁴.

Structural information on the mitoribosome assembly is, however, still scarce. So far, only two late assembly intermediates of the human mitoribosomal large subunit were visualized²⁶⁸. The late assembly intermediates showed immature peptidyl transferase center (PTC) and additional density for 3 assembly factors – ACP, MALSU1 and LOR8F8. These structures showed that, just like in the case of cytoplasmic ribosomes, the active center of the large subunit (i.e. PTC) is the last structural element to mature. Additionally, the discovered cluster of 3 assembly factors, termed ACP module, is believed to prevent premature association of the subunits.

Compared to bacteria where ribosomes assemble in 1-2 minutes⁵¹, analysis of the human mitoribosome assembly intermediates should be more feasible since the process can take even up to 3 hours²³⁰. Still, the amounts of natively purified mitoribosomes and the additional steps required for purification of assembly intermediates make the task of structural analysis challenging in other respects. Nevertheless, with current state of the single particle cryo-EM and the lower requirements for sample purity and quantity, high-resolution structures of the mitoribosome assembly intermediates seem to be within reach.

Aim of the thesis

Defects in the assembly of the mitoribosomal subunits leads to a reduced amount of translationally capable ribosomes and, as a result, decreased capacity of the oxidative phosphorylation (OXPHOS) machinery. Since aerobic organisms depend on the OXPHOS pathway for energy conversion, its reduced activity causes disorders which often manifest with a broad spectrum of clinical symptoms. Such disorders in humans, associated with mitoribosome defects, often occur from a young age and present themselves as severe multisystemic diseases, like hypertronic cardiomyopathy, sensorineural hearing loss, encephalomyopathy or Leigh syndrome^{66,276–279}. In addition, recent studies showed that deregulation of mitoribosome components and assembly factors may lead to cancer development and its progression^{272,280}. Due to their shared ancestry with the bacterial ribosome, mitoribosomes are also sensitive to certain antibiotics used for treatment of microbial infectious diseases which cause severe side effects in humans²⁸¹.

Understanding the mitoribosome maturation is therefore not only fundamentally interesting, but also of crucial importance from a biomedical perspective. Deeper understanding of the mitoribosome assembly should improve our understanding of the severe multisystemic diseases associated with mitoribosome defects as well as aspects of cancer development and its progression. Consequently, a number of research groups are already investigated mitoribosome assembly using genetic and/or biochemical methods in order to reveal the process of mitoribosome maturation²⁸².

In order to investigate biogenesis of mitoribosomes I used cryo-electron microscopy to determine the structures of different assembly intermediates of the mitoribosomal large subunit. At the beginning of my PhD, another project in our research group was focusing on obtaining a structure of a mature mitoribosome from a human parasite *Trypanosoma brucei*. Therefore, because of the experience in our group on working with this organism and its mitoribosome, I initially set out to determine the high-resolution structures of mitoribosomal large subunit assembly intermediates purified from *T. brucei*. Subsequently, in collaboration with Dr. Tea Lenarčič in our group, I also studied this process in humans by determining the structures of human mitoribosomal large subunit assembly intermediates.

Chapter 1. Structural insights into the mechanism of mitoribosomal large subunit biogenesis

The content of this chapter was previously published in Molecular Cell.

Jaskolowski, M.*, Ramrath, D. J. F.*, Bieri, P.*, Niemann, M.*, Mattei, S., Calderaro, S., Leibundgut, M., Horn, E. K., Boehringer, D., Schneider, A., & Ban, N. (2020). Structural Insights into the Mechanism of Mitoribosomal Large Subunit Biogenesis. *Molecular Cell*. <https://doi.org/10.1016/j.molcel.2020.06.030>

Published online 16 July 2020.

Statement of contribution

Dr. Moritz Niemann, Dr. David Ramrath, Salvatore Calderaro and Elke K. Horn isolated the mitochondria. Dr. David Ramrath and Dr. Simone Mattei purified the mitoribosomes and prepared cryo-EM grids. Together with Dr. Daniel Boehringer, they collected the cryo-EM data. Dr. David Ramrath, Dr. Simone Mattei and I analyzed the cryo-EM data and calculated the cryo-EM density maps. Dr. David Ramrath, Dr. Marc Leibundgut and Dr. Philipp Bieri built the initial atomic models. I and Dr. Marc Leibundgut built, revised, corrected, refined and validated the final molecular models. I deposited all the data to the Protein Data Bank and Electron Microscopy Data Bank. I, Dr. Philipp Bieri, Dr. David Ramrath, Dr. Marc Leibundgut and Prof. Nenad Ban interpreted the structures. Dr. Moritz Niemann and Salvatore Calderaro performed the RNAi experiments. I, Dr. Philipp Bieri, Dr. Moritz Niemann and Salvatore Calderaro created the figures. I drafted the manuscript for publication and I, Dr. Philipp Bieri and Prof. Nenad Ban edited it and finalized it. All authors contributed to the final version of the manuscript.

Structural Insights into the Mechanism of Mitoribosomal Large Subunit Biogenesis

Mateusz Jaskolowski^{1,3}, David J.F. Ramrath^{1,3}, Philipp Bieri^{1,3}, Moritz Niemann^{2,3}, Simone Mattei¹, Salvatore Calderaro², Marc Leibundgut¹, Elke K. Horn², Daniel Boehringer¹, Andre´Schneider^{2,*} and Nenad Ban^{1,4,*}

¹Department of Biology, ETH Zurich, Zurich 8093, Switzerland

²Department of Chemistry and Biochemistry, University of Bern, Bern 3012, Switzerland

³These authors contributed equally

⁴Lead Contact

*Correspondence: andre.schneider@dcb.unibe.ch (A.S.), ban@mol.biol.ethz.ch (N.B.)

Summary

In contrast to the bacterial translation machinery, mitoribosomes and mitochondrial translation factors are highly divergent in terms of composition and architecture. There is increasing evidence that the biogenesis of mitoribosomes is an intricate pathway, involving many assembly factors. To better understand this process, we investigated native assembly intermediates of the mitoribosomal large subunit from the human parasite *Trypanosoma brucei* using cryo-electron microscopy. We identified 28 assembly factors, six of which are homologous to bacterial and eukaryotic ribosome assembly factors. They interact with the partially folded rRNA by specifically recognizing functionally important regions such as the peptidyl transferase center. The architectural and compositional comparison of the assembly intermediates indicates a stepwise modular assembly process, during which the rRNA folds towards its mature state. During the process, several conserved GTPases and a helicase form highly intertwined interaction networks that stabilize distinct assembly intermediates. The presented structures provide general insights into mitoribosomal maturation.

Introduction

Mitochondria are cellular organelles responsible for energy conversion and ATP production. They originated from a free-living α -proteobacterium and therefore share a common ancestor with present-day bacteria (Roger et al., 2017). Although during evolution the majority of the genetic information has been either lost or transferred from the mitochondrial to the nuclear genome, mitochondria have retained their own transcription and translation machineries, including mitochondrial ribosomes (mitoribosomes). In all known organisms mitoribosomes are responsible for the synthesis of essential membrane proteins of the oxidative phosphorylation complexes (Ott et al., 2015).

Despite sharing a common ancestor, mitoribosomes differ considerably in composition and architecture from their bacterial counterparts as well as between different eukaryotic lineages, as recently visualized at high-resolution by cryo-electron microscopy (cryo-EM). In general, mitoribosomes feature an increased number of ribosomal proteins in comparison to the bacterial 70S ribosome, whereas the ribosomal RNAs (rRNA) are highly variable in length. The rRNAs of the yeast 74S mitoribosome developed additional expansion segments to which mitoribosome-specific proteins bind, leading to an RNA:protein ratio of 1:1 (2:1 in bacteria) (Desai et al., 2017). In contrast, the mammalian 55S mitoribosome possesses a highly reduced rRNA, but acquired additional mitochondria-specific ribosomal proteins, resulting in an RNA:protein ratio of 1:2 (Amunts et al., 2015; Greber et al., 2015). The *Trypanosoma brucei* mitoribosome is the utmost example of this evolutionary shift towards protein-based architecture as it is composed of 127 mitoribosomal proteins and contains very small rRNAs resulting in an RNA:protein ratio of 1:6 (Ramrath et al., 2018).

Considering the unique architecture of mitoribosomes and the fact that rRNA transcription occurs inside the mitochondrion, whereas most mitoribosomal proteins are synthesized in the cytoplasm and have to be imported, the biogenesis of mitoribosomes is expected to differ from the assembly of prokaryotic and eukaryotic cytoplasmic ribosomes. However, in contrast to the cytoplasmic ribosomes, whose biogenesis has been studied extensively for decades using genetic, biochemical and structural approaches (Chen and Williamson, 2013; Cruz et al., 2015; Davis et al., 2016; Klinge and Woolford, 2018; Shajani et al., 2011; Woolford and Baserga, 2013), maturation of mitoribosomes is less well-understood. Only a few mitoribosomal

assembly factors have been identified so far, including rRNA methyltransferases (Mrm1, Mrm2 and Mrm3), ATP-dependent RNA helicases (Mss116 and Mrh4) and GTPases (Mtg1, Mtg2 and Mtg3) (reviewed in Silva et al., 2015). For the mammalian 28S and 39S subunits, an assembly hierarchy of their mitoribosomal proteins has recently been proposed using SILAC pulse-labeling experiments (Bogehagen et al., 2018). At the same time an assembly pathway of mitoribosomal proteins was suggested for the yeast 54S large subunit (LSU) using a systematic genomic deletion of 44 yeast mitoribosomal proteins (Zeng et al., 2018). Both studies showed that, similarly to the bacterial LSU (Davis et al., 2016), the mitoribosome is assembled through stepwise association of clusters of ribosomal proteins.

Structural insights into mitoribosomal assembly is limited to studies in which assembly intermediates of the *Trypanosoma brucei* mitoribosomal SSU were described (Saurer et al., 2019), and the observation of two late-stage assembly intermediates of the human 39S LSU (Brown et al., 2017). The latter showed that maturation of the peptidyl transferase center (PTC) formed by the 16S rRNA and the binding of bL36m are among the last steps of human mitoribosomal LSU maturation. Cryo-EM reconstructions described in that study also revealed a module consisting of three assembly factors (MALSU1, L0R8F8 and mt-ACP) that binds to uL14m and prevents premature subunit association.

Mitochondrial biogenesis is biomedically important since mutations in mitoribosomal proteins, rRNAs, and assembly factors have been linked to a heterogeneous group of human multisystemic OXPHOS diseases as well as cancer development and progression (Kim et al., 2017; Silva et al., 2015). Furthermore, a mammalian ortholog of the recently identified yeast mitoribosomal assembly factor Mam33, is a protein involved in cancer progression and mitochondrial diseases (Hillman and Henry, 2019).

Here we present the atomic structures of two native *T. brucei* mitoribosomal large subunit assembly intermediates determined by cryo-EM at resolutions of 3.1 Å and 3.9 Å. The intermediates feature 12S rRNAs in immature conformations and vary in the number of bound mitoribosomal proteins and biogenesis factors, suggesting a sequential order of assembly. We discover many novel assembly factors in addition to those with homology to previously biochemically characterized biogenesis factors of other systems. Moreover, we visualize the mode of interaction of the assembly factors with the immature mitoribosome. Finally, we present the conformational changes that

occur during maturation of mitoribosomes and the roles of various factors in this process.

Results

Cryo-EM analysis of trypanosomal mitoribosomes reveals two native assembly intermediates of the large subunit

Mitoribosomal particles were purified from wild-type *T. brucei* cells and analyzed using cryo-EM. Two complexes that are structurally related to the ribosomal LSU, referred to as states A and B, could be classified from the dataset (Figure 1 and S1). The cryo-EM maps were resolved to 3.9 Å and 3.1 Å (Figure S2), respectively, and were of sufficient quality for building and refining an atomic model for both states according to the previously described strategy (Ramrath et al., 2018) (Table 1).

Several lines of evidence indicate that the visualized complexes represent large mitoribosomal subunit assembly intermediates. Both complexes lack the central protuberance (CP) (Figure 1A), a prominent architectural feature that is responsible for intersubunit contacts with the small subunit (SSU), which is known to be formed late during bacterial large ribosomal subunit biogenesis (Davis et al., 2016). Furthermore, a highly intertwined cluster of non-ribosomal proteins is located on the subunit interface side of both complexes (Figure 1A-B). The protein cluster interacts with mitoribosomal proteins and the central core of the LSU formed by the 12S rRNA that harbors the PTC found in immature conformation. Whereas the intersubunit side is almost completely covered, the solvent accessible side resembles the previously published subunit (Ramrath et al., 2018). The L1 stalk, involved in tRNA release at the exit site, lacks mitoribosomal proteins mL91 and mL97 in both states. In the mature LSU, these proteins are located at the base of the L1 stalk, ensuring its correct positioning and solid attachment to the LSU. Although in the L1 stalk only two ribosomal proteins are missing, the L7/L12 stalk is completely absent in both states, along with many of the stalk base mitoribosomal proteins, in particular uL10m, uL16m, bL36m and mL88. Furthermore, both states lack mL79 that links the CP with the stalk base in the mature LSU. Additional nearby proteins, mL64 and mL84, although present in both complexes, adopt different, immature conformations. In total, states A and B lack 22 and 17 mitoribosomal proteins, respectively, out of the 72 found in the mature LSU.

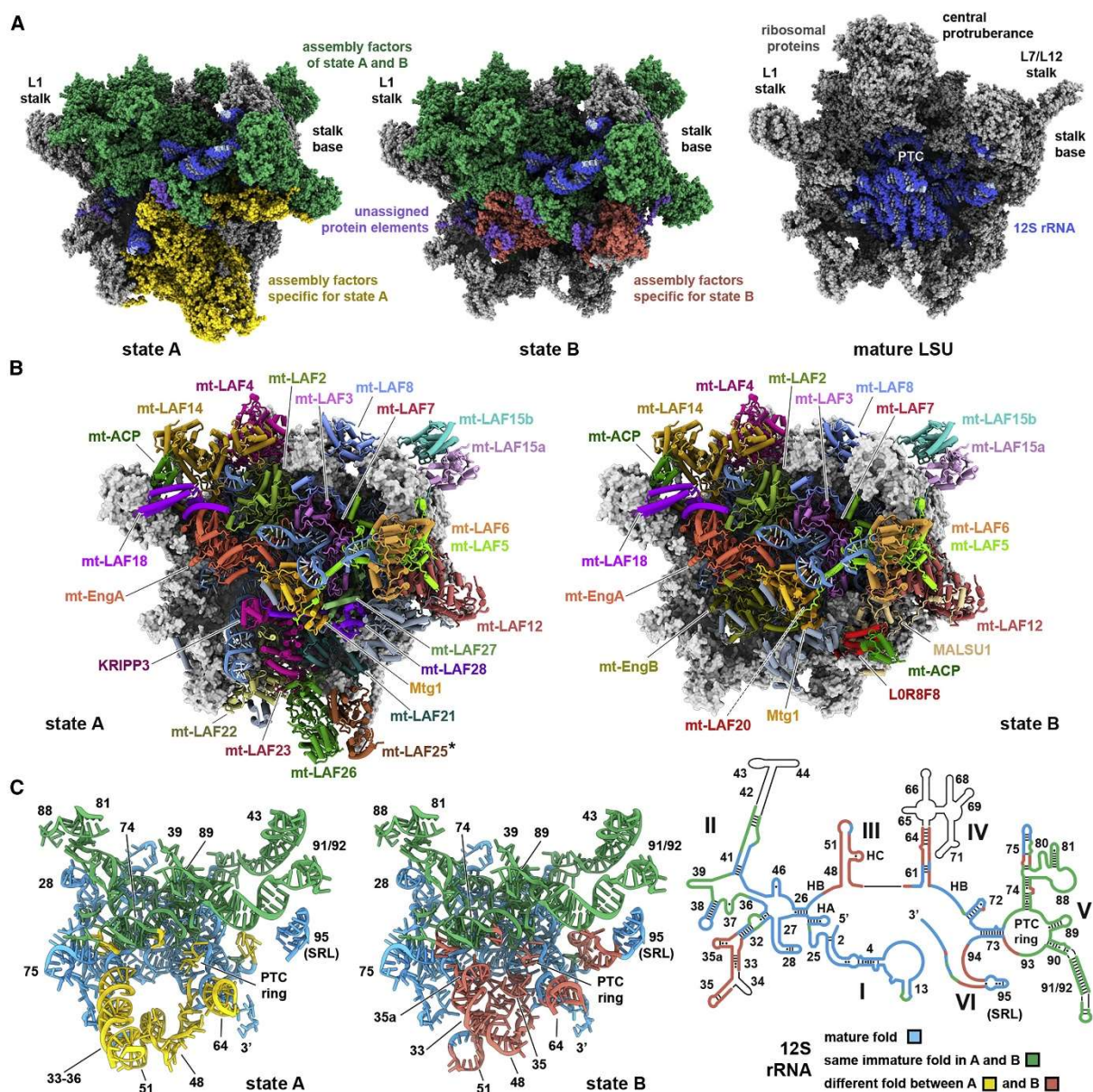


Figure 1. Architectural overview of the mitoribosomal LSU assembly intermediates of *T. brucei*

(A) The molecular structures of the mitoribosomal LSU state A and state B assembly complexes are shown in sphere representation from the intersubunit side. For comparison, the LSU of *T. brucei* (PDB: 6HIX) (Ramrath et al., 2018), including a modeled 12S rRNA, is shown. **(B)** The assembly factors of states A and B are illustrated and colored individually. The model of the 12S rRNA is blue. The ribosomal proteins are shown as gray surfaces. mt-LAF20 in state B is labeled with a dashed line, as it is occluded from view by other assembly factors. mt-LAF25* lacks an assigned sequence, but based on fold homology represents a putative methyltransferase. **(C)** The 12S rRNA structures of states A and B are shown from the intersubunit side (same orientation as in A and B). The 12S rRNA segments, some of which are labeled, are colored according to their conformational state: mature elements in blue, immature elements with the same fold in states A and B in green, and elements adopting conformations specific for state A in yellow and for state B in red, respectively. The 12S rRNA secondary structure diagram of state B is given in the same color key.

Table 1. Cryo-EM data collection, map refinement, model refinement and validation statistics of the *T. brucei* mt-LSU assembly intermediates.

Structure:	State A mt-LSU assembly intermediate	State B mt-LSU assembly intermediate
EMDB accession / PDB code	10999 / 6YXX	11000 / 6YXY
Data collection:		
Microscope	FEI Titan Krios	
Detector	Falcon 3	
Voltage (keV)	300	
Electron exposure (e-/Å ²)	75	
Pixel size (Å)	1.085	
Magnification	129,000x	
Defocus range (µm)	1-3	
Automation software	EPU	
Selected micrographs	26,776	
EM Reconstruction:		
Initial particle images (no.)	2,480,610	
Final particles (no.)	16,215	98,508
Accuracy of rotations (degrees)	0.722	0.411
Accuracy of translations (Å)	0.915	0.487
Resolution (unmasked / masked) at FSC=0.143 (Å)	3.9	3.1
Sharpening B-factor (Å ²)	-153.93	-128.35
Coordinate real space refinement (PHENIX version 1.17.1-3660)		
Unit cell	P1	P1
a, b, c (Å)	260.40, 324.05, 292.23	258.23, 321.16, 294.04
α = β = γ (°)	90	90
CC _{mask}	0.76	0.81
High resolution limit for refinement	3.9	3.1
Resolution according to model vs. map FSC=0.143 / FSC=0.5 (masked) criterions (Å)	3.8 / 3.9	3.0 / 3.1
Resolution according to model vs. map FSC=0.143 / FSC=0.5 (unmasked) criterions (Å)	3.9 / 4.0	3.0 / 3.2
Model composition:		
Number of chains	96	94
Total atoms	183,960	177,572
Protein residues	29,866	19,399
RNA residues	906	903
Ligands: GTP/ATP/NAD/SPD/PM8/H ₂ O/Na ⁺ /Mg ²⁺ /Zn ²⁺	2 / 1 / 1 / 1 / - / 1 / 8 / 2 / 17 / 7	3 / 1 / 1 / 1 / 1 / 2 / 10 / 2 / 33 / 5
Average B-factors (min/max/mean):		
Protein	5.49 / 115.83 / 33.55	3.34 / 90.08 / 27.12
RNA	4.28 / 261.05 / 63.34	4.95 / 175.21 / 45.28
Ligand	1.89 / 98.95 / 57.77	5.40 / 96.97 / 51.22
Water	13.94 / 57.01 / 33.98	9.39 / 38.53 / 19.00
Model validation:		
RMSD bonds (Å)	0.002	0.002
RMSD angles (°)	0.468	0.460
All-atom clashscore	9.26	7.78
EMRinger score	1.14	2.35
MolProbity score	1.64	1.66
Ramachandran statistics:		
Favored (%)	97.17	99.17

Allowed (%)	2.82	2.82
Outliers (%)	0.01	0.01
Rotamer outliers (%)	0.95	1.29
<u>RNA validation:</u>		
Sugar pucker outliers (%):	0.33	1.22
Angle/bond outliers (%):	0	0
Bond outliers (%):	0	0
CC _{mask} , real space correlation coefficients; EMDB, Electron Microscopy Data Bank; PDB, Protein Data Bank; RMSD, root-mean-square deviation; SPD, spermidine, FSC., Fourier shell correlation		

Overall, of the 25 additional proteins identified in state A and the 21 in state B, 16 are present in both states (Figure 1B and SI3). Some of these proteins are structural homologues of previously described mitoribosomal or cytoplasmic ribosomal assembly factors, including bacterial GTPases EngA (Bharat et al., 2006) and EngB (Schaefer et al., 2006), rRNA methyltransferase RlmI (Purta et al., 2008), mitochondrial GTPase Mtg1 (Barrientos et al., 2003), mitochondrial rRNA methyltransferase MRM3 (Rorbach et al., 2014) and mitochondrial RNA pseudouridine synthase Pus5/RPUSD4 (Ansmant et al., 2000; Antonicka et al., 2017), as well as the ACP-LYRm module recently identified in human mitochondrial LSU assembly intermediates (Brown et al., 2017). Consequently, we assigned the newly identified proteins as assembly factors and refer to them as mitochondrial LSU assembly factors (mt-LAFs). Assembly factors with previously characterized homologs were named with their original name and an “mt-” prefix. To corroborate their functional role in ribosome maturation, a selection of the newly found assembly factors was further tested using RNAi knockdown experiments, which showed that their ablation interferes with LSU maturation (Figure 2).

Comparison of the assembly intermediates suggests the order of maturation

In both assembly intermediates, the intertwined assembly factors stabilize the 12S rRNA in an immature conformation (Figure 1). Domain II, namely helices 36-37, 39 and 42-44, and domain V that forms the PTC in the mature LSU, are present in the same immature conformation in both states. However, helices 33-35 of domain II, the entire domain III and helices 61 and 64 of domain IV differ between the two assembly intermediates (Figure 1C). In state A, those rRNA regions are supported by a cluster of nine assembly factors including mt-LAF21 and KRIPP3, which bind between domains II, III and IV. Consistent with the important structural role of these factors in

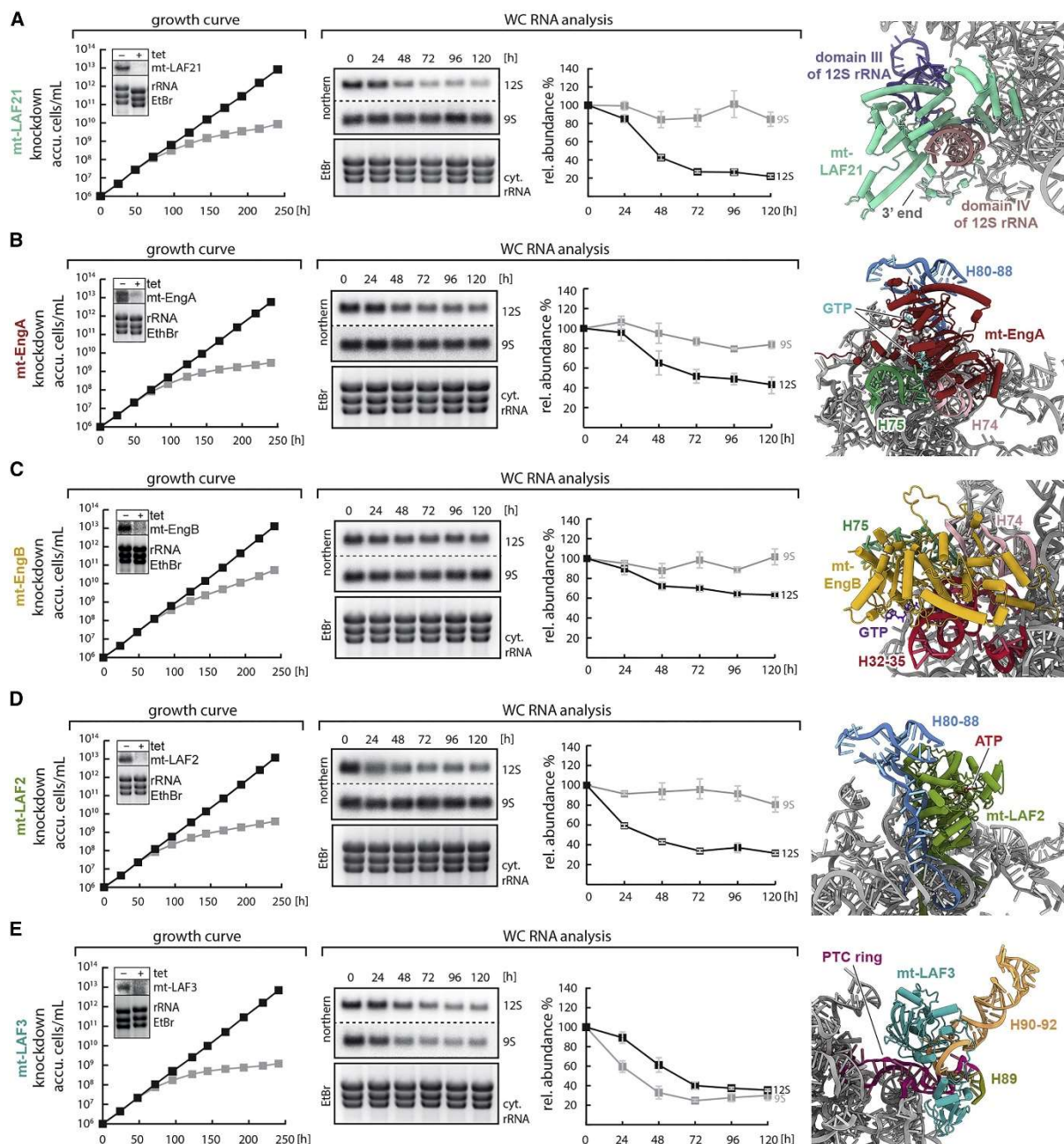


Figure 2. Importance of assembly factors for cell growth and rRNA stability

The protein levels of five assembly factors (A–E) of the LSU assembly intermediate were reduced by tetracycline-inducible RNAi in *T. brucei* cells. All knockdown cultures show reduced growth 72 h after induction. The levels of 12S and 9S rRNA in the knockdown strains were followed in 24-h intervals by northern blotting, and with the exception of mt-LAF3 (E), all show a specific reduction of the 12S rRNA steady-state level, but not of the 9S rRNA. Ribosomal proteins of the LSU and SSU (see Figure S3) are used as controls. The results complement previous findings regarding the mitoribosomal SSU assembly machinery (Saurer et al., 2019). The structures of the assembly factors from state B are shown together with their corresponding rRNA interaction sites. The structure of mt-LAF21 (A) was taken from state A, as it is specific to that state. Cultures were grown in triplicates. Error bars indicate the average deviation from the mean. See also Figure S3.

stabilizing rRNA domains in immature conformation, knockdowns of mt-LAF21 and KRIPP3 specifically reduce the steady state levels of 12S rRNA. In contrast, the SSU 9S rRNA is not affected, suggesting that the targeted protein is required for LSU, but not SSU maturation. Furthermore, the growth rate of *T. brucei* cells is reduced, presumably due to retarded mitoribosome assembly (Figure 2A and S3C). In state B, the cluster of nine assembly factors specific to state A is replaced by four mitoribosomal proteins (mL90, mL99, mL100 and mL101) and by the assembly factors mt-LAF20 and mt-EngB, a homologue of the bacterial GTPase EngB (Schaefer et al., 2006) (Figure 1A-B). The exchange of proteins is accompanied by a conformational change of the N-terminus of mL85 and 12S rRNA regions, which in state B adopt a fold more similar to the one found in mature LSU. Additionally, we observe differences between the two assembly intermediates in the vicinity of H95 called the sarcin-ricin loop (SRL). While in state A this rRNA region is occupied by protein secondary structure elements that could not be assigned due to lower local resolution, in state B different proteins are bound to the SRL, including mitoribosomal protein uL14m and three assembly factors MALSU1, L0R8F8 and ACP that belong to a module that was recently shown to be involved in maturation of the human mitoribosome (Brown et al., 2017). The exchange of proteins is accompanied by a maturation of the nearby H94. Altogether, since state B has a more complete set of ribosomal proteins and the fold of its rRNA resembles more the one present in the mature LSU, we propose that this state represents a later assembly intermediate than state A.

GTPases form a network of interactions

Studies on ribosomal biogenesis suggest that GTPases are frequently engaged in ribosomal maturation and may couple the ribosome assembly with growth control pathways by sensing the cellular GTP/GDP level (Britton, 2009). The structures of the mitoribosomal LSU assembly intermediates contain several GTPases in agreement with previous biochemical evidence that GTPases also play an important role in mitoribosome biogenesis (Gupta et al., 2018; Kotani et al., 2013). The identified GTPases mt-EngA•GTP2 and Mtg1, as well as mt-EngB•GTP, which is present only in state B, are homologous to GTPases known to be involved in ribosome biogenesis in bacteria (Schaefer et al., 2006; Uicker et al., 2006). All three of these GTPases are

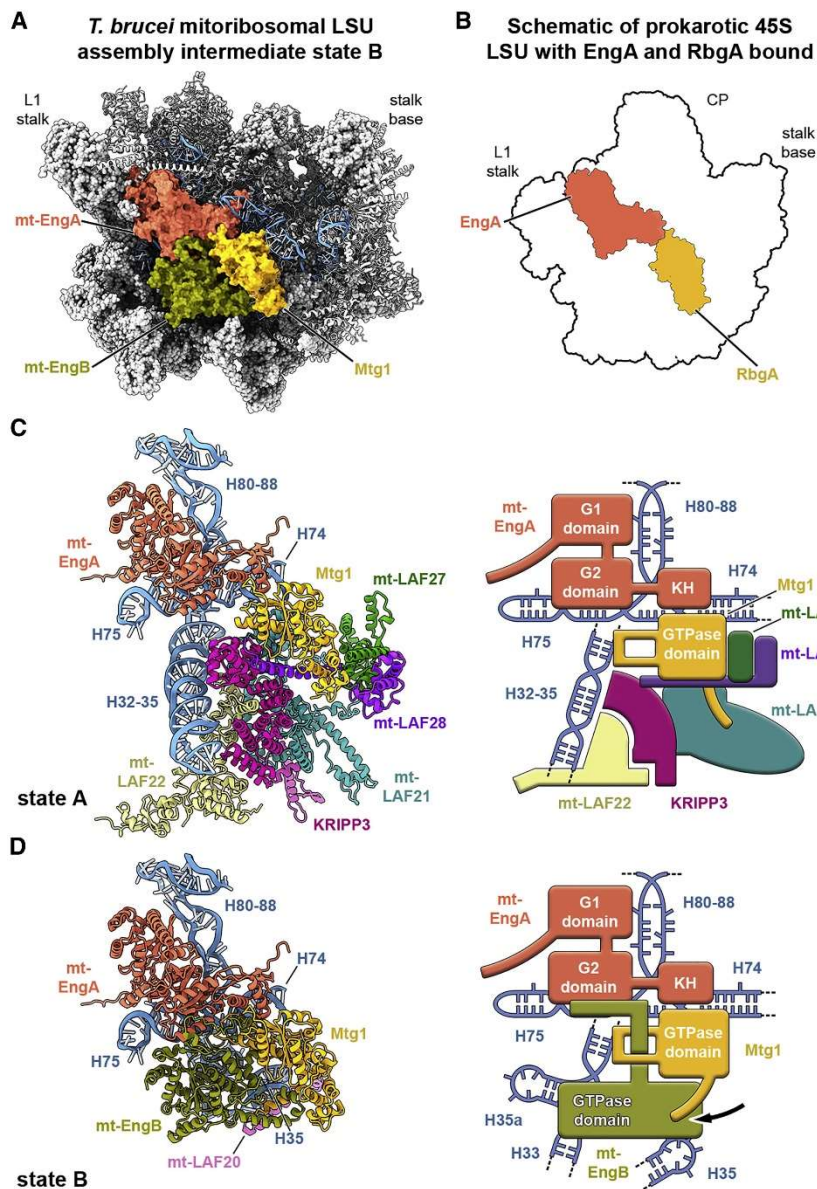


Figure 3. GTPases form an intricate network of interactions

(A) State B assembly intermediate of the *T. brucei* mitoribosomal LSU with the assembly factor GTPases *mt-EngA*, *mt-EngB*, and *Mtg1* shown in colored surface representation and the rRNA in blue. (B) Schematic representation of the binding locations of prokaryotic GTPases *RbgA* and *EngA* to the prokaryotic 45S LSU assembly intermediate based on separate structures of 45S:*RbgA* (PDB: 6PPK) and 50S:*EngA* (PDB: 3J8G). (C and D) The silhouettes of the assembly intermediate states A (C) and B (D) are shown from the intersubunit side as black outlines in the same orientation as in (A). *mt-EngA*, *mt-EngB*, and *Mtg1*, as well as the other assembly factors *mt-LAF20*, *mt-LAF21*, *mt-LAF22*, *KRIPP3*, *mt-LAF27*, and *mt-LAF28*, are involved in the rearrangement of the H32–35 region. Regions of the 12S rRNA that interact with the GTPase cluster (H74, H75, H80–88, and H32–35 regions) are shown in blue, while the remaining 12S rRNA is omitted for clarity. Corresponding schematic representations of the GTPase clusters in states A and B are shown at right. *mt-LAF20* is not shown on the state B schematic, as it is occluded from view by *EngB* and *Mtg1*. The conformational change of the N terminus of *Mtg1* between states A and B is indicated by an arrow. See also Figures S4A and S4B.

located at the center of the LSU and interact with key elements of the 12S rRNA (Figure 3A). In state A, GTPase mt-EngA•GTP2 and Mtg1 interact with each other and form a docking site for the cluster of assembly factors that are only present in state A. During transition to state B, this cluster is replaced by a set of mitoribosomal proteins and assembly factors mt-LAF20 and the GTPase mt-EngB•GTP.

Simultaneous binding of these three GTPases to an assembly intermediate is consistent with the evidence that suggests that homologues of mt-EngA•GTP2, Mtg1 and mt-EngB•GTP work in conjunction during the bacterial LSU maturation (Ni et al., 2016). Although there is currently no structure of these GTPases bound simultaneously to the bacterial large ribosomal subunit, structures of EngA in complex with mature *E. coli* 50S LSU (Zhang et al., 2014) and Mtg1 homolog, RbgA, bound to *B. subtilis* 45S assembly intermediate (Seffouh et al., 2019) are available. We used this information to create a schematic of prokaryotic 45S assembly intermediate in complex with both GTPases (Figure 3B). Strikingly, the observed mode of binding of the trypanosomal mt-EngA•GTP2 and Mtg1 to the mitochondrial LSU assembly intermediate resembles very closely the composite binding mode assumed for its prokaryotic homologs (Figure 3A-B). Therefore, it is tempting to assume that the lessons learned regarding the interplay of these three GTPases based on the structures presented here will also be applicable for understanding the maturation of bacterial ribosomes.

The mt-EngA•GTP2 is a homologue of the bacterial GTPase EngA (also known as Der), which is an essential and conserved bacterial 50S maturation factor (Hwang and Inouye, 2006). As in bacteria, mt-EngA•GTP2 consists of two consecutive GTPase domains (G1 and G2) followed by a C-terminal RNA-binding KH domain. Although the binding environment in the trypanosomal mitoribosome is dominated by proteins instead of rRNA, the overall conformation and binding location of mt-EngA is similar to the bacterial EngA in complex with the immature bacterial 50S (Zhang et al., 2014). The binding of mt-EngA•GTP2 interferes with the association of mL91 and bL33m, as is observed for the latter protein in bacterial ribosomes. The G1 domain binds the helical N-terminus of mL74, stabilizing its immature conformation, and interacts with the immature H88 of the 12S rRNA. The G2 domain attaches to the flipped-out nucleotides of H75, a central helix of the rRNA core, and orients the KH domain to contact the helix 89 of the partially formed PTC. On the opposite end, the N-terminal tail of mt-EngA anchors the factor to the base of the L1 stalk (Figure 3). In

E. coli, only GTP-bound EngA interacts with the LSU intermediate in the late state of maturation (Tomar et al., 2009). This may also be the case for mt-EngA•GTP2 since our cryo-EM maps reveal that GTP molecules are present in the binding pocket of both GTPase domains of mt-EngA•GTP2 (Figure S4A). The importance of mt-EngA•GTP2 in LSU maturation is further emphasized by the fact that *T. brucei* cells grow much slower when mt-EngA•GTP2 is knocked down and we observe a reduction of the 12S rRNA steady state levels 72-hrs post-induction by more than 60% (Figure 2B).

The conserved mitochondrial GTPase 1 (Mtg1) binds at the subunit interface side, where it interacts with the KH domain of mt-EngA, many other LAFs, 12S rRNA, and a few mitoribosomal proteins, including uL14m (Figure 3). The observed binding location and the state of assembly in which the large subunit is lacking proteins uL16m, bL27m and bL36m is consistent with the data available for binding of the prokaryotic homolog of Mtg1, named RbgA (or YlqF), to the immature 50S subunit (Jomaa et al., 2014; Matsuo et al., 2006; Seffouh et al., 2019). Although the active site residues of Mtg1 responsible for the nucleotide binding and hydrolysis are conserved (Gulati et al., 2013), we find the binding pocket in a conformation that prevents binding of a nucleotide due to steric hindrance, implying that Mtg1 in our assembly intermediates serves an architectural role, whereas its nucleotide bound state may be required for LSU assembly at another stage of maturation as proposed earlier (Kim and Barrientos, 2018). Therefore, the observed conformational changes of Mtg1 between the two assembly intermediates (Figure 3) do not involve the GTPase domains but are mostly limited to the N-terminal helix of the factor, which rotates by 90 degrees when the cluster of assembly factors specific for state A dissociates.

Upon dissociation of state A specific factors mt-EngB•GTP is recruited, a homolog of the bacterial GTPase EngB (also known as YihA or YsxC). The contacts between the two GTPases involve the rotated N-terminal helix of Mtg1 and the trypanosomal specific long C-terminal extension of mt-EngB•GTP, which threads through a loop formed by Mtg1, establishing a shared beta-sheet. mt-EngB•GTP knockdown experiments showed reduced cell growth phenotype in trypanosomes and a 40% reduction of the 12S rRNA steady state levels after 96-hrs of RNAi induction (Figure 2C). We observe a nucleotide bound to the GTPase domain of mt-EngB•GTP (Figure S3B) in the same location as observed in the crystal structure of GMP-PNP bound bacterial homologue YsxC (Ruzheinikov et al., 2004).

Due to the structural homology to bacterial factors, the observed contacts between mt-EngA•GTP2 and Mtg1 are likely also formed during bacterial large ribosomal subunit biogenesis. This is not the case for the contacts between GTPases that are mediated by the unique C-terminal extension of mt-EngB•GTP and, therefore, it is possible that in bacteria the communication between EngB and other GTPases is facilitated by the structural changes in the large subunit during maturation. Nevertheless, the observed intricate network of interactions may provide an example of how these GTPases are able to coordinate their action to function as checkpoint proteins in the assembly process (Britton, 2009).

mt-LAF2 is a DEAD-box helicase that interacts with the 12S rRNA

mt-LAF2•ATP, the largest of the identified assembly factors (85.6 kDa, 754 aa), is a member of the DEAD-box helicase family and consists of two highly conserved RecA-like domains, which harbor the DEAD-box motif (Fairman-Williams et al., 2010). The RecA-like domains exhibit a closed conformation, which for bacterial DEAD-box helicase YxiN has been shown to be induced by a cooperative binding of RNA and an ATP molecule (Theissen et al., 2008). Located below the CP region, the RecA-like domains interact with 12S rRNA elements of H37, H39 and H80-81 and with assembly factors. They overlap with the binding location of many mitoribosomal proteins, some of them being part of the CP in the mature LSU, including bL27m, bL31m and bL33m. As observed in other DEAD-box helicases (Putnam and Jankowsky, 2013), mt-LAF2•ATP contains terminal extensions, which in trypanosomal LSU assembly intermediates intertwine with the 12S rRNA core (Figure 4A). The C-terminal tail is particularly long (164 aa) and extends through the entire core of the complex, thereby blocking the entry to the lower part of the polypeptide exit tunnel. mt-LAF2•ATP also contains an additional domain between the two RecA-like domains, which is uncommon for DEAD-box helicases (Figure 4B) (Fairman-Williams et al., 2010). This domain is positioned in front of the nucleotide binding pocket and is stabilized through interactions with mt-LAF3 and mt-LAF8 (Figure S5C). Thus, this interaction may prevent the dissociation of bound nucleotide and subsequent conformational change of mt-LAF2 as long as mt-LAF3 and/or mt-LAF8 stay bound to the assembly intermediate in the current conformation.

Considering that mt-LAF2•ATP is deeply buried in the core of the assembly intermediate and is highly intertwined with the 12S rRNA (Figure S5B) it is likely that

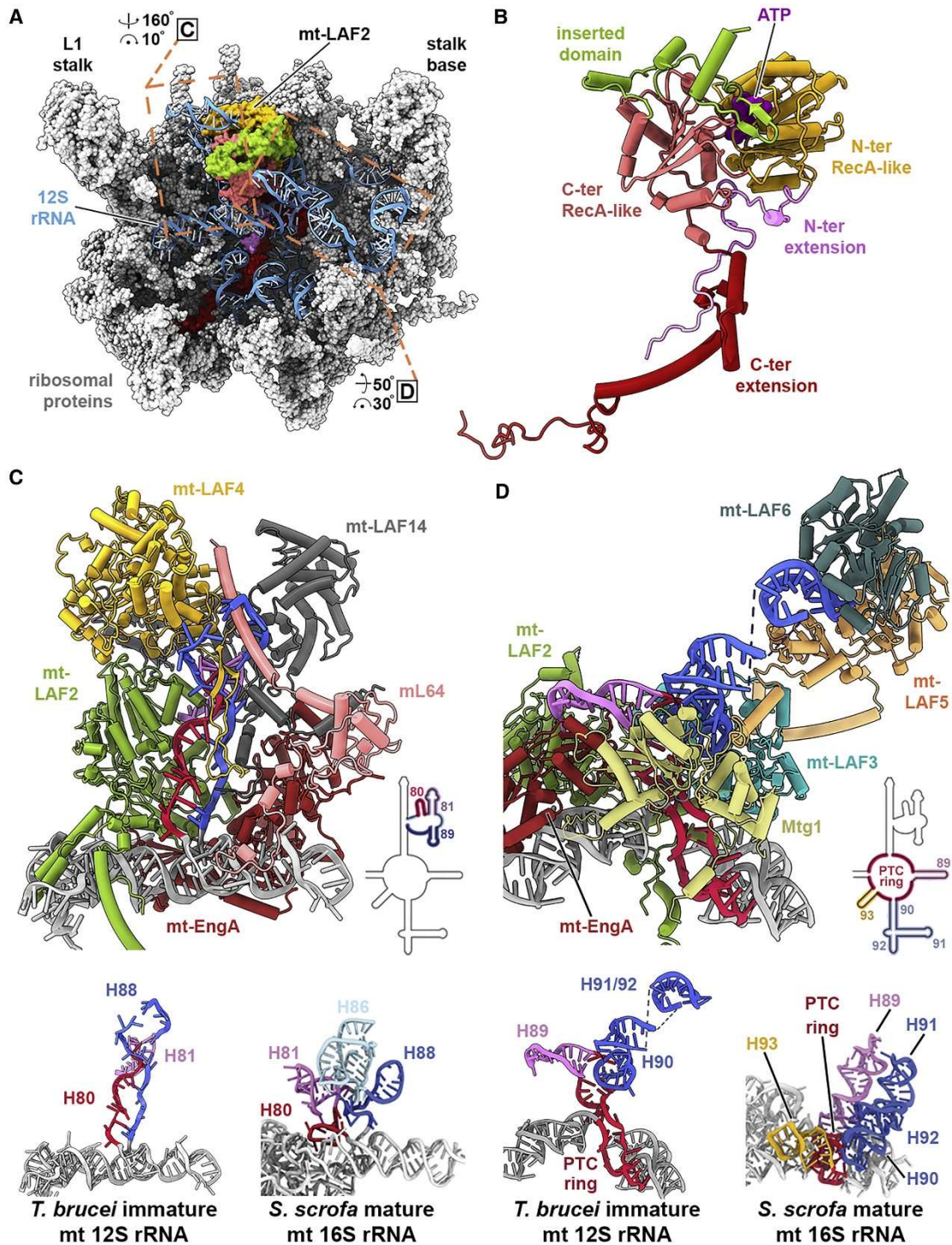


Figure 4. Assembly factors involved in the PTC maturation

(A) State B of the mitoribosomal LSU assembly intermediate is shown from the intersubunit side, with the mitoribosomal proteins in gray and the 12S rRNA in blue. Assembly factor mt-LAF2 is shown in a surface view, with its domains in different colors. Other assembly factors are hidden (see also Figure S5). (B) The assembly factor mt-LAF2 is illustrated, with its domains labeled and color-coded as in (A). (C and D) Immature H80–88 (C) and H89–92 (D) of the 12S rRNA are shown, with surrounding assembly factors colored individually. The immature fold of the rRNA regions is shown below, with a mature conformation of a corresponding fragment from *Sus scrofa* mitoribosomal 16S rRNA for comparison. rRNA fragments are colored as shown on the corresponding secondary structure diagrams of the 12S rRNA domain V.

it is recruited early in the maturation. Indeed, the 12S rRNA steady state levels drop rapidly to 60% after 24-hrs and to 40% after 48-hrs post-induction in mt-LAF2•ATP knockdown cells (Figure 2D) and the growth rate of the *T. brucei* cells is significantly reduced. These results resemble the findings for Mss116, a DEAD-box helicase in yeast, which plays a role in mitoribosomal maturation (De Silva et al., 2017). Deletion of Mss116 lowers the number of assembly intermediates and assembled mitoribosomes, suggesting an involvement at an early stage of the maturation process. Just like mt-LAF2•ATP, Mss116 also has a long C-terminal extension (CTE) (Campo and Lambowitz, 2009), which contributes to the RNA binding (Mohr et al., 2008). Although the CTE of Mss116 adopts a compact conformation it is possible that upon binding to the early stage assembly intermediate, the Mss116 CTE unfolds and interacts with the rRNA similarly to the CTE of mt-LAF2•ATP described here. Taken together, our structural and biochemical results indicate that mt-LAF2•ATP, similarly to Mss116, plays an important role in the early stage of mitoribosome biogenesis and acts as a key rRNA scaffold or even as the nucleation center. Additionally, it interferes with association of the CP proteins and would have to dissociate upon CP maturation, possibly inducing a large rearrangement of the PTC rRNA core region.

Maturation of the peptidyl transferase center involves multiple assembly factors

In the mature ribosomal LSU, rRNA elements of domain V form the PTC, the catalytic site of the ribosome. Although the PTC region of the rRNA is not well ordered in the structure of *T. brucei* mitoribosome (Ramrath et al., 2018) due to high degree of conservation it is reasonable to assume that it will adopt the conformation observed in the mature mammalian 39S LSU (Greber et al., 2015) (Figure 4C-D). Therefore, in the discussion below, we will compare the conformation of the PTC observed in the LSU assembly intermediates to the homology modeled structure of the mature PTC. In both mitoribosomal LSU assembly intermediates, the PTC regions of the 12S rRNA interact with numerous assembly factors and are in an immature conformation. In particular H80, termed P-loop, is unwound by extensive interactions with the DEAD-box helicase mt-LAF2•ATP described above (Figure 4C), similarly as observed in several crystal structures of DEAD-box helicases in complex with RNA fragments (Campo and Lambowitz, 2009; Sengoku et al., 2006) (Figure S5A). Similarly, H88 that in bacteria interacts with the E-site tRNA during translation is unwound in the LSU assembly intermediates. Instead of the canonical stem-loop, the rRNA segment of H88 forms a

ariat-like structure that wraps around a loop of mt-LAF4 and the C-terminal helix of mL64 (also called CRIF1 in mammals). This lariat is sandwiched between a loop of mt-LAF19, the core domain of mt-LAF4 and mt-LAF14 (Figure 4C). Together, these factors prevent formation of the H88 stem-loop. Whereas we cannot detect proteins that are homologous to mt-LAF14 and mt-LAF19 in other organisms, mt-LAF4 shares structural homology with the bacterial tRNA pseudouridine synthase TruD and eukaryotic pseudouridine synthase Pus7. Although its overall catalytic domain fold shows structural homology (Figure S6F), the putative active site lacks the catalytic aspartate and the positively charged rRNA binding cleft found in TruD. Therefore, the pseudouridine synthase fold of mt-LAF4 is presumably used by this assembly factor to specifically recognizing the immature fold of this functionally important rRNA region.

The other 12S rRNA elements of the PTC, in particular the peptidyl transferase ring and the outgoing helices H89 to H92 are kept in an immature conformation by six assembly factors (Figures 4D and 5A). The peptidyl transferase ring and helices H89 and H90 in immature conformation create a three-way junction that is stabilized by mt-LAF3, a structural homolog of the bacterial RluA and mitochondrial RNA pseudouridine synthase RPUSD4 (Antonicka et al., 2017; Hoang et al., 2006; Zaganelli et al., 2017). mt-LAF3 is comprised of two domains acting as a clamp (Figure 5B-C). The N-terminal domain, lacking any close structural homology, interacts specifically with the three-way junction (Figure 5D). The C-terminal domain, structurally similar to the pseudouridine synthase, is sandwiched between the peptidyl transferase ring and H90. The specific interactions of mt-LAF3 with H90 introduce a kink in the canonical stem by flipping out an rRNA base into its active site that prevents the formation of the standard helical structure (Figure 5E). Contrary to the expectations, the flipped-out base is a cytosine (C1010) instead of a uridine, although the observed rRNA fold is related to the crystal structure of the RNA fragment bound to bacterial pseudouridine synthase RluA (Hoang et al., 2006) (Figure S6E). Although the catalytic aspartic acid in mt-LAF3 (D211) and all other residues necessary for its enzymatic activity are conserved, trypanosomes carry a mutation in the vicinity of the binding pocket (L316E). This glutamic acid residue points towards the active site and forms hydrogen bonds with the bound cytosine. This interaction stabilizes the binding of the cytosine and tilts the nucleotide away from the catalytic residues (Figure 5E). Our observations suggest that mt-LAF3 plays an rRNA scaffolding rather than a catalytic role during the visualized mitoribosomal LSU assembly states.

However, surprisingly RNAi-mediated gene knockdown of mt-LAF3, apart from slowing down the growth of *T. brucei* cells, not only reduces the steady state levels of the 12S rRNA by 60% after 72-hrs post-induction, but also affects the stability of the 9S rRNA to a similar extent (Figure 2E). This suggests that mt-LAF3 plays an additional role in SSU maturation or in rRNA post-transcriptional processing.

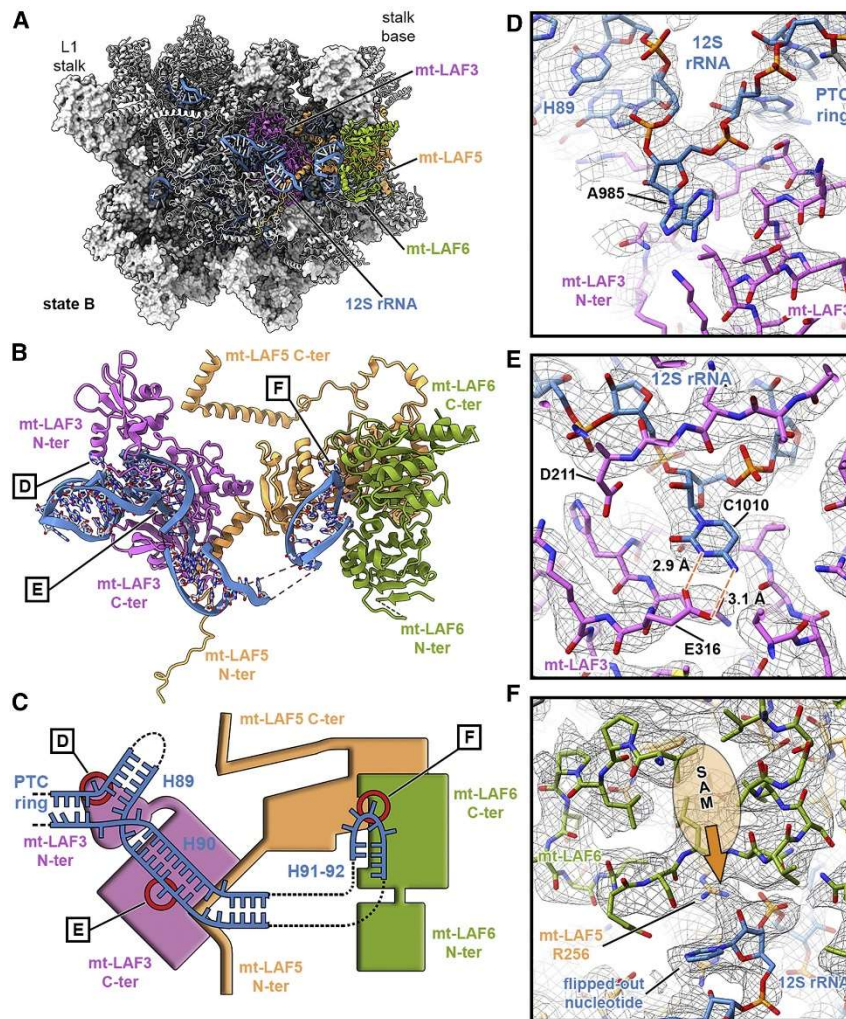


Figure 5. The methyltransferase heterodimer mt-LAF5/mt-LAF6 binds the rRNA helix 92

(A) View of the mitoribosomal LSU assembly intermediate state B from the intersubunit side. The mitoribosomal proteins and assembly factors, colored gray, are represented as surfaces and illustrations, respectively, with the exception of mt-LAF3 (pink), mt-LAF5 (orange), and mt-LAF6 (green). The 12S rRNA is shown in blue. (B and C) Interaction network between assembly factors mt-LAF3, mt-LAF5, and mt-LAF6 and the 12S rRNA elements that in the mature state form the PTC ring. H89–92 in the mature mitoribosomal LSU are shown as ribbons (B) and as a schematic (C). (D–F) The regions of the close-up views shown in (D)–(F) are indicated, with the nucleotides in focus circled in red. (D) The N-terminal domain of the pseudouridine synthase mt-LAF3 stabilizes the kink formed by 12S rRNA elements of the PTC ring and H89, while the C-terminal domain (E) harbors a cytosine nucleotide in its putative active site. (F) The nucleotides of the H91-92 region are sandwiched between the C-terminal domains of mt-LAF5 and mt-LAF6. The putative binding site of the cofactor SAM is indicated. In all 3 close ups, the uncarved cryo-EM density is shown as a black mesh.

The presented results indicate that, although many regions of the LSU are already in a mature conformation, the PTC region of the rRNA is still immature and interacts with numerous assembly factors. The PTC is also one of the last regions of the LSU to mature in prokaryotic and eukaryotic cytoplasmic ribosomes (Bassler and Hurt, 2018; Davis and Williamson, 2017).

A methyltransferase binds to a conserved site of rRNA modification in the A-loop

In a translating ribosome, H92 (A-loop) interacts with the CCA-end of the A-site tRNA and it is crucial for the LSU activity. In both assembly intermediates, helices 90-92 are protruding from the three-way junction and are positioned in a cleft shaped by mt-LAF5 and mt-LAF6 (Figure 5C). Both assembly factors belong to the SpoUT methyltransferases (MTase) superfamily (Anantharaman et al., 2002) and form a heterodimer. mt-LAF6 harbors a conserved set of S-adenosylmethionine (SAM) binding residues, while mt-LAF5 represents an inactive variant due to mutations in cofactor binding residues and resulting rearrangement in the binding pocket. Although enzymatically inactive, mt-LAF5 is likely important for the activity of mt-LAF6 since it contributes in trans a critical active site residue (Figure 5F), similarly as described for the homodimeric methyltransferase NshR that methylates the bacterial 23S rRNA of *Streptomyces actuosus* (Yang et al., 2010). Additionally, mt-LAF5 acts as a docking site, anchoring mt-LAF6 to the LSU assembly intermediate via long N- and C-terminal extensions that interact with multiple other assembly factors and mitoribosomal proteins. mt-LAF6 faces with its catalytic cleft towards the rRNA hairpin loop formed by H92, nucleotides of which are methylated in mitoribosomes of different eukaryotic species (Pintard et al., 2002; Rorbach et al., 2014). Although we could not establish the identity of individual nucleotides in H92 due to lower local resolution of the rRNA in that region, we observed a flipped-out nucleotide that points towards the active site of mt-LAF6 (Figure 5F). In both states, no SAM cofactor is observed in the active site of mt-LAF6, however the position of the flipped-out nucleotide suggests that mt-LAF6 is an active methyltransferase involved in 2'-O-ribose methylation of a nucleotide in H92 loop and therefore may function analogously to MRM2 or MRM3, the 2'-O-MTases that modify Um1369 and Gm1370, respectively, in the A-loop of human mitochondria (Rorbach et al., 2014).

A novel ACP-LYRm module binds and changes the conformation of the L1 stalk

In mitochondria, the acyl carrier protein (ACP) to which a 4'-phosphopantetheine group is covalently attached plays a critical role in the biosynthesis pathway of fatty and lipoic acids by shuttling the growing acyl chain from one enzyme to the other (Cronan et al., 2005). Surprisingly, the ACP has also been observed as a component of mitochondrial multisubunit complexes, like the NADH:ubiquinone oxidoreductase (complex 1) (Fiedorczuk et al., 2016; Zhu et al., 2016) or the iron-sulfur cluster (ISC) assembly machinery (Boniecki et al., 2017). In addition, recent structural studies found ACP attached to assembly intermediates of both the human mitoribosomal LSU (Brown et al., 2017) and trypanosomal mitoribosomal SSU (Saurer et al., 2019). In all these complexes, the ACPs and their covalently linked acyl-phosphopantetheine moieties specifically interact with proteins

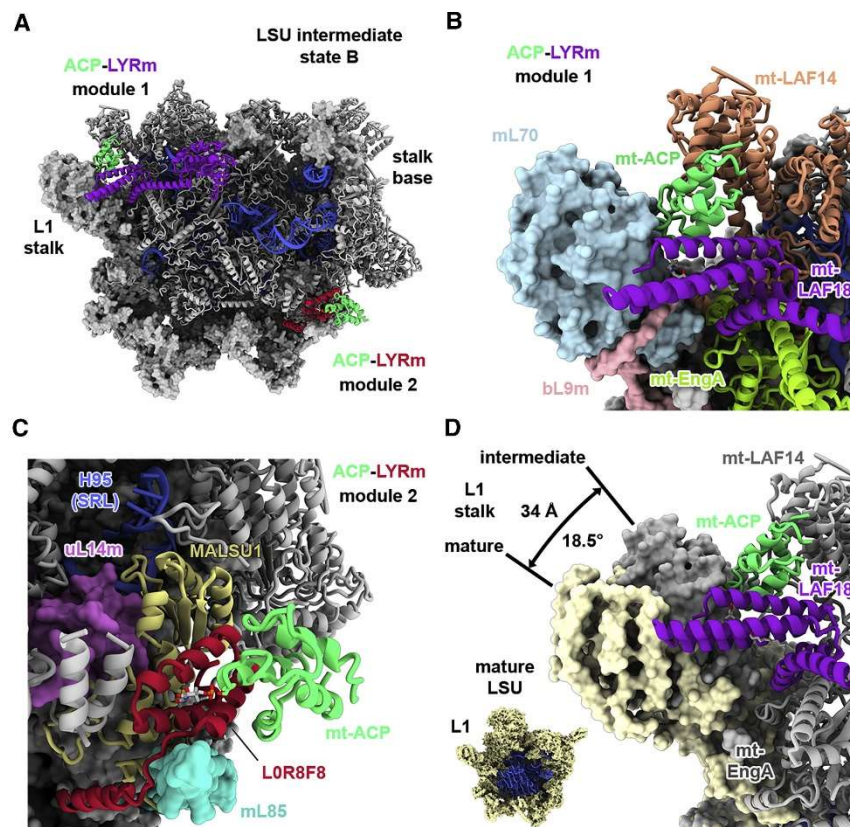


Figure 6. The ACP-LYRm modules in the LSU assembly intermediates

(A) An overview of the state B assembly intermediate is shown from the intersubunit side. The ribosomal proteins are represented as surfaces and the assembly factors as illustrations. (B and C) The ACP-LYRm modules 1 (B) and 2 (C) are presented as close-up views. (D) Models of state B (gray) and of the mature LSU (yellow) are overlaid to indicate the conformational shift of the L1 stalk by 34 Å (18.5°) induced by the ACP-LYRm module 1. In the inset, the mature LSU with proteins in yellow and the 12S rRNA in blue are shown for orientation. See also Figure S4D.

that contain a LYR-motif (LYRm) characterized by consecutive leucine, tyrosine and arginine residues (Figure 6 and S4D).

Interestingly, we found two such ACP-LYRm modules as architectural components of the trypanosomal LSU assembly intermediates (Figure 6A). Module 1, in which mt-LAF18 contributes the LYR motif is present in both states and located near the L1 stalk (Figure 6B). Besides the interaction with mt-LAF18, the ACP acts as bridge between mt-LAF14 and ribosomal proteins mL70 and mL74 of the L1 stalk, causing a tilt of the L1 stalk by 34 Å (18.5°) towards the CP region of the subunit in comparison to the conformation in the mature LSU (Figure 6D). Module 2 is observed only in state B near the SRL (H95), where it replaces state A specific factors. There, the ACP binds the LYRm containing protein L0R8F8, which in turn interacts with mitochondrial assembly factor MALSU1 forming the MALSU1-L0R8F8-ACP complex (Figure 6C and S6D) that was previously observed bound to the late state intermediate of the human mitoribosomal LSU (Brown et al., 2017). Similar as in the human LSU assembly intermediates, this complex interacts with uL14m that joins the *T. brucei* LSU upon progression to state B. Brown and colleagues suggested that the MALSU1-L0R8F8-ACP module prevents the association of the mitoribosomal SSU to the immature LSU through steric clashes. Both ACP-LYRm modules found in the *T. brucei* assembly intermediates would accomplish the suggested function.

Discussion

Whereas bacterial and eukaryotic cytosolic ribosome maturation has been extensively studied in the past (Bassler and Hurt, 2018; Davis and Williamson, 2017), the assembly of mitoribosomes is relatively poorly understood. However, the advances in electron microscopy and the recent breakthroughs in determining atomic structures of mature mitoribosomes (Amunts et al., 2015; Desai et al., 2017; Greber et al., 2015) now permit structural and mechanistic investigations of the mitoribosome biogenesis in different organisms.

Here, we present the atomic cryo-EM structures of two mitoribosomal LSU assembly intermediates, referred to as state A and B (Figure 1) that were prepared from wild-type *T. brucei* cells. In both states, the ribosomal proteins and the 12S rRNA elements located on the solvent accessible side, which does not contact the SSU, are in their mature state. However, the 12S rRNA elements that form the key functional

elements, such as the tRNA binding sites, the PTC and the upper part of the polypeptide exit tunnel, are held in immature conformations stabilized by an extensive protein network formed by multiple assembly factors. The observed states agree with the assembly sequence observed for the mammalian mitoribosomal LSU, where the PTC folds last (Brown et al., 2017). It appears that protein-rich mitoribosomes follow the established order of eukaryotic large ribosomal subunit assembly (Konikkat and Woolford, 2017), where the ribosomal protein shell forms early during the maturation process and assembles almost independently of the rRNA core.

The structures provide additional evidence that the assembly of mitoribosomes occurs through hierarchical assembly of preformed clusters of proteins (Figure 7), as previously suggested by biochemical experiments (Bogenhagen et al., 2018; Zeng et al., 2018). During transition from intermediate state A to B, at least nine assembly factors forming two separate clusters at the lower intersubunit side of state A are replaced by four mitoribosomal proteins and five new assembly factors. The modular exchange is accompanied by conformational changes of the 12S rRNA and mitoribosomal protein elements. During the transition from assembly intermediate state B to the mature LSU, which probably includes multiple steps and intermediates, all the remaining assembly factors have to leave such that the 12S rRNA core, including the PTC, can adopt its mature fold. These observations suggest that even the previously described mitoribosomal large subunit (Ramrath et al., 2018) may

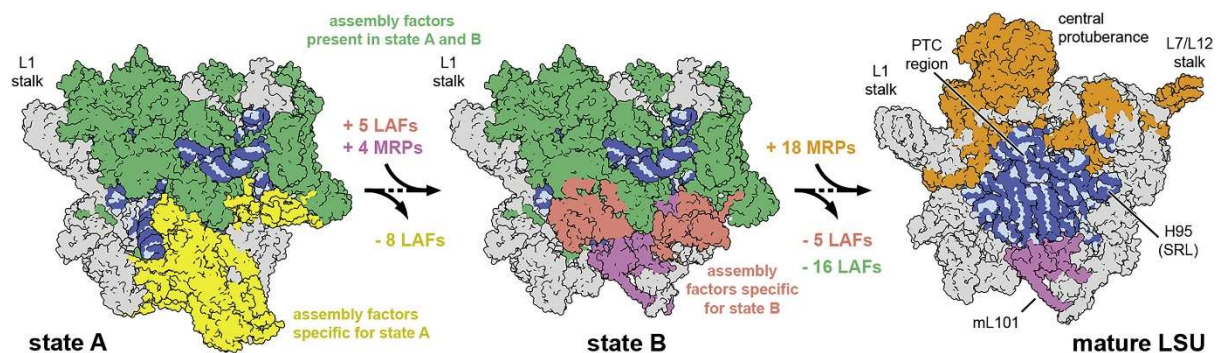


Figure 7. The Assembly Process of the *T. brucei* Mitochondrial LSU

The structures of the mitoribosomal LSU assembly intermediates states A and B and of the mature LSU, including a modeled 12S rRNA, are represented as surfaces from the intersubunit side. They are ordered in the most likely sequence of assembly, based on their structural features. Assembly factors are colored green (states A and B), yellow (specific for state A), and red (specific for state B). Mitoribosomal proteins are colored gray (states A and B and mature LSU), violet (in state B and mature LSU), and orange (mature LSU). The 12S rRNA is colored in blue. Landmarks of the LSU and selected elements are labeled.

represent a very late assembly intermediate with still unstructured PTC, and possibly some assembly factors still bound to the exit region of the large ribosomal subunit as described for the *Leishmania tarentolae* mitoribosome (Soufari et al., 2020). Multiple mitoribosomal proteins have to join state B to form the missing parts of the LSU, in particular the CP and elements of the L1 and the L7/L12 stalks. Considering that in the *T. brucei* mitoribosome the CP is composed entirely of ribosomal proteins, it is likely that it joins as a preassembled complex. In fact, classification of our particle datasets revealed further states of assembly intermediates that probably occur between state B and the mature LSU, but could not be resolved to high resolution (Figure S1). However, their structural features support the idea that the CP joins as a module and incorporates stepwise through distinct conformational states until it adopts its mature position. Likewise, it was proposed that CP components associate as a module during assembly of yeast mitoribosomes (Zeng et al., 2018).

Our structures agree well with the proposed assembly order of the yeast 54S subunit (Zeng et al., 2018) and probably correspond to an intermediate stage (p254S) in the yeast maturation pathway (Figure S7C). Nevertheless, there are few exceptions, possibly due to the different protein composition and architecture of trypanosomal mitoribosomes. The similarities to the order of events proposed for the mammalian 39S subunit assembly pathway are less obvious (Figure S7D) (Bogenhagen et al., 2018). In particular, the proteins forming the CP are incorporated at early stages of mammalian 39S maturation in contrast to the observations for the yeast and trypanosomal LSU maturation. Although mitoribosomes diverged considerably from bacterial ribosomes, the set of ribosomal proteins still missing in the trypanosomal mitoribosomal LSU intermediates matches the ones missing in the late state intermediates of the bacterial LSU (Figure S7B) (Jomaa et al., 2014; Li et al., 2013; Nikolay et al., 2018).

The assembly of trypanosomal mitoribosomes is assisted by numerous assembly factors with 25 LAFs present in state A and 19 LAFs in state B. Comparison based on sequence and structural features revealed that many of the observed LAFs are homologous to ribosomal assembly factors previously described in bacteria or in mitochondria (Figure S6). In particular, the module formed by MALSU1, L0R8F8 and mt-ACP was found in late-state intermediates of the human 39S subunit (Brown et al., 2017) indicating that the observations described here may be applicable for understanding mitoribosomal assembly pathways in other organisms. Furthermore,

some factors that were known to participate in mitoribosome biogenesis, such as Mtg1 and mt-EngA•GTP2 (Gupta et al., 2018; Kim and Barrientos, 2018; Kotani et al., 2013), are described here for the first time in complex with the immature mitoribosome helping to understand their molecular function. The GTPases EngA•GTP2, EngB•GTP and Mtg1 probably play an active role in the assembly process by inducing conformational changes within the assembly that control the release and binding of assembly factors and mitoribosomal proteins. Since they interact with such an extensive region of the intersubunit side, they might also sense a particular conformation of the 12S rRNA. Therefore, it is plausible that the observed intermediates correspond to some of the rate-limiting steps during assembly that are resolved only when a certain conformation of the 12S rRNA leads to GTP hydrolysis and dissociation of the GTPases. Furthermore, the GTPases may link mitoribosome biogenesis to the mitochondrial GTP/GDP ratio, similarly as proposed for the GTPases involved in cytoplasmic ribosome assembly, linking ribosomal maturation to the cellular energy level (Britton, 2009). Other assembly factors that show structural homology to enzymes, such as mt-LAF4 homologous to the tRNA pseudouridine synthase TruD, have lost their enzymatic activity. They probably act as a scaffold or specifically recognize important elements of the 12S rRNA, thereby promoting their correct folding. Structural homologues and functional analogues of the newly identified assembly factors may also play a role in mitoribosome maturation in other eukaryotes, including humans.

In conclusion, presented structures of two late stage assembly intermediates of the *T. brucei* mitoribosomal LSU provide a wealth of information that advances our understanding of ribosomal biogenesis. The numerous identified assembly factors provide an excellent starting point for future biochemical and functional studies of mitoribosomal maturation in trypanosomes and other eukaryotes, including humans. Furthermore, the created RNAi knockdown strains present an interesting system for further structural analysis of other mitochondrial LSU assembly intermediates. Considering that trypanosomes are parasites causing severe diseases in humans and domestic animals and that mitochondrial translation is essential for the disease-causing bloodstream form of trypanosomes, components of the discovered assembly pathway may serve as a possible drug targets for treatment against such diseases (Niemann et al., 2011).

Acknowledgments

We thank Martin Saurer and Ahmad Jomaa for critically reading the manuscript and helpful discussions. We also thank Mauro Fischli for his help at the early stage of the biochemical work and Bernd Schimanski for the BS19.3 single marker cell line. The cryo-EM data was collected at the Scientific Center for Optical and Electron Microscopy (ScopeM) at ETH Zurich, and we thank P. Tittmann and M. Peterek for the support. The cryo-EM data was processed on the Leonhard computing cluster of the Swiss National Supercomputing Centre (CSCS). This work was supported by the Swiss National Science Foundation (SNSF) and the National Center of Competence in Research (NCCR) RNA & Disease program of the SNSF. D.J.F.R. was supported by a FEBS long-term fellowship. S. M. was supported by an EMBO long-term fellowship (ALTF 793-2017) and by a Human Frontier Science Program long-term fellowship (LT000008/2018-L).

Author contributions

M.N., D.J.F.R., S.C. and E.H. prepared the *T. brucei* cell cultures and purified the mitochondrial vesicles. M.N. and S.C. prepared the transgenic *T. brucei* cell lines and performed the RNAi experiments. M.N., S.C. and A.S. designed and analyzed the *T. brucei* experiments. D.J.F.R. and S.M. purified the *T. brucei* mitoribosomal particles and prepared the cryo-EM grids. D.J.F.R., S.M. and D.B. collected the cryo-EM data of the mitoribosome sample. D.J.F.R., S.M. and M.J. calculated the cryo-EM density maps. D.J.F.R. and P.B. built the initial atomic models. M.L. and M.J. refined and validated the final molecular models. M.J., P.B., D.J.F.R., M.L. and N.B. interpreted the structures. P.B., M.J., M.N. and S.C. created the figures. M.J., P.B. and N.B. wrote the manuscript. All authors contributed to the final version of the manuscript.

Declaration of interests

All authors declare no competing interests.

STAR★Methods

Key Resources Table

REAGENT or RESOURCE	SOURCE	IDENTIFIER
Chemicals, Peptides, and Recombinant Proteins		
Sorbitol	Sigma	85529
Nycodenz	Alere Technologies AS	1002424
DNase I from bovine pancreas	Roche	10104159001
IgG Sepharose 6 Fast Flow	GE Healthcare	17-0969-01
Deposited Data		
Cryo-EM density map of assembly intermediate of <i>T. brucei</i> mitoribosomal LSU state A	This study	EMDB-10999
Cryo-EM density map of assembly intermediate of <i>T. brucei</i> mitoribosomal LSU state B	This study	EMDB-11000
Atomic model of assembly intermediate of <i>T. brucei</i> mitoribosomal LSU state A	This study	PDB: 6YXX
Atomic model of assembly intermediate of <i>T. brucei</i> mitoribosomal LSU state B	This study	PDB: 6YXy
Experimental Models: Cell Lines		
BS19.3 for 427-based RNAi cell lines	Saurer et al., 2019	n/a
mt-LAF1 RNAi	This study	n/a
mt-LAF2 RNAi	This study	n/a
mt-LAF3 RNAi	This study	n/a
mt-LAF4 RNAi	This study	n/a
mt-LAF5 RNAi	This study	n/a
mt-LAF17 RNAi	This study	n/a
mt-LAF21 RNAi	This study	n/a
mt-LAF26 RNAi	This study	n/a
Experimental Models: Organisms/Strains		
<i>Trypanosoma brucei</i> Lister strain 427		
<i>Trypanosoma brucei</i> Lister strain 29-13		
Oligonucleotides		
For oligonucleotides used in this study see Table S12		
Recombinant DNA		
n/a		

Software and Algorithms		
EPU	Thermo Fisher Scientific	https://www.fei.com/software/epu/
MotionCor2	Zheng et al., 2017	http://msg.ucsf.edu/em/software/motioncor2.html
GCTF	Zhang, 2016	https://www.mrc-lmb.cam.ac.uk/kzhang/
Relion-3	Zivanov et al., 2018	https://www3.mrc-lmb.cam.ac.uk/relion/index.php/Main_Page
Phyre2	Kelley et al., 2015	http://www.sbg.bio.ic.ac.uk/phyre2/html/page.cgi?id=index
Coot 0.8.9.1	Emsley et al., 2010	http://www2.mrc-lmb.cam.ac.uk/Personal/pemsley/cool/
Phenix	Adams et al., 2010	https://www.phenix-online.org/
Other		
Carbon coated holey copper grids R 2/2	Quantifoil	N/A

Resource Availability

Lead Contact

Further information and requests for resources and reagents should be directed to and will be fulfilled by the Lead Contact, Nenad Ban (ban@mol.biol.ethz.ch)

Materials Availability

Cell lines generated in this study will be made available on request by the Lead Contact with a completed Materials Transfer Agreement (MTA).

Data and Code Availability

The cryo-EM reconstructions of the assembly intermediates of the trypanosomal mitoribosomal LSU have been deposited in the Electron Microscopy Data Bank (EMDB) under ID codes EMDB: 10999 (state A) and EMDB: 11000 (state B). The corresponding atomic models have been deposited in the Protein Data Bank (PDB) under ID codes PDB: 6YXX (state A) and PDB: 6YXY (state B).

Experimental Model and Subject Details

Trypanosoma brucei strains

Trypanosoma brucei cells were grown in suspension culture at 27°C in SDM-79 (Brun and Schönenberger, 1979) supplemented with 7.5 mg/L Hemin and 5% (v/v) heat-inactivated fetal calf serum (FCS) for strain 427 (Cross, 1975) or 10% (v/v) FCS for strain 29-13, (Wirtz et al., 1999). Cells were maintained in disposable 50 mL culture flasks (25 cm²) with closed lids in a temperate incubator and diluted accordingly to keep the cells in the exponential growth phase (density ca. 2×10^5 to 6×10^7 cells/mL). For large scale preparations of mitochondrial vesicles (see below), cells were grown in 2L Erlenmeyer flasks to a density of up to 6×10^7 cells/mL in a total volume of 1-1.5 L at 27°C and shaking at 120 rpm. The vesicle preparation for small to large scale is described in detail in Niemann and Schneider (2020).

Method Details

Transgenic cell lines

RNAi-competent cell line based on *Trypanosoma brucei* strain 427 (Cross, 1975) was used to generate the mt-LAF knockdown cell lines (phleomycin single marker cells, gift from B. Schimanski, University of Bern), whereas strain 29-13 (Wirtz et al., 1999) was used for generating the cell lines targeting mS29/mS54 and uL15m with RNAi. All these constructs were based on a derivate of the stem-loop vector pLEW100 (Wirtz et al., 1999) using the following inserts for the RNAi construct: mt-LAF1 (Tb927.7.1640) ORF nt 521-991, mt-LAF2 (Tb927.11.12930) ORF nt 918-1324, mt-LAF3 (Tb927.9.3350) ORF nt 407-877, mt-LAF4 (Tb927.11.5990) ORF nt 759-1228, mt-LAF5 (Tb927.9.12850) ORF nt 242-710, mt-LAF17 (Tb927.11.16990) ORF nt 731-1157, mt-LAF21 (Tb927.7.3510) ORF nt 240-662, mt-LAF26/KRIPP3 (Tb927.1.1160) ORF nt 385-863. Transfection and selection of clones of the above-mentioned strains was done as described (Waldman, 2004).

Growth curves

T. brucei cells were inoculated to a density of 1×10^6 cells/mL. The culture was divided and one half was induced for RNAi with 1 µg/mL tetracycline (tet). Cells were counted approximately every 24 hours and diluted to 1×10^6 cells/mL accordingly.

Preparation of mitochondrial vesicles

Trypanosoma brucei strain 427 (Cross, 1975) was used for preparation of mitochondrial vesicles and the detailed protocol is described in Niemann and Schneider (2020). Briefly, *T. brucei* cells (ca. 20 L, up to 1×10^{12} cells) were harvested by centrifugation (e.g., 7,100rpm/11,000 x g at 4°C for 10 min in a Fiberlite F9-6x1000 LEX rotor) and washed once in 1X SBG (20 mM sodium phosphate, pH 7.9; 20 mM glucose; 0.15 M NaCl). The cells were lysed at isotonic conditions by nitrogen cavitation at a cell density of $\sim 2.0 \times 10^9$ cells/mL in isotonic 1X SoTE (600 mM sorbitol, 20 mM Tris-HCl pH 7.5, 1 mM EDTA) and by applying 70 bar for 45-60 min. The mitochondrial fraction was pelleted using centrifugation (16,000 rpm, 10 min, 4°C, Sorvall SS-34 rotor) and resuspended in 1X SoTE. To remove nuclear DNA contaminations and membrane fragments, the sample was treated with DNase I (100 µg/ml) for 20-30 min on ice. In a first centrifugation (555 x g, 20 min, 4°C, centrifuge Eppendorf 5810 R with rotor A-4-81, rectangular bucket 500 mL and adaptor for five conical tube 50 mL), cell debris and living cells were separated from the mitochondrial vesicles remaining in the supernatant. The pellet was resuspended in 1X SoTE and the centrifugation was repeated to further extract mitochondrial vesicles.

In a second centrifugation run (16,000 rpm, 10 min, 4°C, Sorvall SS-34 rotor) the mitochondrial vesicles were pelleted and immediately resuspended in 1X SoTE buffer containing 50% (w/v) Nycodenz. The suspension was syringed to the bottom of precast Nycodenz step gradients (18/21/25/28% (w/v) Nycodenz in 1X SoTE buffer; capacity $3.5-8 \times 10^{10}$ cells) using a Sanitex Eterna Matic syringe. The gradients were centrifuged at 27,000 rpm for 45 min at 4°C in a SW32 Ti rotor (Beckman Coulter). Mitochondrial vesicles accumulated at the borders between 21% and 25% (w/v) Nycodenz and were harvested using a syringe. Starting with 20 L of cell culture ($3.5-5 \times 10^7$ cells/ml) usually yielded in ~ 10 g wet weight of mitochondrial vesicles.

Native *T. brucei* mitoribosome purification

Mitochondrial vesicles (approx. 12 ml) were thawed on ice and pelleted by centrifugation (20,800 x g, 10 min, 4°C). The pellet was resuspended in an equal volume (12 ml) of lysis buffer (40 mM HEPES-KOH pH 7.4, 5 mM $\text{Na}_2\text{H}/\text{NaH}_2\text{PO}_4$ pH 7.4, 100 mM KCl, 10 mM MgCl_2 , 3% (w/v) DDM, 2 mM DTT, 2.5 mM EDTA 10 µM bestatin, 2 µM E-64, 10 µM leupeptin, 1 µM pepstatine, 10 µM phenanthroline, 100 µM PMSF, 20 U/ml RiboLock (ThermoFisher Scientific), 125 µM spermine, 125 µM

spermidine) and mitochondria were lysate by gentle mixing for 40 min at 4°C. The sample was centrifuged twice (20,800 x g, 25 min, 4°C) to clear the lysate. The cleared lysate was loaded onto a 60% (w/v) sucrose cushion in lysis buffer and centrifuged (65,000 rpm, 20 h 40 min, 4°C) using MLA-80 rotor (Beckman-Coulter). The pellets were then resuspended in 125 µl resuspension buffer (40 mM HEPES-KOH pH 7.4, 5 mM Na₂H/NaH₂ PO₄ pH 7.4, 100 mM KCl, 10 mM MgCl₂, 2 mM DTT, 0.01% (w/v) DDM) for 75 min at 4°C by gentle mixing. The sample was again cleared by centrifugation (20,800 x g, 10 min, 4°C). The supernatant was subsequently loaded onto a 10%–40% (w/v) sucrose gradient in resuspension buffer and centrifuged (45,000 rpm, 1 h 30 min, 4°C) using a SW55 Ti rotor (Beckman-Coulter). The sample was manually fractionated from the top into 13 equal fractions. Fractions 4-6 were combined and buffer-exchanged to resuspension buffer in a tabletop centrifuge at 4°C using centrifugal filters (Amicon) until the calculated sucrose concentration was below 1%.

Cryo-EM sample preparation and data acquisition

The buffer-exchanged sample was diluted 3 x with resuspension buffer to a final RNA concentration of 80 ng/µl. Quantifoil grids (R 2/2) were coated with a thin layer of carbon and glow discharged for 15 s at 15 mA. The sample (3.5 µl) was applied onto the grid, immediately blotted for 7-9 s using a Vitrobot Mark IV (Thermo Fisher Scientific) at 100% humidity and 4 °C and plunge frozen in a liquid ethane–propane mix cooled to liquid nitrogen temperature.

The cryo-EM data of the LSU native sample was collected on a Titan Krios cryo-transmission electron microscope (Thermo Fisher Scientific) equipped with a Falcon III direct electron detector (Thermo Fisher Scientific) and operating at 300 keV. Two datasets of 14,303 and 15,757 micrographs, respectively, were automatically collected using the EPU software (Thermo Fisher Scientific). A stack of 24 images was recorded for each micrograph at a defocus range between –1 to –3 µm. The exposure time was 1.3 s and the calibrated magnification was 129,000x (corresponding to a pixel size of 1.085 Å/pixel on the object scale), resulting in a total electron dose of ~75 electrons/Å².

Cryo-EM data processing of the mitoribosomal sample

Both datasets were collected and initially processed independently. Movie frames of both datasets were drift-corrected and dose-weighted using MotionCor2 (Zheng et al., 2017). GCTF (Zhang, 2016) was used to estimate the CTF parameters

of non-dose-weighted and drift-corrected micrographs. Based on the power spectra, 13,503 and 13,273 micrographs, respectively, were selected for further processing. Subsequent data processing was carried out using Relion 3 (Zivanov et al., 2018), unless specified differently. 1,243,430 and 1,237,180 particles from dataset I and dataset II, respectively, were picked by a template-free auto-picking procedure based on a Laplacian-of Gaussian (LoG) filter. Initial 2D classification was used in processing of both datasets to remove featureless particles. Selected particles from dataset I, which was processed first, were subjected to another round of 2D classification, from which particles in LSU-like looking class averages were selected. A limited number of 2D classes were used for *ab-initio* model creation. One class of 3D *ab-initio* model creation showed an LSU-like map, with the central protuberance (CP) region missing and additional density at the ribosomal intersubunit side. This map, lowpass filtered to 50 Å, was used in 3D classification of particles from both datasets. Classes lacking an obvious density for the CP region and characterized by the additional density at the intersubunit side of the subunit were selected from both datasets and merged together, which resulted in 131,101 particles (5.3% of the starting particles). Joined particles were aligned using 3D refinement and submitted to a skip-alignment 3D classification focused on the CP region and bottom of the subunit (in the crown view) – two regions which in the refined map showed highly variable density. The classification resulted in one class representing the state A assembly intermediate, two classes representing unidentified states and the remaining classes, representing highly similar state B structures. State A contained 16,215 particles and subsequent refinement and postprocessing yielded a map resolved at 3.9 Å resolution. State B contained 98,508 particles and with following refinement, postprocessing and particle CTF refinement was resolved at 3.1 Å resolution. Two classes representing unidentified states were merged and subjected for another skip-alignment 3D classification with a focus mask around the CP region that showed the highest flexibility in the density. This classification resulted in four meaningful classes (out of 6 in total), which upon further individual refinement resulted in low resolution (9-13 Å) maps that seem to represent assembly intermediates at different stages, although the low resolution of these reconstructions prevented any further and detailed interpretation. For the processing scheme see Figures S1 and S2 for the quality of the cryo-EM map.

Model building and refinement

Published models for the proteins and rRNA of the previously published LSU (Ramrath et al., 2018) were docked into the cryo-EM maps using UCSF ChimeraX (Goddard et al., 2018) and adjusted in Coot (Emsley et al., 2010). Remaining unassigned densities was addressed manually. Initially, proteins were traced as poly-alanine chains and side chain densities were used to assign the most probable amino acid sequence, considering secondary structure and local chemical environment. The obtained partial sequences were subsequently used to search through the non-redundant protein sequence database of TriTrypDB (Aslett et al., 2010) or NCBI (Altschul et al., 1990) to identify the proteins. Phyre2 (Kelley et al., 2015) was utilized to obtain model structures based on amino acid sequence homology. For most of the identified proteins, Tb427 Lister strain amino acid sequences could be used. However, for some proteins the highly homologous sequence of Tb927 strain was taken due to sequence incompleteness in the Tb427 Lister strain (Table S1). The correct fit of the side chain densities was used for validation of the identified sequence. Sequence (BLAST by NCBI) or secondary structure (PDBeFold by EMBL-EBI) was used to identify homologous proteins. Most parts of the maps showed high-quality EM density features, which allowed an atomic interpretation. In some peripheral areas fragmented EM density with lower local resolution was observed, which impeded protein identification, and some stretches in well-ordered areas were too short for confident sequence assignment. These protein fragments were built as unassigned UNK residues. Similarly, areas of weaker EM density clearly encompassing rRNA features such as helices, stem-loops or single-stranded connections but unresolved base orientations were built as unassigned phosphate backbone. In the case of the H91-92 stemloop, in which the orientation, but not the identities of the bases could be established, the model was truncated to poly-pyrimidine.

The build models were initially corrected, completed and refined manually using Coot (Emsley et al., 2010). The final models were then subjected to five cycles of real space refinement using Phenix (Afonine et al., 2018), during which RNA base pair, RNA stacking, protein secondary structure, side chain rotamer and Ramachandran restraints were applied (Table 1). Using available high-resolution structures as guides, additional bond and angle restraints were imposed for some ligands, such as the coordinated zinc ions, covalently linked phosphopantetheine moieties as well as the GTPs with a hexa-coordinated magnesium. The model geometry was validated using

MolProbity. Real space correlation coefficients (CC_{mask}) between cryo-EM maps and the models were calculated to evaluate the fit. Further, the model versus map FSCs at the FSC = 0.5 criterion resulted in similar resolutions as those calculated from both map half-sets at the FSC = 0.143 criterion for both models.

Northern Analysis for mitochondrial rRNAs

The Northern analysis for mitochondrial 9S and 12S rRNAs steady-state levels was done as described in Saurer et al. (2019) and basically follows the acid guanidinium thiocyanate-phenol-chloroform RNA extraction method (Chomczynski and Sacchi, 1987). RNAi cell lines were grown in triplicates in the presence or absence of tetracycline. A minimum of 5×10^7 cells were harvested for each time point and washed with 1x PBS (phosphate buffered saline). Cell pellets were dissolved immediately in 4 M guanidinium isothiocyanate containing 200 mM sodium acetate pH 4.0, 25 mM sodium citrate, 0.5% (w/v) sodium N-lauroyl sarcosinate and 100 mM β -mercaptoethanol as well as 20 mg/mL oyster glycogen. The RNA was extracted and precipitated using 1.2 volumes of ice-cold isopropanol, and pellets were washed with 70% (v/v) ethanol. 5 μ g RNA containing 0.1% (w/v) ethidium bromide were separated in 1% (w/v) agarose gels containing 200 mM formaldehyde for 1 h 45 min at 100 V. The running buffer (20 mM MOPS, 8 mM sodium acetate, 1 mM EDTA, 200 mM formaldehyde, pH 7.0) was pumped continuously between the anode and cathode reservoirs using a peristaltic pump or subjected to interval mixing. The three prominent cytosolic rRNAs (2251, 1864 and ~1400 nt) were visualized and served as loading control. A capillary blot transferred the RNA onto a charged nylon membrane for ca. 16 h in 10x SSC (130 mM NaCl, 150 mM sodium citrate, pH 7.0). The membrane was UV-crosslinked (150 mJ/cm²) and dried, followed by northern hybridization using complementary DNA oligonucleotide probes for mitochondrial 9S and 12S rRNAs (Table S2). The membrane was pre-wetted in 0.2x SSPE (1.5 mM NaCl, 0.1 mM sodium phosphate, 0.01 mM EDTA, pH 7.4) and pre-hybridized for at least 1 h at 55°C in 10 mL of buffer containing 6x SSPE, 5x Denhardt's and 0.5% (w/v) SDS in a 51 mm diameter hybridization bottle. The buffer was discarded and the membrane was hybridized for 12-18 h at 55°C with 10 mL fresh buffer containing in addition 10 pmol 5'PNK- γ^{32} P-ATP labeled DNA probe for the 9S rRNA. The membrane was washed three times with ~50 mL washing solution (2x SSPE, 0.5% (w/v) SDS) for 3 min. The blot was exposed for three days and quantified with a Typhoon FLA 9500

Phosphorimager, followed by re-hybridization using the DNA probe for the 12S rRNA and exposure for one day.

Quantification and Statistical Analysis

The phosphorimager images were quantified using the Image Quant TL software (version 8.1). The signal intensities were used to calculate the average from biological triplicates. The average from uninduced cells (day = 0) was set to 100 and all other averaged time points were normalized accordingly in an unbiased manner. The error bars represent the average deviation calculated with MS Excel.

The statistical analysis of the cryo-EM data processing, model building and model refinement is described in Method Details and in the Supplemental Information.

Creation of Figures

Molecular graphics and analyses were performed with UCSF ChimeraX, developed by the Resource for Biocomputing, Visualization, and Informatics at the University of California, San Francisco, with support from National Institutes of Health R01-GM129325 and the Office of Cyber Infrastructure and Computational Biology, National Institute of Allergy and Infectious Diseases (Goddard et al., 2018).

References

- Adams, P.D., Afonine, P.V., Bunko' czi, G., Chen, V.B., Davis, I.W., Echols, N., Headd, J.J., Hung, L.-W., Kapral, G.J., Grosse-Kunstleve, R.W., et al. (2010). PHENIX: a comprehensive Python-based system for macromolecular structure solution. *Acta Crystallogr. D Biol. Crystallogr.* 66, 213–221.
- Afonine, P.V., Poon, B.K., Read, R.J., Sobolev, O.V., Terwilliger, T.C., Urzhumtsev, A., and Adams, P.D. (2018). Real-space refinement in PHENIX for cryo-EM and crystallography. *Acta Crystallogr D Struct Biology* 74, 531–544, <https://doi.org/10.1107/S2059798318006551>.
- Altschul, S.F., Gish, W., Miller, W., Myers, E.W., and Lipman, D.J. (1990). Basic local alignment search tool. *J. Mol. Biol.* 215, 403–410.
- Amunts, A., Brown, A., Toots, J., Scheres, S.H.W., and Ramakrishnan, V. (2015). Ribosome. The structure of the human mitochondrial ribosome. *Science* 348, 95–98.
- Anantharaman, V., Koonin, E.V., and Aravind, L. (2002). SPOUT: a class of methyltransferases that includes spoU and trmD RNA methylase superfamilies, and novel superfamilies of predicted prokaryotic RNA methylases. *J. Mol. Microbiol. Biotechnol.* 4, 71–75.
- Ansmant, I., Massenet, S., Grosjean, H., Motorin, Y., and Branlant, C. (2000). Identification of the *Saccharomyces cerevisiae* RNA:pseudouridine synthase responsible for formation of psi(2819) in 21S mitochondrial ribosomal RNA. *Nucleic Acids Res.* 28, 1941–1946.
- Antonicka, H., Choquet, K., Lin, Z.Y., Gingras, A.C., Kleinman, C.L., and Shoubbridge, E.A. (2017). A pseudouridine synthase module is essential for mitochondrial protein synthesis and cell viability. *EMBO Rep.* 18, 28–38.
- Aslett, M., Aurrecochea, C., Berriman, M., Brestelli, J., Brunk, B.P., Carrington, M., Depledge, D.P., Fischer, S., Gajria, B., Gao, X., et al. (2010). TriTrypDB: a functional genomic resource for the Trypanosomatidae. *Nucleic Acids Res.* 38, D457–D462.
- Barrientos, A., Korr, D., Barwell, K.J., Sjulsen, C., Gajewski, C.D., Manfredi, G., Ackerman, S., and Tzagoloff, A. (2003). MTG1 codes for a conserved protein required for mitochondrial translation. *Mol. Biol. Cell* 14, 2292–2302.
- Baßler, J., and Hurt, E. (2019). Eukaryotic Ribosome Assembly. *Annu. Rev. Biochem.* 88, 281–306.
- Bharat, A., Jiang, M., Sullivan, S.M., Maddock, J.R., and Brown, E.D. (2006). Cooperative and critical roles for both G domains in the GTPase activity and cellular function of ribosome-associated *Escherichia coli* EngA. *J. Bacteriol.* 188, 7992–7996.
- Bogenhagen, D.F., Ostermeyer-Fay, A.G., Haley, J.D., and Garcia-Diaz, M. (2018). Kinetics and Mechanism of Mammalian Mitochondrial Ribosome Assembly. *Cell Rep.* 22, 1935–1944.
- Boniecki, M.T., Freibert, S.A., Mu€hlenhoff, U., Lill, R., and Cygler, M. (2017). Structure and functional dynamics of the mitochondrial Fe/S cluster synthesis complex. *Nat. Commun.* 8, 1287.
- Britton, R.A. (2009). Role of GTPases in bacterial ribosome assembly. *Annu. Rev. Microbiol.* 63, 155–176.
- Brown, A., Rathore, S., Kimanius, D., Aibara, S., Bai, X.C., Rorbach, J., Amunts, A., and Ramakrishnan, V. (2017). Structures of the human mitochondrial ribosome in native states of assembly. *Nat. Struct. Mol. Biol.* 24, 866–869.
- Brun, R., and Schonenberger. (1979). Cultivation and in vitro cloning or procyclic culture forms of *Trypanosoma brucei* in a semi-defined medium. Short communication. *Acta Trop.* 36, 289–292.

- Chen, S.S., and Williamson, J.R. (2013). Characterization of the ribosome biogenesis landscape in *E. coli* using quantitative mass spectrometry. *J. Mol. Biol.* 425, 767–779.
- Chomczynski, P., and Sacchi, N. (1987). Single-Step Method of RNA Isolation by Acid Guanidinium Thiocyanate–Phenol–Chloroform Extraction. *Anal Biochem* 162, 156–159, <https://doi.org/10.1006/abio.1987.9999>.
- Cronan, J.E., Fearnley, I.M., and Walker, J.E. (2005). Mammalian mitochondria contain a soluble acyl carrier protein. *FEBS Lett.* 579, 4892–4896.
- Cross, G.A. (1975). Identification, purification and properties of clone-specific glycoprotein antigens constituting the surface coat of *Trypanosoma brucei*. *Parasitology* 71, 393–417.
- Davis, J.H., and Williamson, J.R. (2017). Structure and dynamics of bacterial ribosome biogenesis. *Philos. Trans. R. Soc. Lond. Ser. B Biol. Sci.* 372, 20160181.
- Davis, J.H., Tan, Y.Z., Carragher, B., Potter, C.S., Lyumkis, D., and Williamson, J.R. (2016). Modular Assembly of the Bacterial Large Ribosomal Subunit. *Cell* 167, 1610–1622.e15.
- de la Cruz, J., Karbstein, K., and Woolford, J.L., Jr. (2015). Functions of ribosomal proteins in assembly of eukaryotic ribosomes in vivo. *Annu. Rev. Biochem.* 84, 93–129.
- De Silva, D., Tu, Y.-T., Amunts, A., Fontanesi, F., and Barrientos, A. (2015). Mitochondrial ribosome assembly in health and disease. *Cell Cycle* 14, 2226–2250.
- De Silva, D., Poliquin, S., Zeng, R., Zamudio-Ochoa, A., Marrero, N., PerezMartinez, X., Fontanesi, F., and Barrientos, A. (2017). The DEAD-box helicase Mss116 plays distinct roles in mitochondrial ribogenesis and mRNA-specific translation. *Nucleic Acids Res.* 45, 6628–6643.
- Del Campo, M., and Lambowitz, A.M. (2009). Structure of the Yeast DEAD box protein Mss116p reveals two wedges that crimp RNA. *Mol. Cell* 35, 598–609.
- Desai, N., Brown, A., Amunts, A., and Ramakrishnan, V. (2017). The structure of the yeast mitochondrial ribosome. *Science* 355, 528–531.
- Emsley, P., Lohkamp, B., Scott, W.G., and Cowtan, K. (2010). Features and development of Coot. *Acta Crystallogr. D Biol. Crystallogr.* 66, 486–501.
- Fairman-Williams, M.E., Guenther, U.-P., and Jankowsky, E. (2010). SF1 and SF2 helicases: family matters. *Curr. Opin. Struct. Biol.* 20, 313–324.
- Fiedorczuk, K., Letts, J.A., Degliesposti, G., Kaszuba, K., Skehel, M., and Sazanov, L.A. (2016). Atomic structure of the entire mammalian mitochondrial complex I. *Nature* 538, 406–410.
- Goddard, T.D., Huang, C.C., Meng, E.C., Pettersen, E.F., Couch, G.S., Morris, J.H., and Ferrin, T.E. (2018). UCSF ChimeraX: meeting modern challenges in visualization and analysis. *Protein Sci.* 27, 14–25.
- Greber, B.J., Bieri, P., Leibundgut, M., Leitner, A., Aebersold, R., Boehringer, D., and Ban, N. (2015). Ribosome. The complete structure of the 55S mammalian mitochondrial ribosome. *Science* 348, 303–308.
- Gulati, M., Jain, N., Anand, B., Prakash, B., and Britton, R.A. (2013). Mutational analysis of the ribosome assembly GTPase RbgA provides insight into ribosome interaction and ribosome-stimulated GTPase activation. *Nucleic Acids Res.* 41, 3217–3227.
- Gupta, K., Gupta, A., Haider, A., and Habib, S. (2018). Characterization of mitochondrion-targeted GTPases in *Plasmodium falciparum*. *Parasitology* 145, 1600–1612.

- Hillman, G.A., and Henry, M.F. (2019). The yeast protein Mam33 functions in the assembly of the mitochondrial ribosome. *J. Biol. Chem.* 294, 9813–9829, <https://doi.org/10.1074/jbc.RA119.008476>.
- Hoang, C., Chen, J., Vizthum, C.A., Kandel, J.M., Hamilton, C.S., Mueller, E.G., and Ferre' D'Amare, A.R. (2006). Crystal structure of pseudouridine synthase RluA: indirect sequence readout through protein-induced RNA structure. *Mol. Cell* 24, 535–545.
- Hwang, J., and Inouye, M. (2006). The tandem GTPase, Der, is essential for the biogenesis of 50S ribosomal subunits in *Escherichia coli*. *Mol. Microbiol.* 61, 1660–1672.
- Jomaa, A., Jain, N., Davis, J.H., Williamson, J.R., Britton, R.A., and Ortega, J. (2014). Functional domains of the 50S subunit mature late in the assembly process. *Nucleic Acids Res.* 42, 3419–3435.
- Kelley, L.A., Mezulis, S., Yates, C.M., Wass, M.N., and Sternberg, M.J. (2015). The Phyre2 web portal for protein modeling, prediction and analysis. *Nat. Protoc.* 10, 845–858.
- Kim, H.J., and Barrientos, A. (2018). MTG1 couples mitoribosome large subunit assembly with intersubunit bridge formation. *Nucleic Acids Res.* 46, 8435–8453.
- Kim, H.J., Maiti, P., and Barrientos, A. (2017). Mitochondrial ribosomes in cancer. *Semin. Cancer Biol.* 47, 67–81.
- Klinge, S., and Woolford, J.L., Jr. (2019). Ribosome assembly coming into focus. *Nat. Rev. Mol. Cell Biol.* 20, 116–131.
- Konikkat, S., and Woolford, J.L., Jr. (2017). Principles of 60S ribosomal subunit assembly emerging from recent studies in yeast. *Biochem. J.* 474, 195–214.
- Kotani, T., Akabane, S., Takeyasu, K., Ueda, T., and Takeuchi, N. (2013). Human G-proteins, ObgH1 and Mtg1, associate with the large mitochondrial ribosome subunit and are involved in translation and assembly of respiratory complexes. *Nucleic Acids Res.* 41, 3713–3722.
- Li, N., Chen, Y., Guo, Q., Zhang, Y., Yuan, Y., Ma, C., Deng, H., Lei, J., and Gao, N. (2013). Cryo-EM structures of the late-stage assembly intermediates of the bacterial 50S ribosomal subunit. *Nucleic Acids Res.* 41, 7073–7083.
- Matsuo, Y., Morimoto, T., Kuwano, M., Loh, P.C., Oshima, T., and Ogasawara, N. (2006). The GTP-binding protein YlqF participates in the late step of 50 S ribosomal subunit assembly in *Bacillus subtilis*. *J. Biol. Chem.* 281, 8110–8117.
- Mohr, G., Del Campo, M., Mohr, S., Yang, Q., Jia, H., Jankowsky, E., and Lambowitz, A.M. (2008). Function of the C-terminal domain of the DEADbox protein Mss116p analyzed in vivo and in vitro. *J. Mol. Biol.* 375, 1344–1364.
- Ni, X., Davis, J.H., Jain, N., Razi, A., Benlekbir, S., McArthur, A.G., Rubinstein, J.L., Britton, R.A., Williamson, J.R., and Ortega, J. (2016). YphC and YsxC GTPases assist the maturation of the central protuberance, GTPase associated region and functional core of the 50S ribosomal subunit. *Nucleic Acids Res.* 44, 8442–8455.
- Niemann, M., and Schneider, A. (2020). A Scalable Purification Method for Mitochondria from *Trypanosoma brucei*. *Methods Mol. Biol.* 2116, 611–626.
- Niemann, M., Schneider, A., and Cristodero, M. (2011). Mitochondrial translation in trypanosomatids: a novel target for chemotherapy? *Trends Parasitol.* 27, 429–433.
- Nikolay, R., Hilal, T., Qin, B., Mielke, T., Buërger, J., Loerke, J., Textoris-Taube, K., Nierhaus, K.H., and Spahn, C.M.T. (2018). Structural Visualization of the Formation and Activation of the 50S Ribosomal Subunit during In Vitro Reconstitution. *Mol. Cell* 70, 881–893.e3.

- Ott, M., Amunts, A., and Brown, A. (2016). Organization and Regulation of Mitochondrial Protein Synthesis. *Annu. Rev. Biochem.* 85, 77–101.
- Pintard, L., Bujnicki, J.M., Lapeyre, B., and Bonnerot, C. (2002). MRM2 encodes a novel yeast mitochondrial 21S rRNA methyltransferase. *EMBO J.* 21, 1139–1147.
- Purta, E., O'Connor, M., Bujnicki, J.M., and Douthwaite, S. (2008). YccW is the m5C methyltransferase specific for 23S rRNA nucleotide 1962. *J. Mol. Biol.* 383, 641–651.
- Putnam, A.A., and Jankowsky, E. (2013). DEAD-box helicases as integrators of RNA, nucleotide and protein binding. *Biochim. Biophys. Acta* 1829, 884–893.
- Ramrath, D.J., Niemann, M., Leibundgut, M., Bieri, P., Prange, C., Horn, E.K., Leitner, A., Boehringer, D., Schneider, A., and Ban, N. (2018). Evolutionary shift toward protein-based architecture in trypanosomal mitochondrial ribosomes. *Science* 362, eaau7735.
- Roger, A.J., Muñoz-Gómez, S.A., and Kamikawa, R. (2017). The Origin and Diversification of Mitochondria. *Curr. Biol.* 27, R1177–R1192.
- Rorbach, J., Boesch, P., Gammage, P.A., Nicholls, T.J., Pearce, S.F., Patel, D., Hauser, A., Perocchi, F., and Minczuk, M. (2014). MRM2 and MRM3 are involved in biogenesis of the large subunit of the mitochondrial ribosome. *Mol. Biol. Cell* 25, 2542–2555.
- Ruzheinikov, S.N., Das, S.K., Sedelnikova, S.E., Baker, P.J., Artymiuk, P.J., García-Lara, J., Foster, S.J., and Rice, D.W. (2004). Analysis of the open and closed conformations of the GTP-binding protein YsxC from *Bacillus subtilis*. *J. Mol. Biol.* 339, 265–278.
- Saurer, M., Ramrath, D.J.F., Niemann, M., Calderaro, S., Prange, C., Mattei, S., Scaiola, A., Leitner, A., Bieri, P., Horn, E.K., et al. (2019). Mitoribosomal small subunit biogenesis in trypanosomes involves an extensive assembly machinery. *Science* 365, 1144–1149.
- Schaefer, L., Uicker, W.C., Wicker-Planquart, C., Foucher, A.-E., Jault, J.-M., and Britton, R.A. (2006). Multiple GTPases participate in the assembly of the large ribosomal subunit in *Bacillus subtilis*. *J. Bacteriol.* 188, 8252–8258.
- Seffouh, A., Jain, N., Jahagirdar, D., Basu, K., Razi, A., Ni, X., Guarneri, A., Britton, R.A., and Ortega, J. (2019). Structural consequences of the interaction of RbgA with a 50S ribosomal subunit assembly intermediate. *Nucleic Acids Res.* 47, 10414–10425.
- Sengoku, T., Nureki, O., Nakamura, A., Kobayashi, S., and Yokoyama, S. (2006). Structural basis for RNA unwinding by the DEAD-box protein *Drosophila* Vasa. *Cell* 125, 287–300.
- Shajani, Z., Sykes, M.T., and Williamson, J.R. (2011). Assembly of bacterial ribosomes. *Annu. Rev. Biochem.* 80, 501–526.
- Soufari, H., Waltz, F., Parrot, C., Durrieu, S., Bochler, A., Kuhn, L., Sissler, M., and Hashem, Y. (2020). Structure of the full kinetoplast mitoribosome and insight on its large subunit maturation. *bioRxiv*. <https://doi.org/10.1101/2020.05.02.073890>.
- Theissen, B., Karow, A.R., Köhler, J., Gubaev, A., and Klostermeier, D. (2008). Cooperative binding of ATP and RNA induces a closed conformation in a DEAD box RNA helicase. *Proc. Natl. Acad. Sci. USA* 105, 548–553.
- Tomar, S.K., Dhimole, N., Chatterjee, M., and Prakash, B. (2009). Distinct GDP/GTP bound states of the tandem G-domains of EngA regulate ribosome binding. *Nucleic Acids Res.* 37, 2359–2370.
- Uicker, W.C., Schaefer, L., and Britton, R.A. (2006). The essential GTPase RbgA (YlqF) is required for 50S ribosome assembly in *Bacillus subtilis*. *Mol. Microbiol.* 59, 528–540.

- Waldman, A.S. (2004). *Genetic Recombination: Reviews and Protocols* (Humana Press), pp. 53–86.
- Wirtz, E., Leal, S., Ochatt, C., and Cross, G.A. (1999). A tightly regulated inducible expression system for conditional gene knock-outs and dominant-negative genetics in *Trypanosoma brucei*. *Mol. Biochem. Parasitol.* 99, 89–101.
- Woolford, J.L., Jr., and Baserga, S.J. (2013). Ribosome biogenesis in the yeast *Saccharomyces cerevisiae*. *Genetics* 195, 643–681.
- Yang, H., Wang, Z., Shen, Y., Wang, P., Jia, X., Zhao, L., Zhou, P., Gong, R., Li, Z., Yang, Y., et al. (2010). Crystal structure of the nosiheptideresistance methyltransferase of *Streptomyces actuosus*. *Biochemistry* 49, 6440–6450.
- Zaganelli, S., Rebelo-Guiomar, P., Maundrell, K., Rozanska, A., Pierredon, S., Powell, C.A., Jourdain, A.A., Hulo, N., Lightowlers, R.N., ChrzanowskaLightowlers, Z.M., et al. (2017). The Pseudouridine Synthase RPUSD4 Is an Essential Component of Mitochondrial RNA Granules. *J. Biol. Chem.* 292, 4519–4532.
- Zeng, R., Smith, E., and Barrientos, A. (2018). Yeast Mitoribosome Large Subunit Assembly Proceeds by Hierarchical Incorporation of Protein Clusters and Modules on the Inner Membrane. *Cell Metab.* 27, 645–656.e7.
- Zhang, K. (2016). Gctf: Real-time CTF determination and correction. *J. Struct. Biol.* 193, 1–12.
- Zhang, X., Yan, K., Zhang, Y., Li, N., Ma, C., Li, Z., Zhang, Y., Feng, B., Liu, J., Sun, Y., et al. (2014). Structural insights into the function of a unique tandem GTPase EngA in bacterial ribosome assembly. *Nucleic Acids Res.* 42, 13430–13439.
- Zheng, S.Q., Palovcak, E., Armache, J.-P., Verba, K.A., Cheng, Y., and Agard, D.A. (2017). MotionCor2: anisotropic correction of beam-induced motion for improved cryo-electron microscopy. *Nat. Methods* 14, 331–332.
- Zhu, J., Vinothkumar, K.R., and Hirst, J. (2016). Structure of mammalian respiratory complex I. *Nature* 536, 354–358.
- Zivanov, J., Nakane, T., Forsberg, B.O., Kimanius, D., Hagen, W.J., Lindahl, E., and Scheres, S.H. (2018). New tools for automated high-resolution cryo-EM structure determination in RELION-3. *eLife* 7, e42166.

Supplemental Information

Structural Insights into the Mechanism of Mitoribosomal Large Subunit Biogenesis

Mateusz Jaskolowski^{1,3}, David J.F. Ramrath^{1,3}, Philipp Bieri^{1,3}, Moritz Niemann^{2,3}, Simone Mattei¹, Salvatore Calderaro², Marc Leibundgut¹, Elke K. Horn², Daniel Boehringer¹, Andre Schneider^{2,*} and Nenad Ban^{1,4,*}

¹Department of Biology, ETH Zurich, Zurich 8093, Switzerland

²Department of Chemistry and Biochemistry, University of Bern, Bern 3012, Switzerland

³These authors contributed equally

⁴Lead Contact

*Correspondence: andre.schneider@dcb.unibe.ch (A.S.), ban@mol.biol.ethz.ch (N.B.)

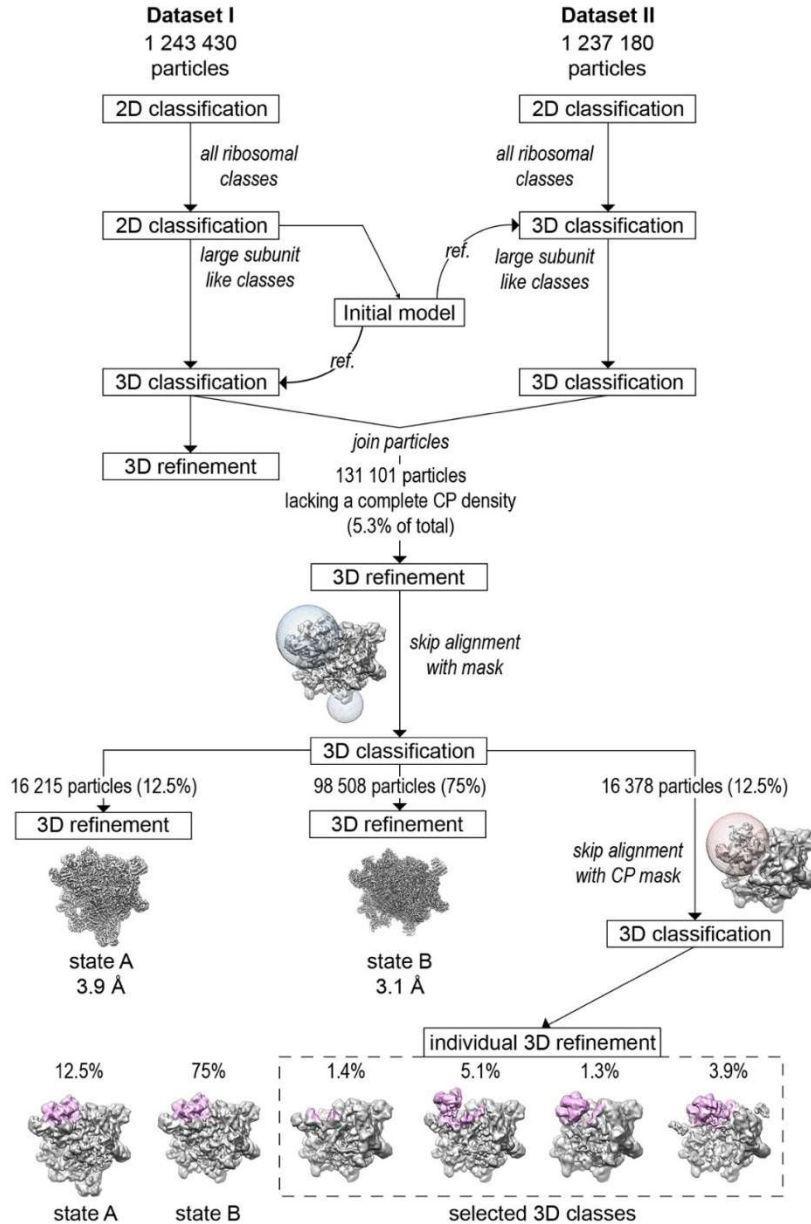


Figure S1. Cryo-EM data processing and reconstruction of the mt-LSU assembly intermediates. Related to STAR Methods

Processing scheme of the native *T. brucei* mitoribosome sample collected as two separate datasets. Particles in both datasets were picked using a reference-free method. Initially, both datasets were processed separately. Selected 2D classes from dataset I were used to generate an *ab initio* 3D model. After 3D classification, classes that represented mt-LSU, but lacked the complete density for the CP region and showed an extra density on the intersubunit side were joined and 3D refined. Subsequent focused 3D classification resulted in state A (12.5%) and state B (75%) assembly intermediates, which were resolved to 3.9 Å and 3.1 Å resolution, respectively. The remaining particles (12.5%) were refined and subjected to another round of 3D classification focused on the CP region; 4 additional classes with varying density in the CP region were identified and refined individually. The cryo-EM maps of all identified assembly intermediates are shown at the bottom of the figure lowpass filtered to 13 Å, with the CP region colored orchid.

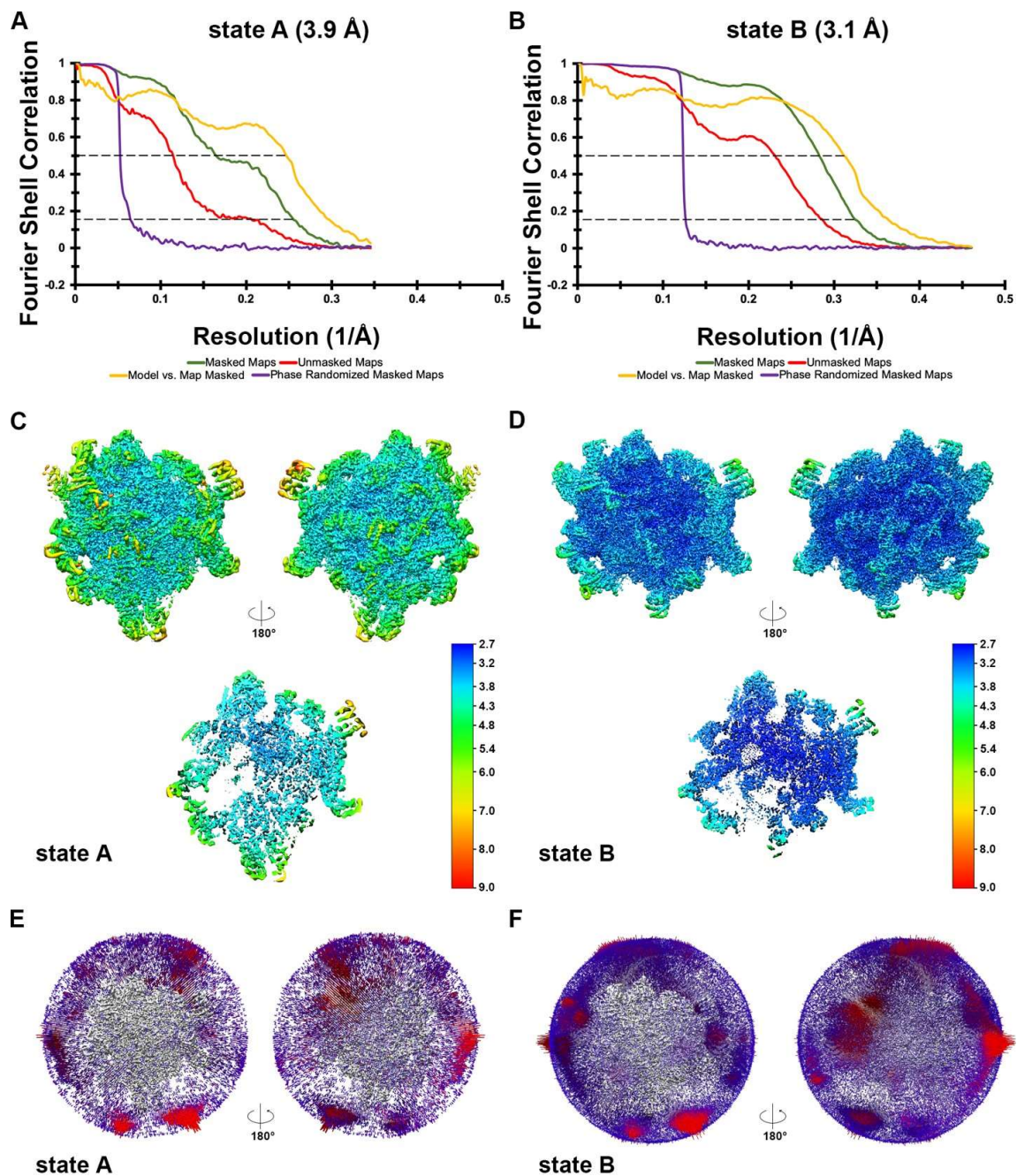


Figure S2. Data quality of the native sample. Related to STAR Methods

(A-B) Fourier shell correlation (FSC) curves of the cryo-EM maps of states A (A) and B (B) are shown as green lines. The overall resolutions of the different reconstructions are estimated using the FSC = 0.143 criterion. The model-vs-map FSC curves shown as yellow lines reveal a similar resolution using an FSC = 0.5 cutoff. (C-D) Local resolution map of states A (C) and B (D) shown from the intersubunit side and from the solvent accessible side. Additionally, a cross-section through the middle of the subunit is shown at the bottom of the respective panel. The local resolution of both maps is visualized according to the same color key. (E-F) Euler distribution plots for states A (E) and B (D) are shown from both the subunit interfaces and from the solvent accessible side.

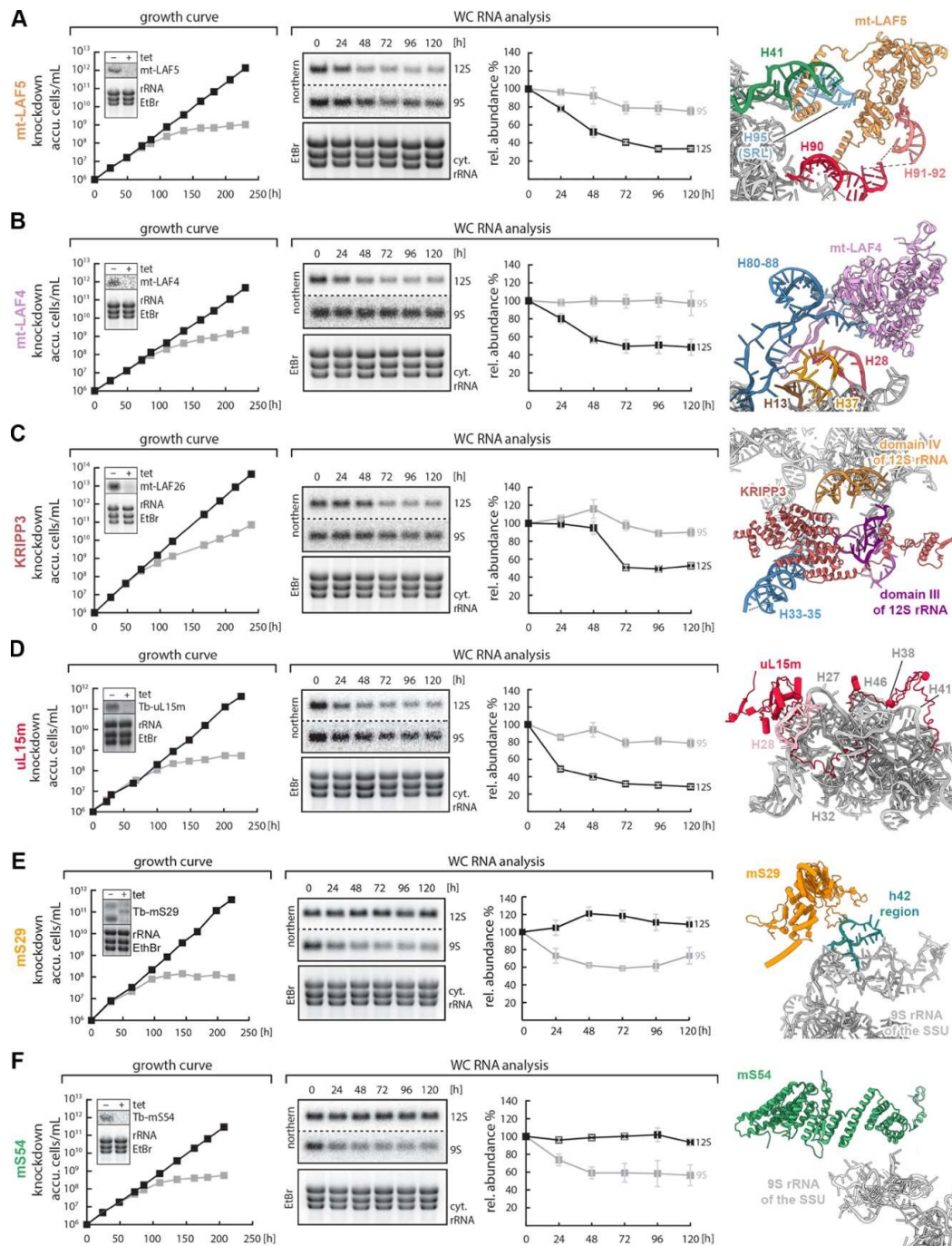


Figure S3. The growth rate and the stability of the mitochondrial rRNA is affected by assembly factors and ribosomal proteins. Related to Figure 2

RNAi-induced knockdown of the assembly factors *mt-LAF-5* (A), *mt-LAF4* (B) and *KRIPP3* (C) stalls cell cultures growth and causes a reduction in 12S rRNA levels. A knockdown of *uL15m* (D) was used as a positive control, and knockdowns of *mt-SSU* ribosomal proteins *mS29* (E) and *mS54* (F) were used as a negative control. The structure of *mt-LAF5* (A) and *mt-LAF4* (B) are shown as observed in state B, whereas *KRIPP3* (C) was taken from the state A assembly intermediate. The structural panel of *uL15m* (D) was created using the PDB: 6HIX model, whereas the panels with *mS29* (E) and *mS54* (F) were made from the PDB: 6HIZ model. Cultures were grown in triplicates. Error bars indicate the average deviation from the mean.

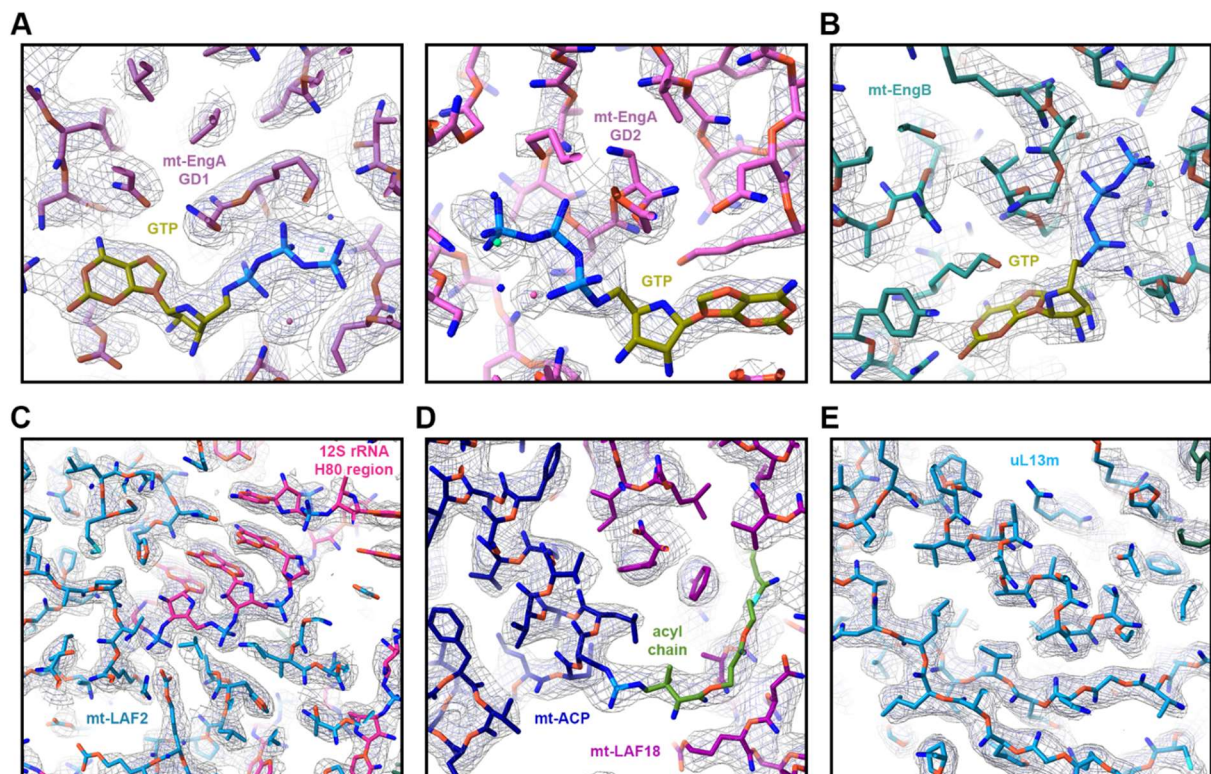


Figure S4. Cryo-EM map quality and model fit of the state B mt-LSU assembly intermediate. Related to STAR Methods

GTP molecules (teal) bound to the mt-EngA (purple) (A) and EngB (olive) (B) are shown. (C) A fragment of H80 is shown in purple with nearby assembly factor mt-LAF2 (yellow). (D) mt-ACP (red) and mt-LAF18 (purple), which are part of the ACP-LYRm module 1, are shown together with the covalently attached acylated phosphopantetheine prosthetic group (green). (E) Cryo-EM map of ribosomal protein uL13m (yellow). In all close-ups, the uncarved cryo-EM map is shown as black and red mesh at different contour levels.

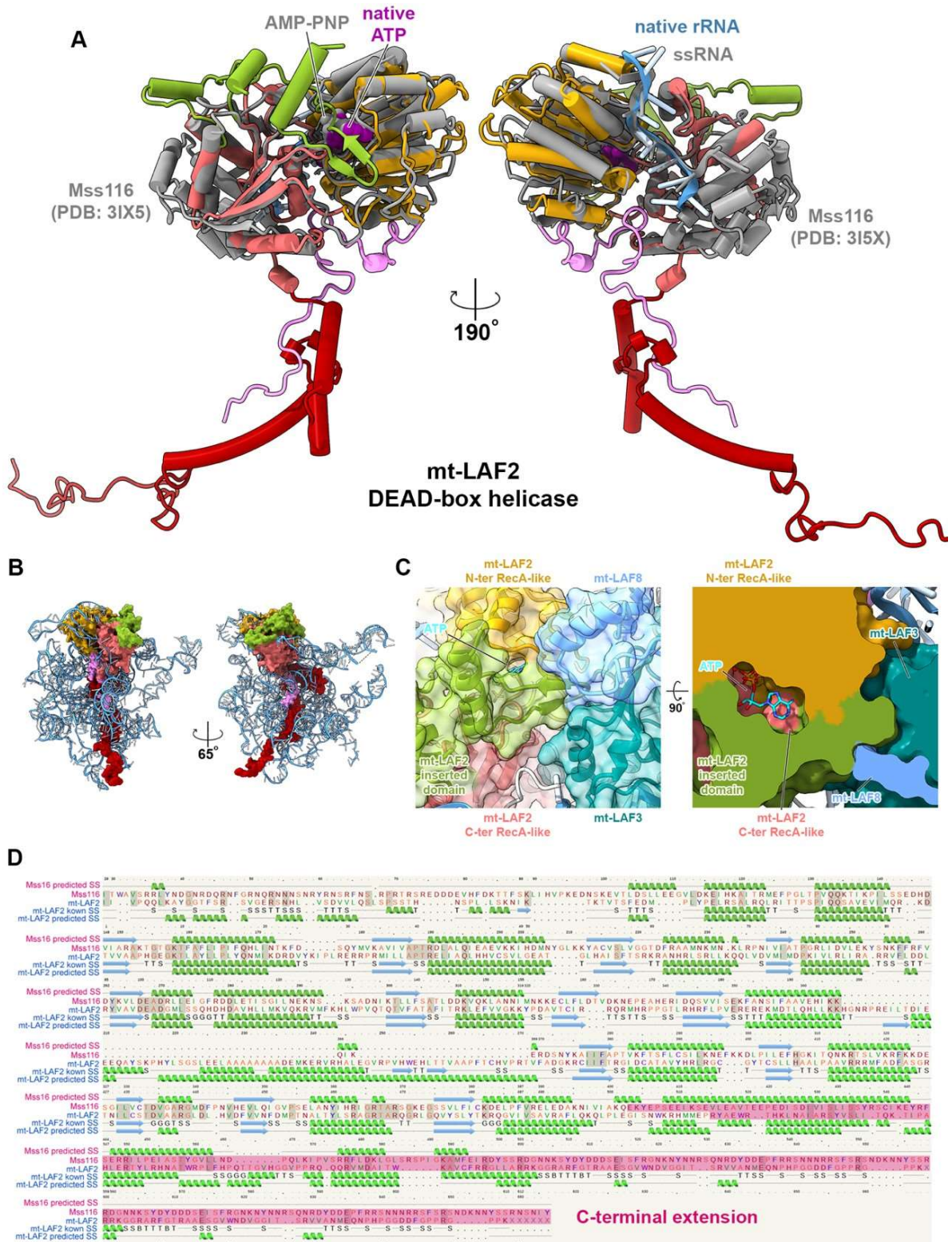


Figure S5. Detailed look at the DEAD-box helicase mt-LAF2. Related to Figure 4

(A) Two views of the structure of mt-LAF2 colored according to its domains, overlaid with the crystal structure of yeast DEAD-box helicase Mss116 (PDB: 3IX5). (B) Structure of mt-LAF2 (surface representation) with 12S rRNA (cartoon) to highlight its exceptional entanglement with the rRNA. (C) Alignment obtained by Phyre2 one-to-one modeling (Kelley et al., 2015) of Mss116 using the mt-LAF2 structure as a template. The C-terminal extensions of both Mss116 and mt-LAF2 are highlighted in red.

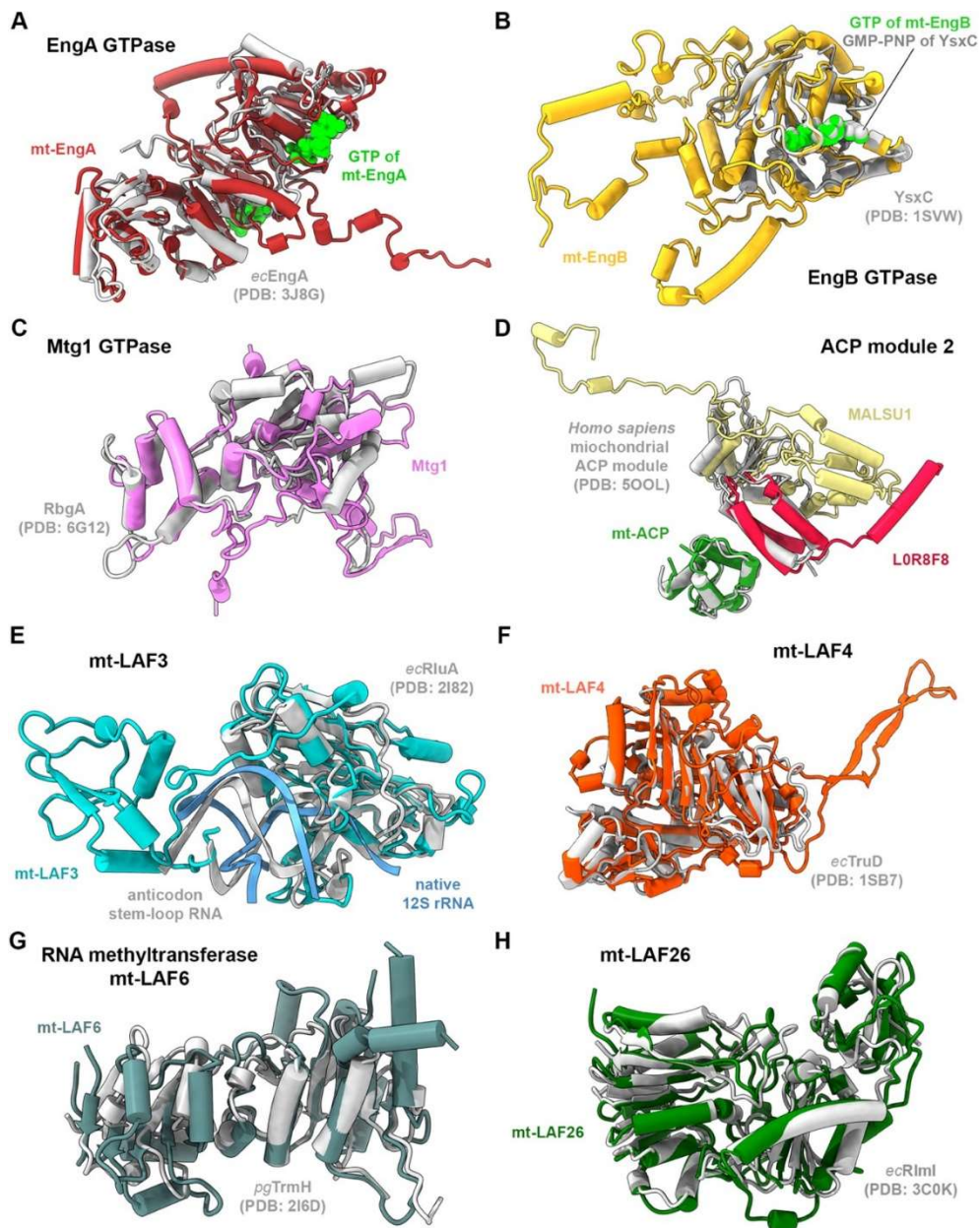


Figure S6. Selected assembly factors superimposed with structural homologs. Related to Figure 1.

Assembly factors of the trypanosomal LSU intermediates (shown in different colors) are overlaid with their structural homologs (gray). **(A)** GTPase mt-EngA overlaid with the *E. coli* EngA bound to the 50S subunit. Native GTP molecules bound to mt-EngA are shown in sphere representation and colored green. **(B)** GTPase mt-EngB superimposed with the *B. subtilis* YsxC structure. The native GTP of mt-EngB and the bound GMP-PNP of YsxC are shown in sphere representation and colored green and gray, respectively. **(C)** GTPase Mtg1 aligned with a structure of *B. subtilis* RbgA bound to the bacterial large subunit assembly intermediate. **(D)** ACP module 2 (mt-ACP, L0R8F8, MALSU1) overlaid with the ACP module present in a human mitoribosomal assembly intermediate (Brown et al., 2017). **(E)** mt-LAF3 superimposed with the structure of RluA from *E. coli*. **(F)** mt-LAF4 overlaid with the structure of *E. coli* TruD. **(G)** RNA methyltransferase mt-LAF6 aligned with the structure of TrmH from *Porphyromonas gingivalis*. **(H)** mt-LAF26 overlaid with the *E. coli* structure of RlmI.

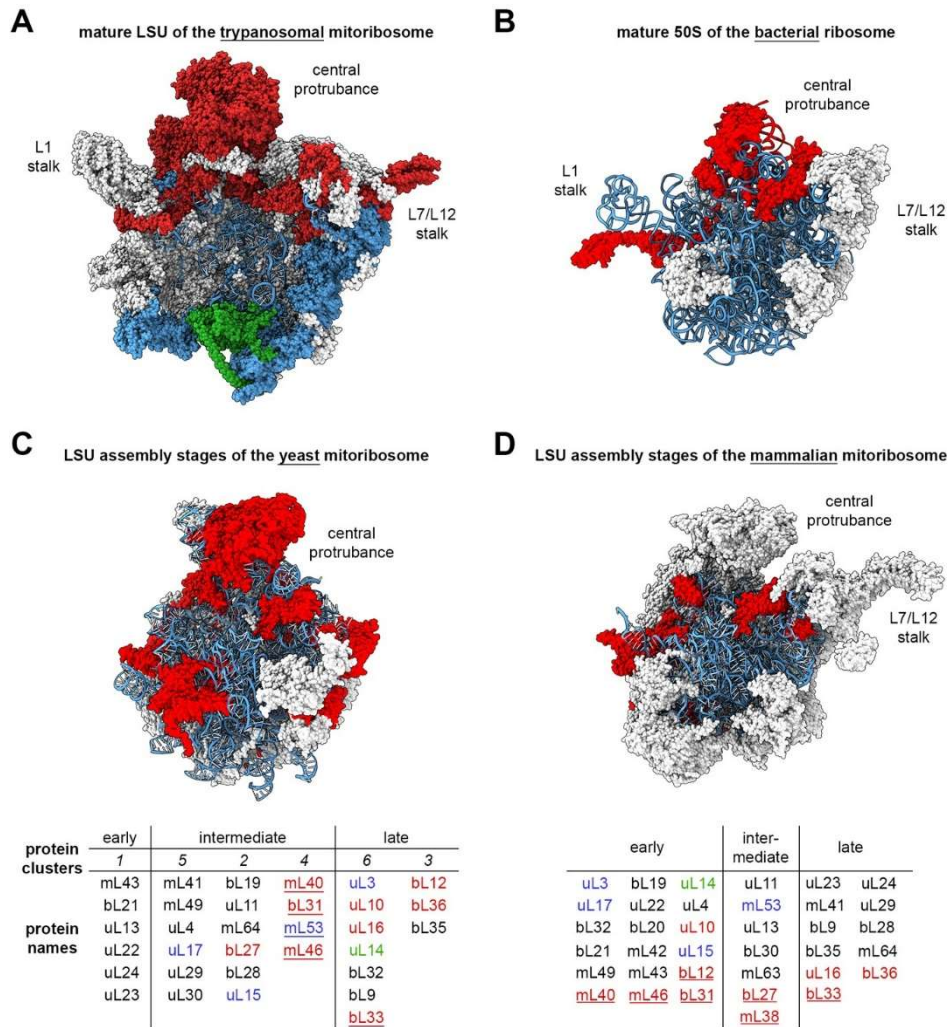


Figure S7. Comparison of the trypanosomal LSU assembly intermediates with previous biochemical data and structures of mature large subunits from different species. Related to Figure 7.

(A) Mature mitoribosomal LSU of *T. brucei* (PDB: 6HIX) shown with ribosomal proteins colored according to their appearance in the presented assembly intermediate states A and B (red: missing in both assembly states; green: missing in state A, but present in state B; blue: present in both states in an immature conformation). (B) Mature 50S LSU of *E. coli* (PDB: 4YBB). Proteins that are missing in state 3 *in vitro* assembled 50S according to Nikolay et al. (2018) are colored red. (C) Mature *S. cerevisiae* mitochondrial LSU (PDB:5MRC). Ribosomal proteins missing in p₂₅₄S according to Zeng et al. (2018) are colored red. The table below shows ribosomal proteins belonging to the same protein clusters as mentioned by Zeng et al. (2018). Their names are colored according to their appearance in the trypanosomal assembly intermediates. (D) Structure of *Sus scrofa* mitoribosomal LSU (PDB:6GB2). Ribosomal proteins missing in the intermediate assembly intermediate as shown in Bogenhaged et al. (2018) are colored red. Similar to panel C, the table below shows ribosomal protein clusters with their names colored relative to their presence in the trypanosomal assembly intermediates. In both tables, the underscored ribosomal proteins are located at the central protuberance of the given LSU. For easier comparison, all structures are shown in similar orientation.

Table S2. Oligonucleotides used in this study. Related to STAR Methods

RNAi constructs	
mt-LAF1 Tb927.7.1640	5'-CACTCAAGCTTGGATCCGAATGGTTGAGGAGGCGTT-3' 5'-GATTCTCTAGACTCGAGCAAACCCACCAGTCTGTT-3'
mt-LAF2 Tb927.11.12930	5'-CACTCAAGCTTGGATCCGCTGGAGTTTGTGTTGGGA-3' 5'-GATTCTCTAGACTCGAGCATTATCACCTTTCGCACCG-3'
mt-LAF3 Tb927.9.3350	5'-CACTCAAGCTTGGATCCGTGTCCTAGAGGAGACTGAC-3' 5'-GATTCTCTAGACTCGAGCAACAACTCAGCGATAGCC-3'
mt-LAF4 Tb927.11.5990	5'-CACTCAAGCTTGGATCCCTTGCTGAAGAAGACGGCA-3' 5'-GATTCTCTAGACTCGAGGGACTACATCCCCTTCAAC-3'
mt-LAF5 Tb927.9.12850	5'-CACTCAAGCTTGGATCCGCAACATCGTTGTTCCGGAT-3' 5'-GATTCTCTAGACTCGAGTCAAACCTCTGCTTGTGTTGC-3'
mt-LAF17 Tb927.11.16990	5'-CACTCAAGCTTGGATCCGGTGCATTAACATGACAGCC-3' 5'-GATTCTCTAGACTCGAGCCCTCTAACAAAGAGGAGTC-3'
mt-LAF21 Tb927.7.3510	5'-CACTCAAGCTTGGATCCGAGTGGCTACGTAACAGAGA-3' 5'-GATTCTCTAGACTCGAGCCGAGTGAGCCAACTTTAC-3'
mt-LAF26/KRIPP3 Tb927.1.1160	5'-CGGGATCCTTCCTGCATTGCAGCACC-3' 5'-GGCCCTCGAGACAAGGGGAGTTGGTGCC-3'
Northern oligos for mitoribosomal rRNA detection	
9S rRNA	5'-TTGGTTAAATCAGCACTTAAC-3'
12S rRNA	5'-CTTGTTAACCTGCTCGAACC-3'

Chapter 2. Stepwise maturation of the peptidyl transferase region of human mitoribosomes

The content of this chapter was previously published in Nature Communications.

Lenarčič, T.* , Jaskolowski, M.* , Leibundgut, M., Scaiola, A., Schönhut, T., Saurer, M., Lee, R.G., Rackham, O., Filipovska, A., and Ban, N. (2021). Stepwise maturation of the peptidyl transferase region of human mitoribosomes. Nature Communications. <https://doi.org/10.1038/s41467-021-23811>

Published online 16 June 2021.

Statement of contribution

Dr. Tea Lenarčič and Tanja Schönhut transfected the cells and overexpressed the protein. Dr. Tea Lenarčič isolated the mitochondria and purified the mitoribosomes. Dr. Alexandra Filipovska, Dr. Oliver Rackham and Richard G. Lee performed *in vivo* experiments in HEK cells. Dr. Tea Lenarčič and Alain Scaiola collected the cryo-EM data. Dr. Tea Lenarčič and I prepared the cryo-EM grids, processed the data and calculated the cryo-EM density maps. Cooperatively with Dr. Tea Lenarčič, we built the initial atomic models and identified the assembly factors present in the assembly intermediates. Dr. Marc Leibundgut built and performed refinement of the atomic models. Dr. Tea Lenarčič and I drafted the initial version of the manuscript. I, Dr. Tea Lenarčič and Dr. Alexandra Filipovska created the figures. I, Dr. Tea Lenarčič and Prof. Dr. Nenad Ban edited and finalized the manuscript. All authors contributed to the final version of the manuscript.

Stepwise maturation of the peptidyl transferase region of human mitoribosomes

Tea Lenarčič^{1,6}, Mateusz Jaskolowski^{1,6}, Marc Leibundgut¹, Alain Scaiola¹, Tanja Schönhut¹, Martin Saurer¹, Richard G. Lee^{2,3}, Oliver Rackham^{2,3,4,5}, Aleksandra Filipovska^{2,3,5} & Nenad Ban¹✉

¹Department of Biology, Institute of Molecular Biology and Biophysics, ETH Zurich, Zurich, Switzerland.

²Harry Perkins Institute of Medical Research, QEII Medical Centre, University of Western Australia, Nedlands, WA, Australia.

³ARC Centre of Excellence in Synthetic Biology, QEII Medical Centre, University of Western Australia, Nedlands, WA, Australia.

⁴Curtin Health Innovation Research Institute and Curtin Medical School, Curtin University, Bentley, WA, Australia.

⁵Telethon Kids Institute, Northern Entrance, Perth Children's Hospital, Nedlands, WA, Australia.

⁶These authors contributed equally: Tea Lenarčič, Mateusz Jaskolowski

✉email: ban@mol.biol.ethz.ch

Abstract

Mitochondrial ribosomes are specialized for the synthesis of membrane proteins responsible for oxidative phosphorylation. Mammalian mitoribosomes have diverged considerably from the ancestral bacterial ribosomes and feature dramatically reduced ribosomal RNAs. The structural basis of the mammalian mitochondrial ribosome assembly is currently not well understood. Here we present eight distinct assembly intermediates of the human large mitoribosomal subunit involving seven assembly factors. We discover that the NSUN4-MTERF4 dimer plays a critical role in the process by stabilizing the 16S rRNA in a conformation that exposes the functionally important regions of rRNA for modification by the MRM2 methyltransferase and quality control interactions with the conserved mitochondrial GTPase MTG2 that contacts the sarcin-ricin loop and the immature active site. The successive action of these factors leads to the formation of the peptidyl transferase active site of the mitoribosome and

the folding of the surrounding rRNA regions responsible for interactions with tRNAs and the small ribosomal subunit.

Introduction

Human mitochondrial ribosomes (mitoribosomes) are responsible for the synthesis of 13 oxidative phosphorylation (OXPHOS) proteins, encoded by the mitochondrial genome^{1,2}. Due to their unusual architectural features^{1,2,3} and the requirement to coordinate mitochondrial ribosomal RNA (rRNA) synthesis with the import of all ribosomal proteins, their assembly is anticipated to involve mitochondrial-specific pathways and participation of both conserved and mitochondrial-specific maturation factors, such as GTPases and methyltransferases¹. Production of functional mitoribosomes is critical since defects in the mitochondrial translation machinery lead to a range of severe human diseases⁴.

Structural analyses of the yeast⁵ and prokaryotic cytoplasmic large subunits^{6,7} as well as kinetoplastid mitoribosomal large subunit (mt-LSU) assembly intermediates^{8,9,10}, combined with the biochemical studies of yeast and human mitoribosomal assembly^{11,12}, showed that the solvent exposed side of the mt-LSU matures early, whereas the conserved functional sites of the large subunit, such as the peptidyl transferase center (PTC), the GTPases-associated center (GAC) and the polypeptide exit tunnel, assemble last. At the final stages of the maturation, assembly factors bind to these functional regions to facilitate their maturation and prevent premature translation¹³. Although human mitoribosome assembly has been extensively investigated using a combination of biochemical and high-throughput approaches^{12,14,15,16}, structural understanding of this process is currently limited to a late assembly intermediate where a MALSU1–L0R8F8–mt-ACP module is bound¹⁷.

To better understand the structural basis of human mitoribosome maturation, we isolated mt-LSU assembly intermediates and investigated their composition and structures using cryo-electron microscopy (cryo-EM). We determined structures of eight distinct states of the human mt-LSU where a total of seven assembly factors (MTERF4, NSUN4, MRM2, MTG2, MALSU1, L0R8F8, and mt-ACP) were bound in different combinations. Our results reveal the conformational changes that allow successive modification and maturation of the functionally important regions of rRNA. The structural data supported by biochemical evidence provide an explanation for the

role of the essential NSUN4–MTERF4 heterodimer in the process and specifically in the maturation of the functionally important tRNA-interacting P loop through interplay with the conserved GTPase MTG2 (GTPBP5). The obtained results allow us to propose a stepwise maturation pathway of the functionally important regions in the human mitochondrial large ribosomal subunit (mt-LSU).

Results

Structure of assembly intermediates of the human mitoribosomal large subunit

To purify assembly intermediates of the human mt-LSU, we transfected human embryonic kidney cells with a tagged mitochondrial GTPase 1 (MTG1) (Supplementary Fig. 1), which is a homolog of bacterial RbgA^{18,19} and is essential for the production of functional mitoribosomes due to its involvement in the late stages of mt-LSU assembly prior to monosome formation^{20,21}. The affinity-purified sample was investigated using single-particle cryo-EM to reveal several mt-LSU-like structures containing the entire set of ribosomal proteins. Furthermore, density for several additional proteins was observed at the intersubunit side bound to the rRNA in an immature conformation. Using focused classification around those additional features, we were able to obtain reconstructions of eight distinct cryo-EM classes (overall resolution range between 2.9 and 3.5 Å) corresponding to assembly intermediate states of the mt-LSU (Supplementary Figs. 2 and 3). Two of the classes, states A0

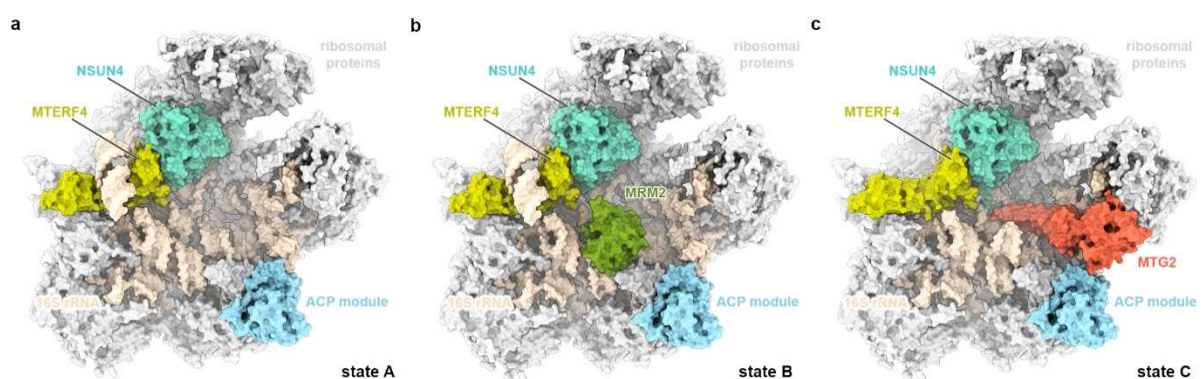


Fig. 1. Structures of the key human mitoribosomal large subunit assembly intermediates.

The molecular structures of states A (a), B (b) and C (c) are shown in surface representation from the intersubunit side. Ribosomal proteins are depicted in light grey, 16S rRNA in beige and assembly factors NSUN4, MTERF4, MRM2, MTG2 and the MALSU1–L0R8F8–mt-ACP module in teal, light green, green, red and blue, respectively.

and D, resemble the structures of the assembly intermediates described previously, where a MALSU1–L0R8F8–mt-ACP module is bound at the intersubunit face, whereas the rRNA is either disordered or in a nearly mature state, respectively¹⁷. Other classes correspond to novel assembly intermediates (Supplementary Fig. 2). We characterized in detail three of these intermediates, resolved to 2.9, 3.1, and 3.1 Å, and referred to them as states A, B, and C, respectively (Fig. 1 and Supplementary Table 1). They represent the key steps in the late stages of mt-LSU maturation, during which functionally important regions of the rRNA progressively mature. The remaining classes (states C0, D0', and D0'') correspond to structurally related, but less complete states that occur between the described intermediates.

NSUN4-MTERF4 stabilizes rRNA in a conformation that exposes the active site region

In addition to the previously characterized MALSU1–L0R8F8–mt-ACP module¹⁷, state A contains at the intersubunit side, below the central protuberance (CP), a dimer of NSUN4 and MTERF4, which were both previously identified as mitoribosomal assembly factors^{22,23} and their structures determined by x-ray crystallography^{24,25} (Fig. 1a). Although tagged MTG1 was used for affinity purification of ribosomal assembly intermediates, the factor was not sufficiently ordered on the mt-LSU to be structurally interpreted in any of the observed states. The NSUN4–MTERF4 dimer forms extensive interactions with the rRNA and ribosomal proteins by contacting rRNA helices H66, H75, H81, H87, and H93, and keeps the C-termini of uL2m and mL48 in an immature conformation (Fig. 2a). Interestingly, NSUN4 is an RNA m5C methyltransferase that has been implicated in the assembly of both small and large mitoribosomal subunits, however, biochemical data suggested that *in vivo* it only modifies the rRNA of the small subunit²³. Consistently, no RNA substrate was found in the active site of NSUN4 where a clearly visible S-adenosyl-methionine (SAM) cofactor was bound (Fig. 2b and Supplementary Fig. 4). Since NSUN4 lacks an RNA substrate recognition domain that is present in bacterial homologs²², it was proposed that it relies on interactions with MTERF4 to be targeted to the mt-LSU to regulate ribosome maturation^{22,23}, as we now observe in the mt-LSU-bound state.

The MTERF4 protein folds into a bent α -solenoid that binds with its convex region to the surface of the immature subunit and exposes its positively charged concave region towards the outside, where we observe a segment of double-helical

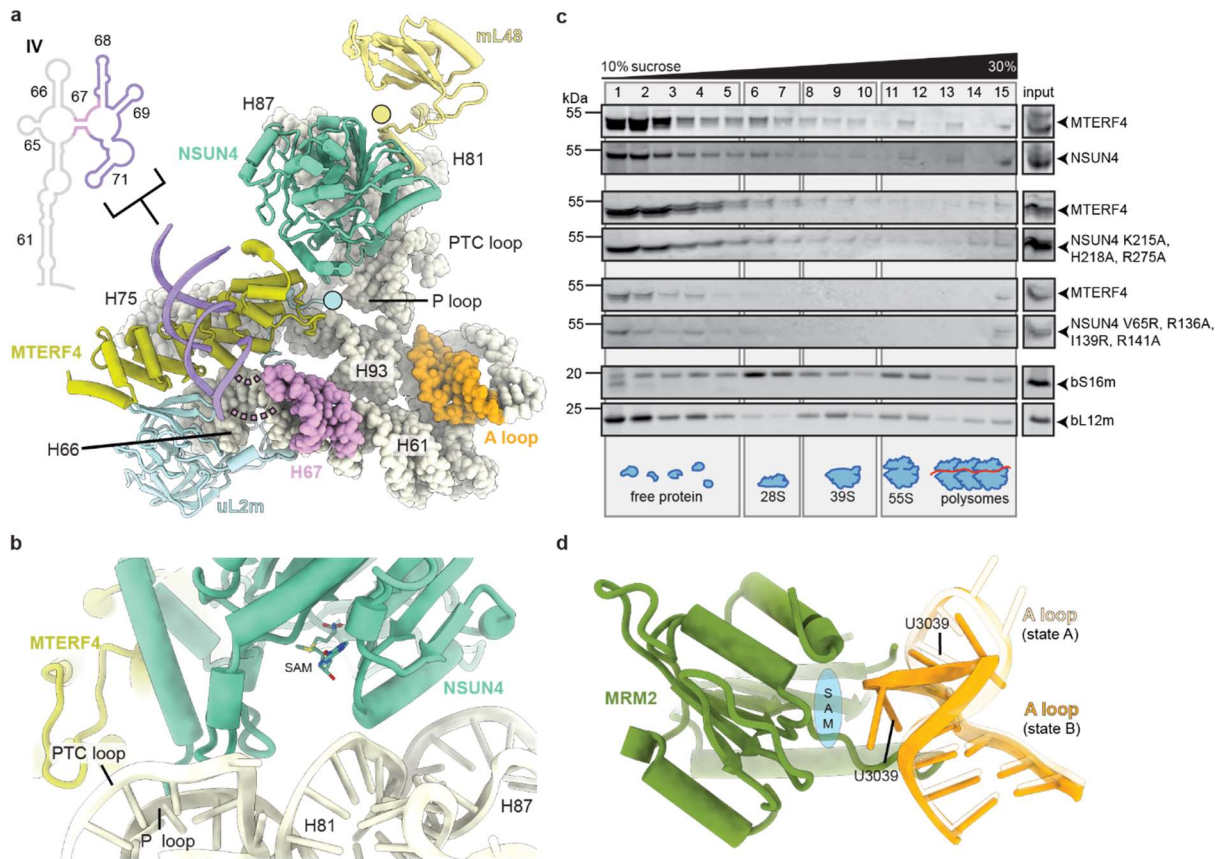


Fig. 2. Interactions of NSUN4 and MTERF4 with the immature human mitoribosomal large subunit.

(a) The NSUN4–MTERF4 heterodimer (teal and light green, respectively) forms a number of contacts with the mitochondrial large subunit via rRNA (beige spheres) and ribosomal proteins, resulting in rearrangements of the mL48 (yellow) and uL2m (light blue) C-termini (highlighted as circles), as well as stabilization of the H68–H71 region (violet) of the 16S rRNA domain IV. The connection from helix H67 (pink) to H68–H71 is shown as dashed lines. The A loop, which is modified by MRM2 in state B, is colored orange. (b) The NSUN4 (teal) active site with bound S-adenosyl-methionine (SAM) cofactor is shown together with nearby rRNA helices H81, H87, P loop and PTC loop (beige cartoon). MTERF4 is also shown for orientation (light green). (c) Effects of mutations in NSUN4 or MTERF4 on their association with mitoribosomal fractions. A continuous 10%–30% sucrose gradient was used to separate mitochondrial lysates from HEK 293T cells expressing MTERF4 and either wild-type or mutated version of NSUN4 to determine their distribution and co-migration with mitochondrial ribosomal fractions. The small and large ribosomal subunit and polysomes in mitochondria isolated from wild-type cells were followed by immunoblotting for mitochondrial ribosomal protein markers of the small (bS16m) and large (bL12m) ribosomal subunits. The input, mitochondrial lysate, was used as a positive control. (d) Rearrangement of the A loop (light orange: state A; orange: state B) upon the MRM2 methylation event. The likely position of MRM2 SAM cofactor, which is not visible in our structure, is schematically shown in blue.

RNA bound (Supplementary Fig. 5). Although we could not assign the identity of RNA nucleotides in this region, continuous density can be traced from rRNA helix H67, suggesting that the additional density belongs to the H68–H71 region of the rRNA (Fig. 2a and Supplementary Fig. 5). In the mature mt-LSU these helices form the front of the peptidyl transferase active site cleft. The interactions with MTERF4 expose the immature rRNA regions corresponding to the PTC loop that forms the active site of the ribosome, as well as the A (H92) and P (H80) loops responsible for binding the acceptor end of tRNAs and positioning substrates for the peptidyl transferase reaction in the active site of the mature mt-LSU.

To better understand the role of both MTERF4 and NSUN4 in the context of the mt-LSU assembly, we designed a series of mutants based on our structural results with deletions in key interaction regions. The mutant proteins were then investigated with respect to their ability to form dimers and associate with the mitoribosome using continuous sucrose gradients in cells expressing a FLAG-tagged MTERF4 and HA-tagged NSUN4. Wild-type MTERF4 and NSUN4 associate with each other and co-migrate with the large subunit of the mitoribosome, confirming previous findings^{22,23,24,25}. Two different mutants were designed to disrupt NSUN4 interactions with the 16S rRNA or MTERF4. The first NSUN4 mutant, bearing a triple mutation K215A, H218A and R275A located at the interface between the rRNA and NSUN4 (Supplementary Fig. 5), was designed to test the contribution of NSUN4 to binding of the complex to the 16S rRNA of the immature mt-LSU. This mutation neither reduced the association of NSUN4 with MTERF4 nor their co-migration with the large subunit (Fig. 2c), indicating that MTERF4 plays a predominant role in delivering the complex to the immature subunit. A second NSUN4 mutant carrying a quadruple mutation of residues V65R, R136A, I139R, and R141A (Supplementary Fig. 5), designed to break the dimer between NSUN4 and MTERF4, completely abolished their interaction as shown previously²⁵, and also prevented binding of either of the two proteins to the large subunit (Fig. 2c). We conclude that formation of a stable NSUN4–MTERF4 heterodimer is critical for their function in mitoribosome assembly.

MRM2 methylates the U3039 in the A loop before it adopts mature conformation

While state A described above contains only the MALSU1–L0R8F8–mt-ACP module and NSUN4–MTERF4 dimer, in state B we additionally observe the MRM2 methyltransferase bound to the rRNA in an optimal position for methylation of its target

nucleotide U3039 within the A loop of the 16S rRNA^{26,27} (Fig. 1b). The A loop is repositioned such that the 2'-O-ribose of nucleotide U3039 faces the active site of MRM2, although we do not observe density for a SAM cofactor (Fig. 2d). The binding site for the MRM2 methyltransferase, as observed in state B, is occupied by helix H71 in the mature mt-LSU (Supplementary Fig. 6). This implies a temporal order of maturation events where U3039 methylation must take place before helix H71 assumes its mature conformation.

MTG2 and NSUN4 interact with the P loop in a tweezer-like manner

In state C (Fig. 1c), MRM2 is replaced by MTG2, a GTPase conserved from bacteria to eukaryotes. The bacterial homolog (ObgE) has been recently visualized on the native assembly intermediates of the bacterial large subunit⁷. MTG2 was proposed to play a key role in the human mt-LSU assembly as a final quality control checkpoint protein²⁸. Furthermore, biochemical experiments showed that it interacts with the mt-LSU at the same time as MRM2, MTERF4, MTG1, and MALSU128. Our structure reveals that, in the presence of NSUN4, MTERF4, and the MALSU1–L0R8F8–mt-ACP module, MTG2 binds to the mt-LSU in a position, from which it can simultaneously check two key regions of the large ribosomal subunit: the GAC that plays a key role in stimulating GTP hydrolysis of translational GTPases and the catalytic PTC (Fig. 3a).

On the side of the GAC, the conserved Ras-like G domain of MTG2 interacts with sarcin-ricin loop (SRL) H95 and ribosomal protein uL11m (Fig. 3b). The G domain is oriented such that the active site, including the only partially resolved G2/Switch I and G3/Switch II loops involved in GTP binding and hydrolysis, faces towards the SRL and uL11m. Such positioning suggests that the G domain of MTG2 would be able to monitor the correct conformation of the GAC region in the final stages of mt-LSU maturation.

On the other side, the N-terminal Obg domain of MTG2 stabilizes the mature conformation of the PTC-forming helices H81, H89, H90 as well as the A and PTC loops and indirectly H71, which are in immature conformations in states A and B (Supplementary Fig. 7). The most prominent rRNA rearrangement involves the PTC loop, which in state A surprisingly forms a helix with the P loop of the 16S rRNA (Fig. 3c). As the PTC loop matures in state C, it withdraws from the P loop, which is now held in immature conformation by contacts with assembly factors MTG2 and NSUN4 (Fig. 3d). These interactions encompass the Obg domain of MTG2 and the N-terminal

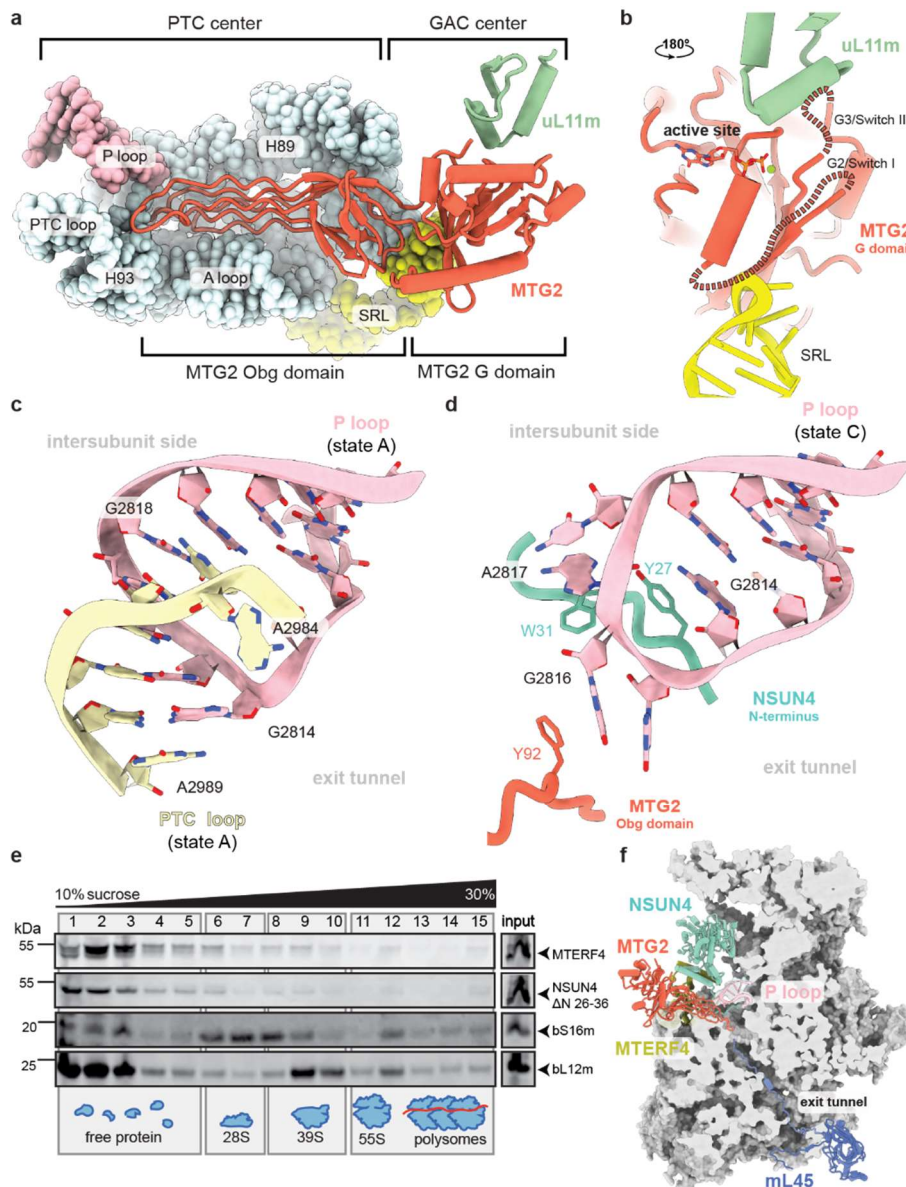


Fig. 3. Mitochondrial GTPase MTG2 interacts with the functional regions of the immature human mitoribosomal large subunit.

(a) Interaction of the MTG2 (red cartoon) with the 16S rRNA and ribosomal proteins in state C. The N-terminal Obg domain of MTG2 contacts the peptidyl transferase center (PTC) region of the 16S rRNA (light cyan, PTC helices depicted individually, P loop in pink), whereas the G domain associates with the ribosomal GTPase associated center (GAC) components uL11m (green) and the sarcin-ricin loop (SRL). (b) Detailed view of G domain interactions with the GAC rotated by 180° relative to panel (a). The Switch loops II and III are schematically indicated as dashed lines. The color key is the same as in panel (a). (c) The 16S rRNA PTC loop (light yellow) stacking with the P loop (pink) as a result of an immature rRNA arrangement in state A. (d) Specific interactions of the NSUN4 N-terminal tail (teal) and the MTG2 Obg domain (red) with the P loop (pink). Amino acid residues involved in coordinating the P loop are highlighted. (e) Effects of NSUN4 ΔN 26-36 mutant on the association with

continued on the next page

mitoribosomal fractions and 55S monosome formation. A continuous 10%–30% sucrose gradient was used to separate mitochondrial lysates from HEK 293T cells expressing the MTERF4 and NSUN4 mutant to determine their distribution and co-migration with mitochondrial ribosomal fractions. The small and large ribosomal subunit and polysomes in mitochondria isolated from NSUN4 ΔN 26-36 transfected cells were followed by immunoblotting for mitochondrial ribosomal protein markers of the small (bS16m) and large (bL12m) ribosomal subunits. The input, mitochondrial lysate, was used as a positive control. (f) Cross-section of the mitochondrial large subunit state C assembly intermediate. Spatial arrangement of assembly factors NSUN4 (teal), MTERF4 (light green) and MTG2 (red) ensure probing the P loop (pink) and the entrance to the nascent polypeptide tunnel in the mitochondrial large subunit assembly intermediate (gray). The mL45 (blue) N-terminal tail occupies the exit tunnel, contributing to an inactive state of the subunit.

tail of NSUN4, which is disordered in the absence of MTG2. The two factors grip the immature P loop from two sides in a tweezer-like manner involving aromatic residues Tyr27 and Trp31 of NSUN4 that stack with the P loop nucleotides G2814 and A2817, whereas MTG2 contributes Phe92 to interact with the P loop nucleotide G2816 (Fig. 3d). While deletion of residues 26–36 at the N-terminal region of NSUN4 did not reduce the association of NSUN4 with MTERF4 or mt-LSU, it reduced the levels of mature mitoribosomes in a dominant-negative manner (Fig. 3e) compared to the wild-type control (Fig. 2c). Taken together, our structural and biochemical results reveal a direct contribution of the NSUN4 N-terminal tail to the maturation of the mt-LSU.

The above-mentioned P loop is the sole element of the 16S rRNA domain V that remains immature in state C and, together with helices H68 and H69 of domain IV that are still bound to MTERF4, the only area in the mt-LSU rRNA that still needs to mature (Supplementary Fig. 7). Interestingly, besides keeping the P loop in a distinct immature conformation, MTG2 also samples the entrance to the nascent polypeptide tunnel with one of its Obg domain loops (Fig. 3f). At exit side of the ribosomal tunnel, we observe that mitoribosomal protein mL45 inserts its N-terminal tail into the tunnel, as observed for the non-translating mature mitoribosomes^{29,30}, and reaches almost to the Obg domain of MTG2. Consequently, the two proteins sample virtually the entire length of the exit tunnel and may play a role in facilitating proper folding of proteins and rRNA elements forming the mitoribosomal nascent polypeptide tunnel during mt-LSU maturation.

Stepwise maturation of the human mitochondrial large subunit

Visualization of eight distinct assembly intermediates of the human mt-LSU that reveal the interdependence of assembly factors and the role of the rRNA in the process allows us to propose a model for stepwise maturation of the ribosomal active site (Fig. 4 and Supplementary Fig. 8). Binding of the NSUN4–MTERF4 dimer to the immature, but compositionally complete mt-LSU, sequesters the flexibly disposed H68–H71 region to expose the active site and allow access of factors that modify the rRNA and check its conformation. This conformation is recognized by the methyltransferase MRM2 that modifies nucleotide U3039 in the A loop of the rRNA. After the methylation of U3039, MRM2 dissociates and the quality checkpoint GTPase MTG2 binds to the P loop in an NSUN4-dependent manner to facilitate maturation of the PTC and to check the functionality of the GAC of the ribosome. Once the rRNA assumes its native or nearly native conformation, the assembly factors dissociate, and a mature, translationally competent mt-LSU is formed.

Our data provide the basis for understanding the late stages of human mt-LSU maturation at a structural level and reveal the key role of the NSUN4 and MTERF4 to induce a conformation of the subunit ready for subsequent modification and maturation steps. The described assembly intermediates show maturation and/or proof-reading of all functionally important regions of the large subunit. These results complement the

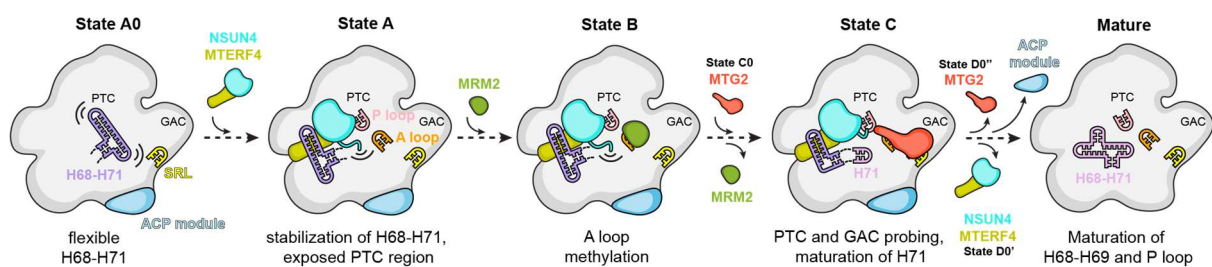


Fig. 4. Model for stepwise maturation of the human mitoribosomal large subunit aided by assembly factors.

Eight classes, corresponding to distinct assembly states in this study, allow us to propose the order of events in the late stages of the human mitoribosomal large subunit assembly. Sequestering of the H68-H71 16S rRNA by assembly factors NSUN4 and MTERF4 exposes the functionally important regions of the large subunit that allows MRM2 to modify its target nucleotide in the A loop. Dissociation of MRM2 is followed by association of MTG2, a mitochondrial GTPase that performs a final quality check of the peptidyl transferase center (PTC) region as well as the sarcin-ricin loop (SRL) in the GTPase associated center (GAC). Dissociation of all assembly factors results in completion of the rRNA maturation and formation of a translationally competent particle.

discovery of a remarkably complex mitoribosomal assembly machinery in trypanosomal mitochondria^{8,9,10,31} and suggest that the divergent mitochondrial ribosomes are likely to involve an equally diverse set of assembly factors across different species. Furthermore, while this work was in preparation, several manuscripts describing complementary results on the topic of mt-LSU maturation were published or uploaded in pre-print repositories^{32,33,34,35}. Taken together, these results now provide a comprehensive description of the late stages of mitoribosomal large subunit assembly in human mitochondria. Furthermore, these results will help us understand the structural basis of mutations in the mitochondrial translational apparatus that are associated with neurodegenerative diseases³⁶ and diverse progressive and fatal genetic disorders^{37,38}.

Methods

Transient expression of MTG1-3xFLAG in HEK 293 EBNA cells

HEK 293 EBNA embryonic kidney cells, adapted to suspension growth in serum-free Ex-Cell medium, were obtained from the protein production and structure core facility at EPFL. The cell line was cultured at 37 °C under 4.5% CO₂ in EX-CELL® 293 serum-free medium for HEK 293 cells (Sigma), supplemented with 4 mM L-glutamine. The cells were not tested for mycoplasma contamination.

The pcDNA3.1(+) plasmid encoding the C-terminally 3xFLAG-tagged MTG1 (UniProt ID Q9BT17) was ordered from GenScript. The inserted sequence was verified using a CMV forward primer at Microsynth. Cells with a concentration of 10⁶ cells/mL were transfected with 1.5 mg of DNA per liter of the culture using transfection reagent 40 kDa PEI MAX (Polysciences, Inc.) in a 1:2 ratio. Cells were harvested and mitochondria were isolated 72 h post-transfection.

Isolation of mitochondria from HEK 293 EBNA cells

Mitochondria were isolated as previously described^{39,40} with few modifications. Briefly, the cell pellets were resuspended in ice-cold RSB hypo buffer (10 mM Tris–HCl pH 7.5, 10 mM NaCl, and 1.5 mM MgCl₂) and allowed to swell for 10 min. The swollen cells were opened with several strokes of a dounce homogenizer followed by immediate addition of 2.5× MS buffer (12.5 mM Tris–HCl pH 7.5, 525 mM mannitol, 175 mM sucrose, 2.5 mM EDTA, and 2.5 mM DTT) to a final concentration of 1× MS

buffer (5 mM Tris–HCl pH 7.5, 210 mM mannitol, 70 mM sucrose, 1 mM EDTA and 1 mM DTT). The homogenate was clarified at 1300×g and 4 °C for 10 min, followed by another 10 min centrifugation at 7500×g and 4 °C. Finally, the supernatant and the crude mitochondria fraction were separated after centrifugation at 9500×g and 4 °C for 10 min. The mitochondria pellet was resuspended in 20 mM HEPES–KOH pH 7.6, 250 mM sucrose, and 1 mM EDTA and applied to a layered sucrose gradient, consisting of 15%, 23%, 32%, and 60% (w/v) sucrose solutions in 20 mM HEPES–KOH pH 7.6 and 1 mM EDTA. After 70 min ultracentrifugation at 60,000×g and 4 °C using SW 32 Ti rotor, mitochondria band between 32% and 60% (w/v) sucrose solution was carefully collected, flash-frozen in liquid nitrogen, and stored at –80 °C until use.

Preparation of MTG1-3xFLAG-tagged mitochondrial ribosomes

Upon thawing of the mitochondria, 1.5 volumes of lysis buffer (20 mM HEPES–KOH pH 7.6, 100 mM KCl, 20 mM MgCl₂, 1.6% Triton X-100, supplemented with 1× cComplete EDTA-free protease inhibitor cocktail (Roche)) was added, and mitochondria were lysed using a dounce homogenizer. Membranes were further solubilized by stirring for 15 min at 4 °C. The lysate was clarified by centrifugation at 20,800×g for 15 min at 4 °C. Next, the supernatant was incubated for 1.5–2 h at 4 °C with anti-FLAG M2 affinity gel (Sigma) while gently mixing. The anti-FLAG M2 affinity gel (Sigma) was pre-equilibrated with three sequential column volumes of 0.1 M glycine HCl pH 3.5 and washed with 10 volumes of TBS and wash buffer (20 mM HEPES–KOH pH 7.6, 100 mM KCl, and 20 mM MgCl₂). After collecting the flow-through, the beads were washed with 10 column volumes of wash buffer. Bound mitoribosomes were eluted 3 times using elution buffer (20 mM HEPES–KOH pH 7.6, 100 mM KCl, 20 mM MgCl₂, and 100–200 µg/mL 3×FLAG peptide), each time preceded by a 10–15 min incubation at 4 °C with gentle mixing. Eluted fractions were pooled and subjected to a 2.5 h ultracentrifugation at 135,500×g at 4 °C using a TLA-55 rotor (Beckman-Coulter). Finally, the mitoribosome pellet was resuspended in mitoresuspension buffer (20 mM HEPES–KOH pH 7.6, 100 mM KCl, 20 mM MgCl₂, and 1 mM DTT), yielding mt-LSU at a concentration of ~40 nM. Samples from the key steps of the purification were subjected to western blot analysis (anti-3×FLAG antibody A8592, Sigma) (Supplementary Fig. 1).

Expression of NSUN4 variants in HEK 293T cells

Expression cassettes for NSUN4 variants were synthesized from overlapping oligonucleotides and cloned into pTwist CMV (Twist Bioscience). All NSUN4 variants were expressed as fusions to a C-terminal HA tag, while MTERF4 was C-terminally FLAG-tagged.

Human embryonic kidney (HEK 293T) cells were cultured at 37 °C in humidified 95% air with 5% CO₂ in Dulbecco's modified essential medium (DMEM) (Gibco, Life Technologies) containing glucose (4.5 g/L), L-glutamine (2 mM), 1 mM sodium pyruvate, 50 µg/ml uridine, and 10% (v/v) fetal bovine serum (FBS). The cells were tested and shown to be free off mycoplasma contamination. HEK 293T cells were plated at 60% confluence in 15 cm plates and transfected with mammalian expression plasmids in OptiMEM media (Invitrogen). 158 ng/cm² of NSUN4 and MTERF4 plasmid DNA, in equal ratios, were transfected using Fugene HD (Roche). Cell incubations were carried out for 72 h following transfection and mitochondria were isolated as described previously⁴¹.

Sucrose gradients of mitochondrial ribosomes to analyze NSUN4 mutants

Sucrose gradient fractionation was carried out on purified mitochondria as previously described⁴¹. Briefly, isolated mitochondria were separated on a 10–30% sucrose gradient and lysed in 260 mM sucrose, 100 mM KCl, 20 mM MgCl₂, 10 mM Tris–HCl pH 7.5, 2% digitonin, 40 U/ml RNase inhibitor, and 1× cComplete protease inhibitor cocktail (Roche) for 20 min. After centrifugation at 9200×g for 45 min at 4 °C, the clarified lysates were loaded on a continuous 10–30% sucrose gradient containing 100 mM KCl, 20 mM MgCl₂, 10 mM Tris–HCl pH 7.5, and the aforementioned RNase and protease inhibitors, followed by centrifugation at 71,000×g in an Optima Beckman Coulter preparative ultracentrifuge. Fractions were collected, and one-third of each fraction was precipitated with 0.02% sodium deoxycholate and 12% trichloroacetic acid, washed twice with acetone, and resolved by SDS–PAGE. Representative markers of the small and large ribosomal subunits were detected by immunoblotting as described below.

Immunoblotting

Specific proteins were detected using rabbit monoclonal antibodies against MRPL12 (bL12m) (16394-1-AP), MRPS16 (bS16m) (16735-1-AP), and FLAG (Sigma, F7425); and mouse monoclonal antibodies against HA (Cell Signaling, 2367). All

primary antibodies were diluted 1:1000 using the Odyssey blocking buffer (LI-COR). IR dye 800CW goat anti-rabbit IgG or IR Dye 680LT goat anti-mouse IgG (LI-COR) secondary antibodies (diluted 1:10,000) were used, and the immunoblots were visualized using the Odyssey Infrared Imaging System (LI-COR).

Cryo-EM sample preparation and data acquisition

Quantifoil R2/2 holey carbon copper grids (Quantifoil Micro Tool) were prepared by applying an additional thin layer of continuous carbon, followed by glow-discharging for 15 s at 15 mA using an easiGlow Discharge cleaning system (PELCO). For both datasets, 4 μ l of resuspended MTG1-3 \times FLAG-tagged mitoribosome sample was directly applied onto the grid mounted in the Vitrobot chamber (Thermo Fisher Scientific) and incubated for 1 min. Excess of buffer was blotted away, and the grid was immediately plunge frozen in 1:2 ethane:propane (Carbagas) at liquid nitrogen temperature. The Vitrobot chamber was kept at 4 °C and 100% humidity during the whole procedure. For the second dataset, NP-40 detergent was added to a final concentration of 0.001% just before applying the MTG1-3 \times FLAG-tagged mitoribosome sample onto the grid.

Both datasets were collected on a Titan Krios cryo-transmission electron microscope (Thermo Fisher Scientific) operating at 300 kV. For the first dataset, the microscope was equipped with a Falcon III EC Direct Electron Detector (FEI) and the movies were collected in integrating mode with a pixel size of 1.087 Å/pix, 30 frames, and a total dose of 60 e⁻/Å², with defocus varying from -3.0 to -0.6 μ m. The second dataset was collected on a microscope equipped with a K3 detector (Gatan), mounted to a GIF Quantum LS imaging filter operated with an energy filter slit width of 20 eV. The movies were collected in counting and super-resolution mode, with 40 frames and a total dose of 60 e⁻/Å² at a physical pixel size of 1.06 Å/pix (0.53 Å/pix in super-resolution) with defocus varying from -3.0 to -0.6 μ m. The collection of both datasets was automated with the EPU software (Thermo Fisher Scientific).

Cryo-EM data processing

Both datasets were collected and processed independently. Unless stated otherwise, all processing steps were performed using cryoSPARC 3.1⁴².

Movies of the first dataset collected on the Falcon III EC Direct Electron Detector (FEI) were drift-corrected and dose-weighted using MotionCor2⁴³, and the corrected 15,441 micrographs were imported into cryoSPARC⁴³. The CTF parameters for each

micrograph were estimated using patch-based CTF estimation, and 100 randomly selected micrographs were used to pick initial particles using a Laplacian-of-Gaussian filter-based method. These particles were subjected to a 2D classification. Classes resembling the large subunit of the human mitoribosome were used as a reference for picking particles from the whole dataset. The resulting 2,214,072 particles were extracted at 5.6-fold binning and subjected to 2D classification. Good-looking classes were selected and used for an ab-initio reconstruction to create the initial 3D model. The obtained model was then used as an input in homogenous refinement with all 1,064,609 selected particles from the 2D classification. The resulting refined map was used to create a mask covering the intersubunit side of the large subunit in UCSF Chimera⁴⁴. Aligned particles, together with the mask, were used in a 3D Variability analysis⁴⁵ with eight modes to solve and the resolution filtered to 6 Å. The particles were then divided into 10 clusters using 3D variability display.

The second dataset was pre-processed during collection using cryoSPARC live⁴². The pre-processing included 2-fold binning, drift-correction, dose-weighting, CTF estimation, and particle picking using a Laplacian-of-Gaussian filter-based method, resulting in 10,682 processed micrographs and 1,626,837 extracted particles that were exported into cryoSPARC. The particles were then subjected to 2D classification, and classes resembling the mitoribosomal large subunit were selected, resulting in 833,994 particles. All particles were used for ab-initio reconstruction, and the resulting cryo-EM map was used as an input model in homogenous refinement. The previously created intersubunit mask was resampled onto the new map using UCSF Chimera⁴⁴ and together with the aligned particles was used for 3D variability analysis⁴⁵ with five modes to solve and the resolution filtered to 10 Å. The particles were then divided into 25 clusters using 3D variability display.

Overall, the processing of both datasets resulted in similarly looking 3D classes. The only difference was states B and D0", which were present only in the first and the second dataset, respectively. The key classes found in both datasets were re-extracted at full-size and refined again, this time with per-particle defocus estimation⁴⁶. The local resolution was calculated using a locally windowed FSC method as described in ref. 47.

Model building and refinement

Published structures of the mature human mitoribosome³⁰ (PDB 6ZM6) and of a late assembly intermediate containing the ACP module¹⁷ (PDB 5OOL) were used as initial models and docked into the cryo-EM maps using UCSF Chimera⁴⁴. Composite models were assembled in PyMOL Molecular Graphics System, Version 2.1.5 (Schrödinger, LLC), followed by manual rebuilding of the proteins and nucleic acids using Coot⁴⁸. For interpretation of the additional density features representing the assembly factors, the crystal structures of the human NSUN4–MTERF4 dimer²⁴ (PDB 4FZV) and MRM2 (PDB 2NYU) were fitted and readjusted. For MTG2, an initial model was obtained using the Phyre2 modeling server⁴⁹ based on a crystal structure of the *E. coli* homolog ObgE⁵⁰ (PDB 5M04). The N-terminal Obg and C-terminal G domains were docked individually and rebuilt. For fitting the GDP and SAM cofactors, superimposed high-resolution structures were used as a guide.

The models were real-space refined for five cycles using Phenix version 1.19.1⁵¹, while applying side-chain rotamer and Ramachandran restraints. The remaining discrepancies between the models and maps were detected and corrected using real space difference density maps and the geometry validation tools implemented in Coot⁴⁸. The final model geometry was validated using MolProbity⁵² (Supplementary Table 1). To evaluate the quality of the fit of the refined models to the EM maps, real-space correlation coefficients (CCmask) as well as the model versus map FSCs at the FSC = 0.5 criteria were calculated. The resulting resolutions were close to those calculated from the map half-sets at the FSC = 0.143 criteria (Supplementary Fig. 3).

Figure preparation

Molecular graphics and analyses were performed with UCSF Chimera⁴⁴ and UCSF ChimeraX⁵³, developed by the Resource for Biocomputing, Visualization, and Informatics at the University of California, San Francisco, with support from National Institutes of Health P41-GM103311 and R01-GM129325 and the Office of Cyber Infrastructure and Computational Biology, National Institute of Allergy and Infectious Diseases. Detailed views of cryo-EM map densities were created using The PyMOL Molecular Graphics System, Version 2.1.5 Schrödinger, LLC.

Reporting summary

Further information on research design is available in the Nature Research Reporting Summary linked to this article.

Data availability

The data that support this study are available from the corresponding author upon reasonable request. The atomic coordinates were deposited in the RCSB Protein Data Bank (PDB) under accession numbers 7ODR (state A), 7ODS (state B), and 7ODT (state C). The cryo-EM maps were deposited in the Electron Microscopy Data Bank (EMDB) under accession numbers EMD-12845 (state A), EMD-12846 (state B), EMD-12847 (state C), EMD-12848 (state A0), EMD-12849 (state C0), EMD-12850 (state D0'), EMD-12851 (state D0''), and EMD-12852 (state D). Source data are provided with this article.

References

1. Greber, B. J. et al. The complete structure of the 55S mammalian mitochondrial ribosome. *Science* 348, 303–308 (2015).
2. Amunts, A., Brown, A., Toots, J., Scheres, S. H. W. & Ramakrishnan, V. The structure of the human mitochondrial ribosome. *Science* 348, 95–98 (2015).
3. Bieri, P., Greber, B. J. & Ban, N. High-resolution structures of mitochondrial ribosomes and their functional implications. *Curr. Opin. Struct. Biol.* 49, 44–53 (2018).
4. Ferrari, A., Del'Olivo, S. & Barrientos, A. The diseased mitoribosome. *FEBS Lett.* <https://doi.org/10.1002/1873-3468.14024> (2020).
5. Konikkat, S. & Woolford, J. L. Principles of 60S ribosomal subunit assembly emerging from recent studies in yeast. *Biochem. J.* 474, 195–214 (2017).
6. Davis, J. H. et al. Modular assembly of the bacterial large ribosomal subunit. *Cell* 167, 1610–1622e15 (2016).
7. Nikolay, R. et al. Snapshots of native pre-50S ribosomes reveal a biogenesis factor network and evolutionary specialization. *Mol. Cell* 81, 1200–1215e9 (2021).
8. Jaskolowski, M. et al. Structural insights into the mechanism of mitoribosomal large subunit biogenesis. *Mol. Cell* 79, 629–644e4 (2020).
9. Soufari, H. et al. Structure of the mature kinetoplastids mitoribosome and insights into its large subunit biogenesis. *Proc. Natl Acad. Sci. USA* 117, 29851–29861 (2020).
10. Tobiasson, V. et al. Interconnected assembly factors regulate the biogenesis of mitoribosomal large subunit. *EMBO J.* 40, e106292 (2021).
11. Zeng, R., Smith, E. & Barrientos, A. Yeast mitoribosome large subunit assembly proceeds by hierarchical incorporation of protein clusters and modules on the inner membrane. *Cell Metab.* 27, 645–656e7 (2018).
12. Bogenhagen, D. F., Ostermeyer-Fay, A. G., Haley, J. D. & Garcia-Diaz, M. Kinetics and mechanism of mammalian mitochondrial ribosome assembly. *Cell Rep.* 22, 1935–1944 (2018).
13. Karbstein, K. Quality control mechanisms during ribosome maturation. *Trends Cell Biol.* 23, 242–250 (2013).
14. Maiti, P., Lavdovskaia, E., Barrientos, A. & Richter-Dennerlein, R. Role of GTPases in driving mitoribosome assembly. *Trends Cell Biol.* 1–14 (2021) <https://doi.org/10.1016/j.tcb.2020.12.008>.
15. Silva, D. D. et al. Mitochondrial ribosome assembly in health and disease. *Cell Cycle* 14, 2226–2250 (2015).
16. Kummer, E. & Ban, N. Mechanisms and regulation of protein synthesis in mitochondria. *Nat. Rev. Mol. Cell Biol.* 22, 307–325 (2021).
17. Brown, A. et al. Structures of the human mitochondrial ribosome in native states of assembly. *Nat. Struct. Mol. Biol.* 24, 866–869 (2017).
18. Jomaa, A. et al. Functional domains of the 50S subunit mature late in the assembly process. *Nucleic Acids Res.* 42, 3419–3435 (2014).
19. Seffouh, A. et al. Structural consequences of the interaction of RbgA with a 50S ribosomal subunit assembly intermediate. *Nucleic Acids Res.* 47, 10414–10425 (2019).

20. Kotani, T., Akabane, S., Takeyasu, K., Ueda, T. & Takeuchi, N. Human Gproteins, ObgH1 and Mtg1, associate with the large mitochondrial ribosome subunit and are involved in translation and assembly of respiratory complexes. *Nucleic Acids Res.* 41, 3713–3722 (2013).
21. Kim, H.-J. J. & Barrientos, A. MTG1 couples mitoribosome large subunit assembly with intersubunit bridge formation. *Nucleic Acids Res.* 46, 8435–8453 (2018).
22. Cámara, Y. et al. MTERF4 regulates translation by targeting the methyltransferase NSUN4 to the mammalian mitochondrial ribosome. *Cell Metab.* 13, 527–539 (2011).
23. Metodiev, M. D. et al. NSUN4 is a dual function mitochondrial protein required for both methylation of 12S rRNA and coordination of mitoribosomal assembly. *PLoS Genet.* 10, 1–11 (2014).
24. Yakubovskaya, E. et al. Structure of the essential MTERF4:NSUN4 protein complex reveals how an MTERF protein collaborates to facilitate rRNA modification. *Structure* 20, 1940–1947 (2012).
25. Spåhr, H., Habermann, B., Gustafsson, C. M., Larsson, N.-G. G. & Hallberg, B. M. Structure of the human MTERF4–NSUN4 protein complex that regulates mitochondrial ribosome biogenesis. *Proc. Natl Acad. Sci. USA* 109, 15253–15258 (2012).
26. Rorbach, J. et al. MRM2 and MRM3 are involved in biogenesis of the large subunit of the mitochondrial ribosome. *Mol. Biol. Cell* 25, 2542–2555 (2014).
27. Lee, K.-W. & Bogenhagen, D. F. Assignment of 2'-O-methyltransferases to modification sites on the mammalian mitochondrial large subunit 16 S ribosomal RNA (rRNA). *J. Biol. Chem.* 289, 24936–24942 (2014).
28. Maiti, P., Antonicka, H., Gingras, A.-C. C., Shoubridge, E. A. & Barrientos, A. Human GTPBP5 (MTG2) fuels mitoribosome large subunit maturation by facilitating 16S rRNA methylation. *Nucleic Acids Res.* 48, 7924–7943 (2020).
29. Kummer, E. et al. Unique features of mammalian mitochondrial translation initiation revealed by cryo-EM. *Nature* 560, 263–267 (2018).
30. Itoh, Y. et al. Mechanism of membrane-tethered mitochondrial protein synthesis. *Science* 371, 846–849 (2021).
31. Saurer, M. et al. Mitoribosomal small subunit biogenesis in trypanosomes involves an extensive assembly machinery. *Science* 365, 1144–1149 (2019).
32. Cipullo, M., Gesé, G. V., Khawaja, A., Hällberg, B. M. & Rorbach, J. Structural basis for late maturation steps of the human mitoribosomal large subunit. *Nat. Commun.* (2021).
33. Cheng, J., Berninghausen, O. & Beckmann, R. A distinct assembly pathway of the human 39S late pre-mitoribosome. Preprint at bioRxiv <https://doi.org/10.1101/2021.03.17.435838> (2021).
34. Hillen, H. S. et al. Structural basis of GTPase-mediated mitochondrial ribosome biogenesis and recycling. *Nat. Commun.* (2021).
35. Chandrasekaran, V. et al. Visualising formation of the ribosomal active site in mitochondria. Preprint at bioRxiv <https://doi.org/10.1101/2021.03.19.436169> (2021).
36. Sun, N., Youle, R. J. & Finkel, T. The mitochondrial basis of aging. *Mol. Cell* 61, 654–666 (2016).
37. Pearce, S., Nezich, C. L. & Spinazzola, A. Mitochondrial diseases: translation matters. *Mol. Cell. Neurosci.* 55, 1–12 (2013).
38. Boczonadi, V. & Horvath, R. Mitochondria: impaired mitochondrial translation in human disease. *Int. J. Biochem. Cell Biol.* 48, 77–84 (2014).
39. Clayton, D. A. & Shadel, G. S. Isolation of mitochondria from cells and tissues. *Cold Spring Harb. Protoc.* 2014, pdb.top074542 (2014).

40. Aibara, S., Andréll, J., Singh, V. & Amunts, A. Rapid isolation of the mitoribosome from HEK cells. *J. Vis. Exp.* <https://doi.org/10.3791/57877> (2018).
41. Lee, R. G. et al. Cardiolipin is required for membrane docking of mitochondrial ribosomes and protein synthesis. *J. Cell Sci.* 133, jcs240374 (2020).
42. Punjani, A., Rubinstein, J. L., Fleet, D. J. & Brubaker, M. A. cryoSPARC: algorithms for rapid unsupervised cryo-EM structure determination. *Nat. Methods* 14, 290–296 (2017).
43. Zheng, S. Q. et al. MotionCor2: anisotropic correction of beam-induced motion for improved cryo-electron microscopy. *Nat. Methods* 14, 331–332 (2017).
44. Pettersen, E. F. et al. UCSF Chimera—a visualization system for exploratory research and analysis. *J. Comput. Chem.* 25, 1605–1612 (2004).
45. Punjani, A. & Fleet, D. J. 3D variability analysis: resolving continuous flexibility and discrete heterogeneity from single particle cryo-EM. *J. Struct. Biol.* 213, 107702 (2021).
46. Zivanov, J., Nakane, T. & Scheres, S. H. W. Estimation of high-order aberrations and anisotropic magnification from cryo-EM data sets in RELION-3.1. *IUCrJ* 7, 253–267 (2020).
47. Cardone, G., Heymann, J. B. & Steven, A. C. One number does not fit all: mapping local variations in resolution in cryo-EM reconstructions. *J. Struct. Biol.* 184, 226–236 (2013).
48. Emsley, P., Lohkamp, B., Scott, W. G. & Cowtan, K. Features and development of Coot. *Acta Crystallogr. Sect. D* 66, 486–501 (2010).
49. Kelley, L. A., Mezulis, S., Yates, C. M., Wass, M. N. & Sternberg, M. J. E. E. The Phyre2 web portal for protein modeling, prediction and analysis. *Nat. Protoc.* 10, 845–858 (2015).
50. Gkekas, S. et al. Structural and biochemical analysis of *Escherichia coli* ObgE, a central regulator of bacterial persistence. *J. Biol. Chem.* 292, 5871–5883 (2017).
51. Afonine, P. V. et al. Real-space refinement in PHENIX for cryo-EM and crystallography. *Acta Crystallogr. Sect. D* 74, 531–544 (2018).
52. Williams, C. J. et al. MolProbity: more and better reference data for improved all-atom structure validation. *Protein Sci.* 27, 293–315 (2018).
53. Goddard, T. D. et al. UCSF ChimeraX: meeting modern challenges in visualization and analysis. *Protein Sci.* 27, 14–25 (2018).

Supplementary materials

Stepwise maturation of the peptidyl transferase region of human mitoribosomes

Tea Lenarčič^{1,6}, Mateusz Jaskolowski^{1,6}, Marc Leibundgut¹, Alain Scaiola¹, Tanja Schönhut¹, Martin Saurer¹, Richard G. Lee^{2,3}, Oliver Rackham^{2,3,4,5}, Aleksandra Filipovska^{2,3,5} & Nenad Ban¹✉

¹Department of Biology, Institute of Molecular Biology and Biophysics, ETH Zurich, Zurich, Switzerland.

²Harry Perkins Institute of Medical Research, QEII Medical Centre, University of Western Australia, Nedlands, WA, Australia.

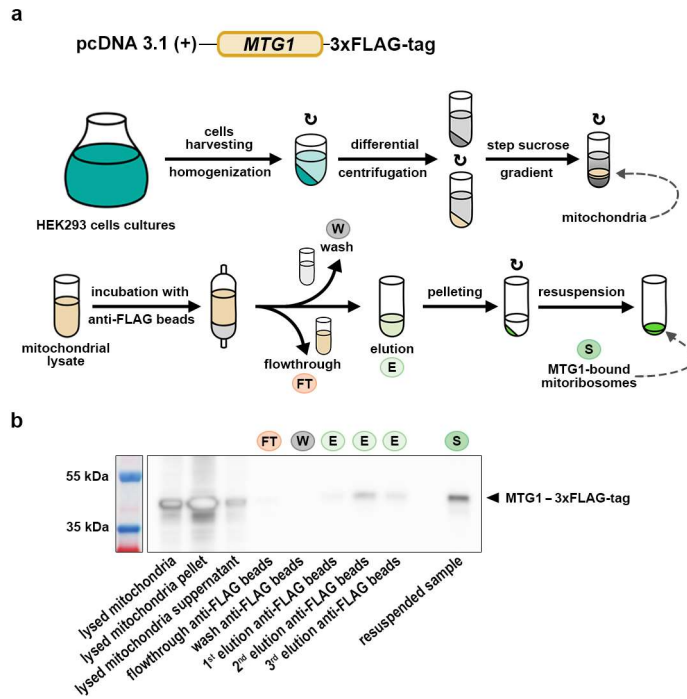
³ARC Centre of Excellence in Synthetic Biology, QEII Medical Centre, University of Western Australia, Nedlands, WA, Australia.

⁴Curtin Health Innovation Research Institute and Curtin Medical School, Curtin University, Bentley, WA, Australia.

⁵Telethon Kids Institute, Northern Entrance, Perth Children's Hospital, Nedlands, WA, Australia.

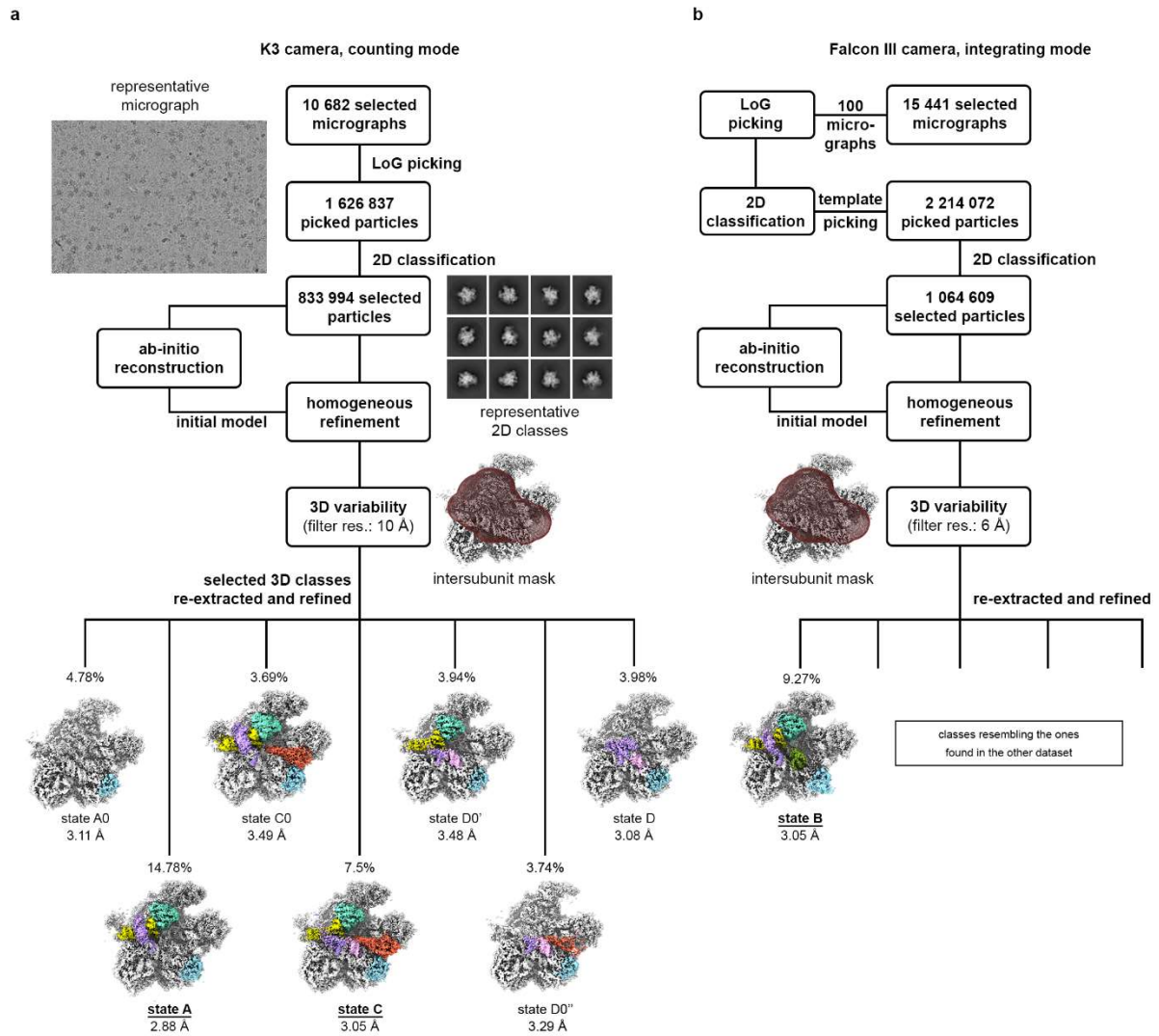
⁶These authors contributed equally: Tea Lenarčič, Mateusz Jaskolowski

✉email: ban@mol.biol.ethz.ch



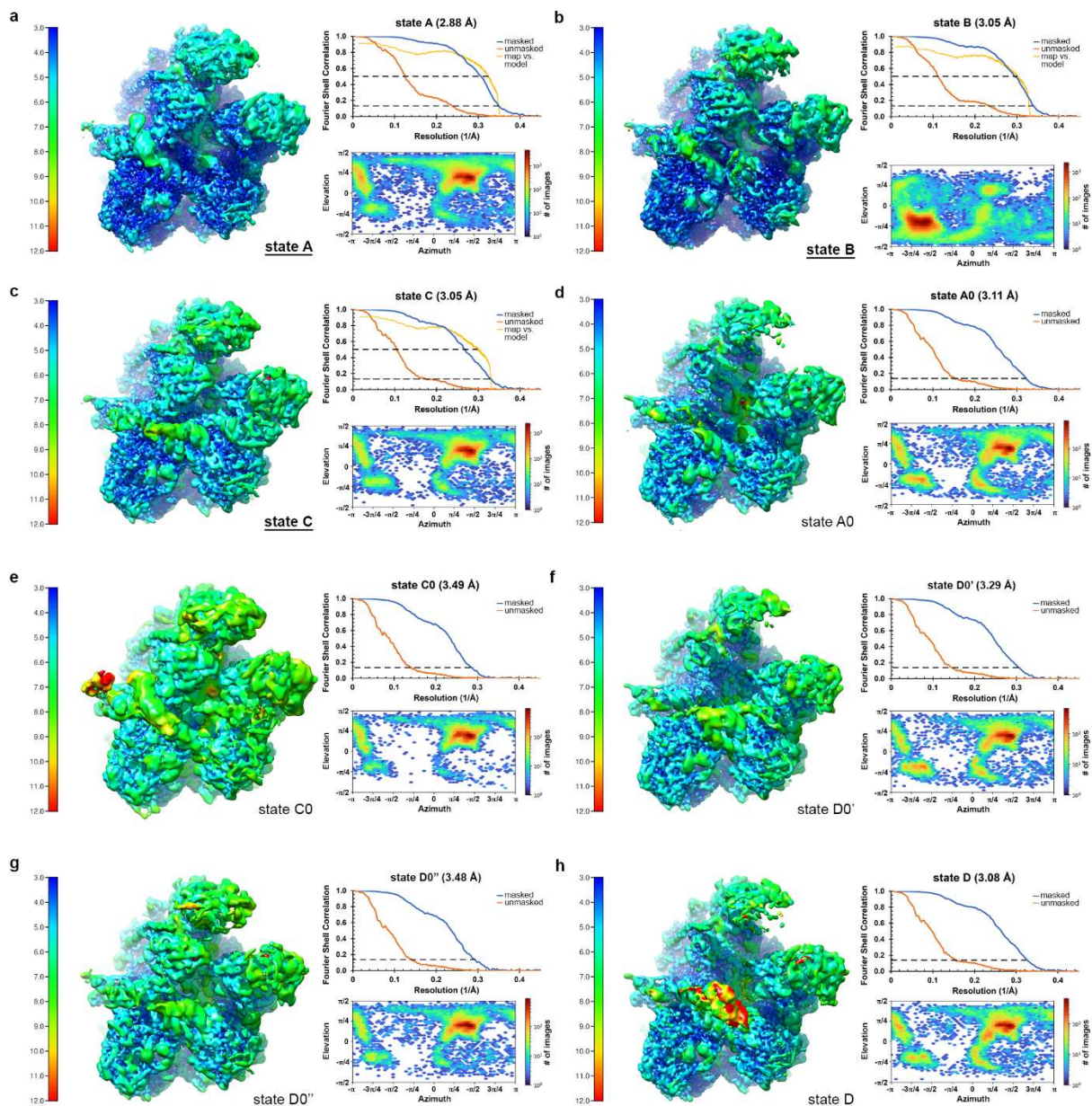
Supplementary Figure 1. 3x-FLAG tagged MTG1 co-pellets with the mitoribosomal particles.

(a) Schematic representation of the mitochondria preparation, followed by the purification of mitoribosomes *via* C-terminally 3x-FLAG-tagged MTG1. Curved arrows indicate an (ultra)centrifugation step. **(b)** Western Blot analysis of the purification procedure using antibodies against the 3xFLAG tag.



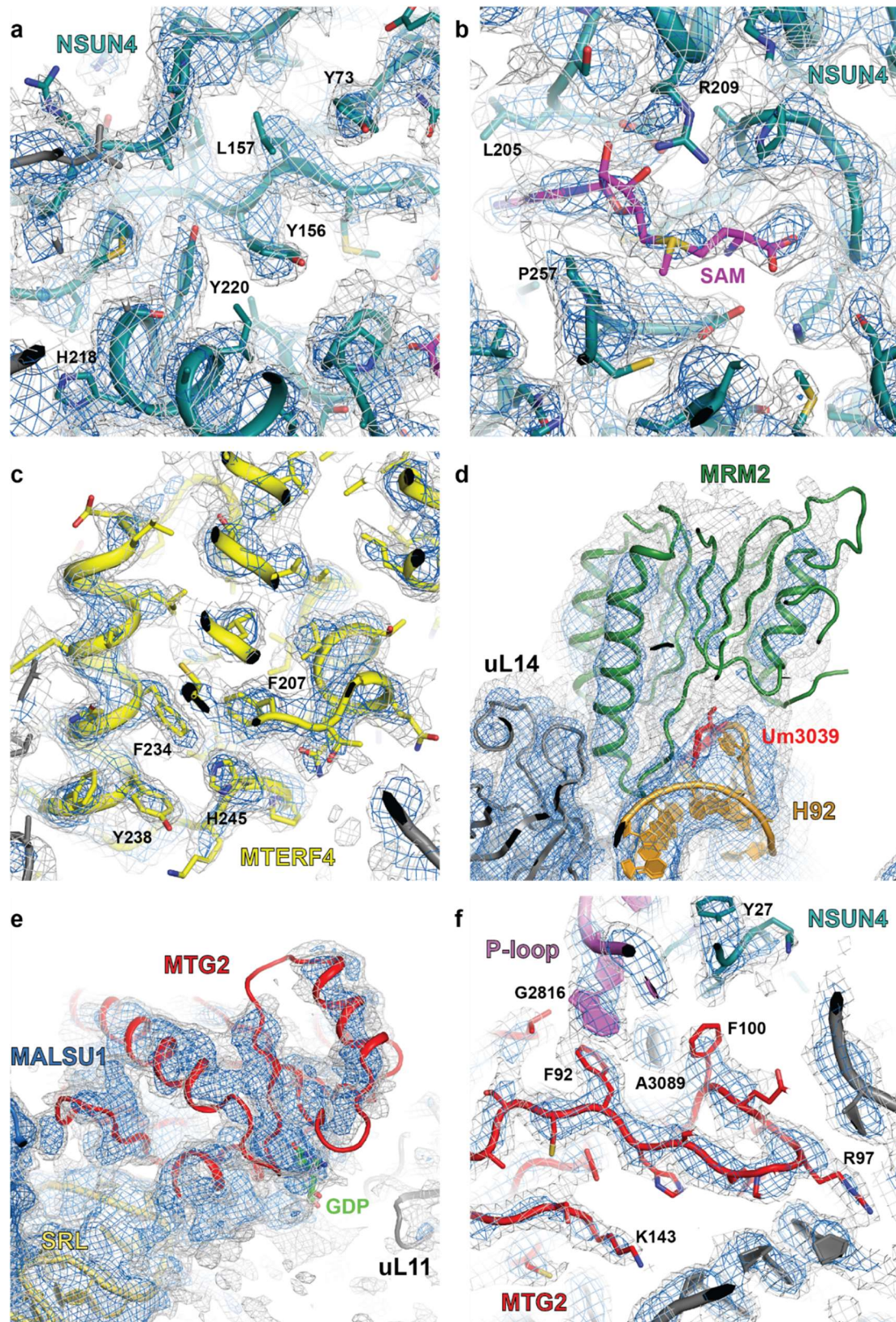
Supplementary Figure 2. Data processing of the purified particles bound to the tagged MTG1 assembly factor.

Data processing schemes for both datasets collected from the particles obtained by affinity purification of C-terminally tagged MTG1 assembly factor. Both datasets, collected using K3 (**a**) and Falcon III EC (**b**) cameras, were processed independently. Cryo-EM maps of selected 3D classes with density of assembly factors as well as key rRNA regions color-coded as in Fig. 1 are shown.



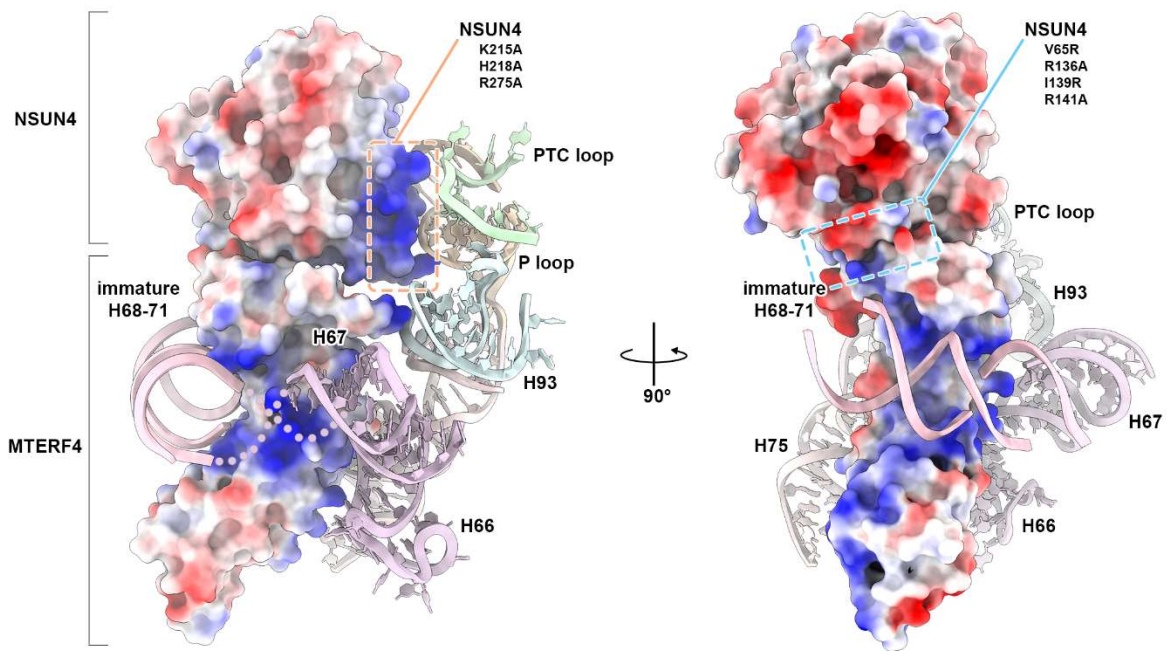
Supplementary Figure 3. Cryo-EM data statistics.

Cryo-EM maps, colored according to the local resolution with scale bars presented on the left of each panel, are shown for state A (a), state B (b), state C (c), state A0 (d), state C0 (e), state D0' (f), state D0'' (g) and state D (h). Each panel contains the FSC curve on the top right and the particles angular distribution graph on the bottom right.



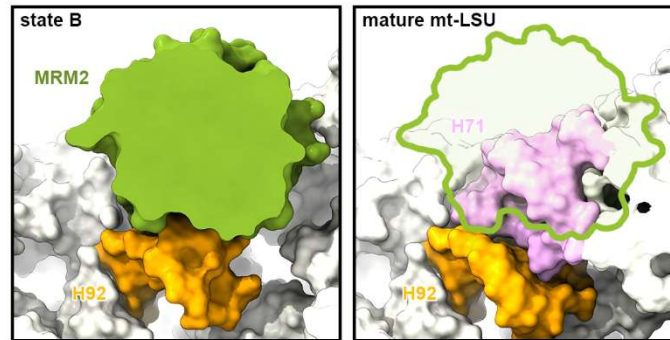
Supplementary Figure 4. Examples of electron density maps in the areas of the bound maturation factors.

Overview of the EM density for (a) NSUN4, (b) the NSUN4 S-adenosyl-methionine cofactor, (c) MTERF4, (d) MRM2, (e) the G domain of MTG2 and (f) the N-terminal Obg domain of MTG2 and NSUN4 interacting with the P loop.



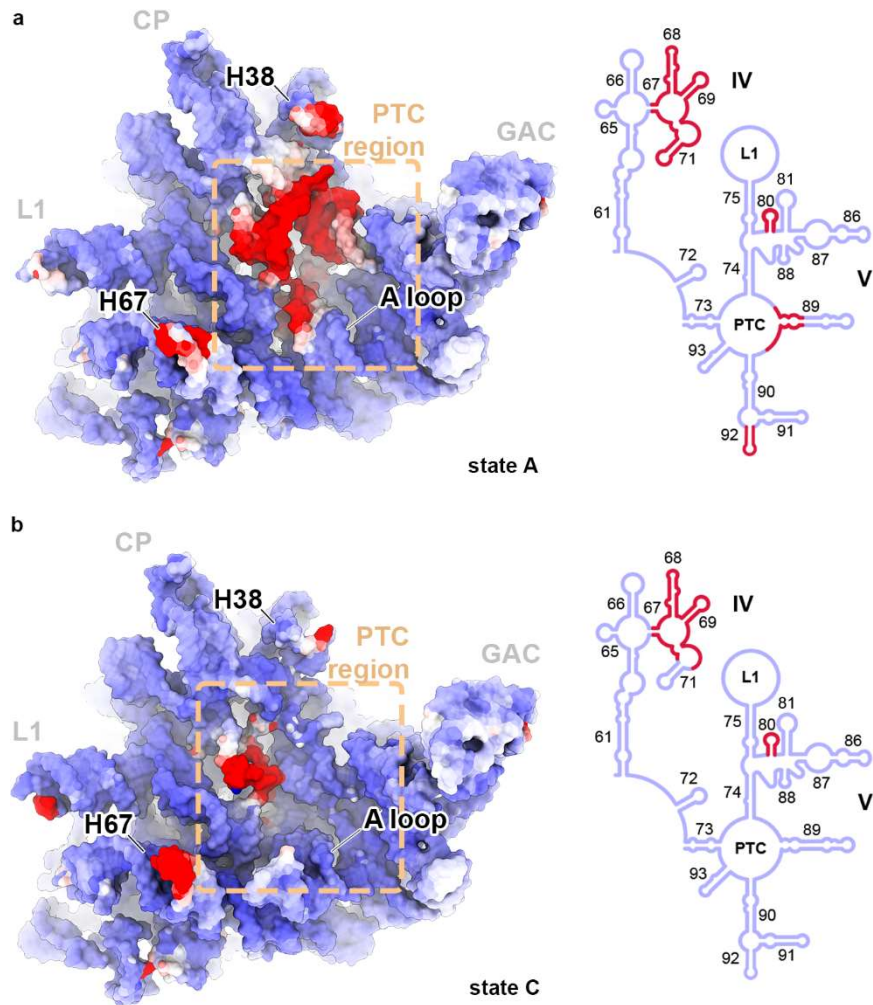
Supplementary Figure 5. NSUN4 binding to key elements of the PTC rRNA region and MTERF4 stabilizing a distinct immature conformation of H68-71.

Atomic models of NSUN4–MTERF4 are shown in surface representation and colored according to their electrostatic potential. Selected rRNA elements that interact with NSUN4–MTERF4 are shown in cartoon and are labeled individually. NSUN4–MTERF4 is shown as viewed from the GTPase associated center (left) and from intersubunit space (right). Regions of introduced NSUN4 mutations are indicated with dashed line boxes.



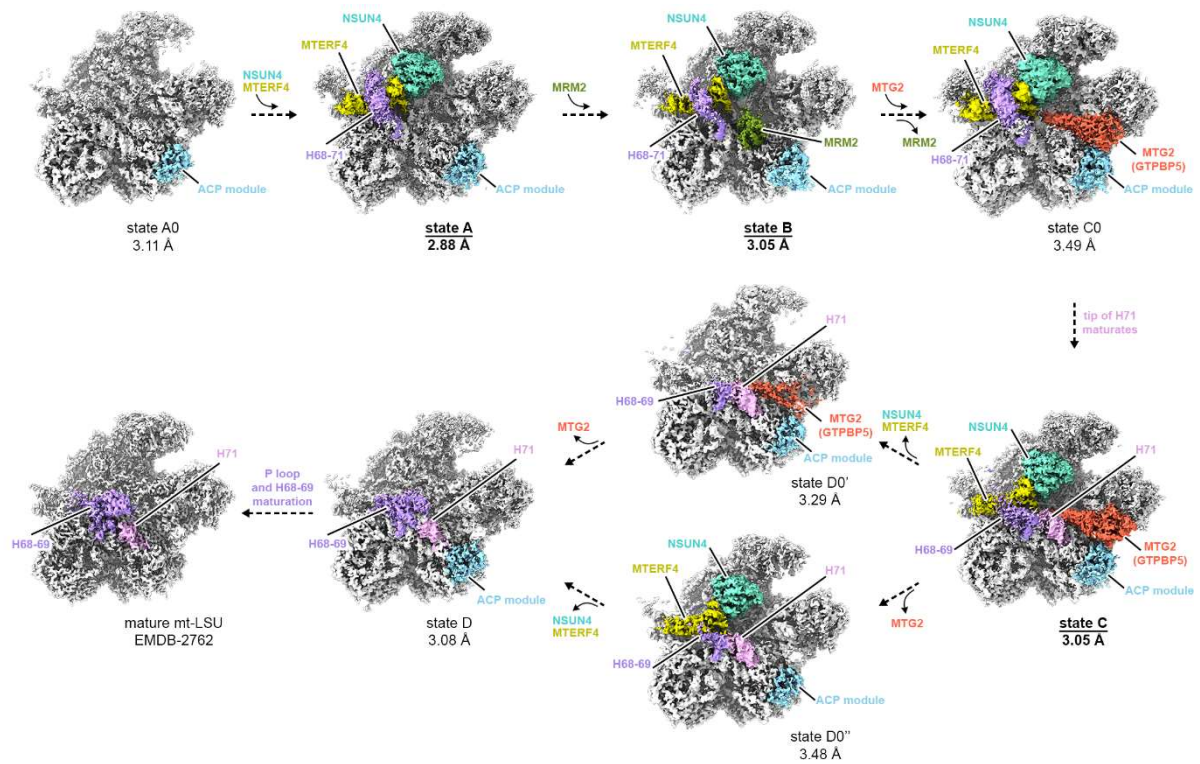
Supplementary Figure 6. MRM2 methylates U3039 in the A-loop before maturation of H71.

Cross-sections of the atomic models of state B (left) and the mature mt-LSU (right, PDB: 6ZM6) are shown as viewed from the CP. The MRM2 methyltransferase, H92 (A loop) and H71 are labeled and colored individually. On the right panel, the green outline represents superposed MRM2 to visualize steric hindrance of the assembly factor with the mature H71.



Supplementary Figure 7. Stepwise maturation of the key rRNA regions of the mt-LSU.

The 16S rRNA atomic models of states A (a) and C (b) are shown in surface representation and colored according to the root-mean-square deviation (RMSD) compared to the mature 16S rRNA (PDB: 6ZM6). RMSD values range from 0 Å (blue) to 8 Å and above (red). Corresponding 2D diagrams of 16S rRNA domains IV and V are shown on the right of each panel and colored according to their respective atomic model.



Supplementary Figure 8. Stepwise maturation of the mt-LSU including all obtained cryo-EM maps.

The pathway of mt-LSU maturation is proposed based on all obtained cryo-EM maps. The densities corresponding to the assembly factors and important rRNA fragments are colored and labeled individually. The ACP module includes MALSU1, L0R8F8 and mt-ACP.

Supplementary Table 1. Cryo-EM data collection, refinement and validation statistics.

	State A MTERF-NSUN4 + ACP module	State B MTERF-NSUN4- MRM2 + ACP module	State C MTERF-NSUN4- MTG2-H71 + ACP module
EMDB code	#####	#####	#####
PDB code	#####	#####	#####
Data collection and processing			
Camera	K3	Falcon III EC	K3
Magnification	81,000 (nominal)	75,000 (nominal)	81,000 (nominal)
Voltage (kV)	300		
Electron exposure (e ⁻ /Å ²)	60		
Defocus range (µm)	0.6-3.0		
Pixel size (Å)	1.06 (super-res. pix. at 0.53Å/pix.)	1.087	1.06 (super-res. pix. at 0.53Å/pix.)
Initial particle images (no.)	833,994	1,064,609	833,994
Final particle images (no.)	123,285	114,557	62,565
Map resolution at FSC=0.143 (Å)	2.9	3.1	3.1
Structure refinement in PHENIX 1.19.1			
Model resolution at FSC=0.5 (Å)	3.1	3.3	3.4
CC _{mask}	0.80	0.76	0.79
Map sharpening B factor (Å ²)	- 64.1	- 97.9	- 54.6
Model composition			
Non-hydrogen atoms	107,683	108,570	110,405
Protein residues	9,274	9,374	9,588
RNA residues	1,516	1,516	1,521
Ligands: Mg ²⁺ / K ⁺ / Zn ²⁺ / [Fe ₂ -S ₂] / C10-PPT / SAM / GDP	97 / 2 / 2 / 1 / 1 / 1 / -	68 / 0 / 2 / 1 / 1 / 1 / -	99 / 4 / 2 / 1 / 1 / 1 / 1
B factors min/max/mean (Å²)			
Protein	14/122/57	20/246/91	27/356/101
RNA	8/183/52	22/382/77	27/278/72
Ligand	12/108/52	19/177/88	26/234/94
R.m.s. deviations			
Bond lengths (Å)	0.002	0.002	0.002
Bond angles (°)	0.408	0.402	0.403
Validation			
MolProbity score	1.3	1.3	1.3
Clashscore	5.1	5.3	5.3
Poor rotamers (%)	0.8	0.7	0.8
Protein			
EM Ringer score	3.2	2.5	2.8
Ramachandran plot			
Favored (%)	98.73	98.70	98.78
Allowed (%)	1.27	1.29	1.22
Disallowed (%)	0.0	0.01	0.0
RNA			
Pucker outliers (%)	0.5	0.7	0.6
Bond outliers (%)	0.0	0.0	0.0
Angle outliers (%)	0.0	0.0	0.0
Suite outliers (%)	17.1	18.4	18.5

Conclusions and future perspectives

Ribosomes are responsible for protein synthesis and therefore have a central role in the expression of genetic information. A great progress has been made since the discovery of ribosomes in unveiling their composition and their mechanism of action. Ribosomal assembly has also been studied extensively in the recent years. Because of their composition and the number of proteins and rRNAs involved in its biogenesis is a complex and fascinating process that still holds many mysteries.

In addition, understanding of ribosome maturation is important from a biomedical perspective. In bacteria, the ribosome assembly may provide promising antimicrobial drug targets, while in eukaryotes a way to treat ribosome biogenesis associated disorders. In eukaryotes, ribosomopathies are caused not only by the cytoplasmic ribosome, but also the mitoribosome. Deregulation of mitoribosome components and its assembly factors also lead to severe multisystemic diseases and may cause cancer^{66,272,276-280}.

Despite the years of research and numerous excellent biochemical and genetic studies on the mitoribosome maturation, structural data is still scarce. In this thesis I presented my contributions to determining high-resolution structures of the mitochondrial large subunit from both *Homo sapiens* and human parasite *Trypanosoma brucei* that provide important structural insights into this intricate process. I have been able to identify numerous novel mitochondrial assembly factors that help in understanding their role in mitoribosome maturation. These results agree with previous biochemical and genetic studies and present promising targets for further analysis.

Mitoribosome maturation is both similar to and different from the bacterial ribosome assembly

According to the endosymbiotic theory mitochondria are organelles of α -proteobacterial origin³², and thus, the mitoribosome shares an ancestor with its bacterial counterpart. Although their structures differ significantly, only a handful of newly identified assembly factors show homology to prokaryotic proteins and seem to play similar roles in the mitoribosome maturation.

For example, three GTPases (mt-EngA, mt-EngB and Mtg1) found on one of the *T. brucei* mitoribosomal large subunit assembly intermediates show homology to

bacterial assembly factors. Interestingly, while the binding site of bacterial mt-EngB homolog has not been visualized so far, the position of both mt-EngA and Mtg1 in *T. brucei* mitoribosome is almost identical to that observed for its homologs in bacterial ribosome^{171,189}. Furthermore, biochemical investigation of the bacterial ribosome biogenesis suggest that all three GTPases act together at a specific step in the large subunit ribosomal assembly¹⁸⁵. Given the homology of the factors and almost identical binding place for those that are structurally characterized, it is tempting to assume that the role and the mode of interaction for these GTPases during bacterial ribosome assembly is very similar to those observed in the presented structures of *Trypanosoma brucei* mitoribosome.

Similarly, mitochondrial assembly factor Mtg2 found on the assembly intermediates of the human mitoribosome presented in chapter 2 shows homology to the bacterial GTPase ObgE. Interestingly, structure of ObgE in complex with the mature bacterial large subunit¹⁷⁹ shows practically identical mode of interaction. Furthermore, based on the recent structural analysis of the native assembly intermediates in bacteria that describe the role of ObgE during large subunit assembly in detail²⁸³, it seems that Mtg2 fulfills the same role in the mitoribosomal maturation as its homolog in bacteria. Additionally, the bacterial assembly intermediate described in the above-mentioned study discovered RsfS assembly factor bound just below the ObgE. Intriguingly, the structure of the human mitoribosome assembly intermediate described in chapter 2 also has a RsfS homolog bound – MALSU1. The mode of interaction of both factors is presumably the same.

Very recent results describing assembly intermediates of the human mitoribosomal large subunit characterized the binding place of DEAD-box ATPase DDX28²⁸⁴. Interestingly, DDX28 binds the assembly intermediate in virtually the same place as mt-LAF2 does the assembly intermediate of *T. brucei* mitoribosome. mt-LAF2 is also a DEAD-box helicase and based on the sequence similarity and biochemical results may act similarly to yeast Mss116, although structural analysis is necessary to validate this hypothesis. Nevertheless, a possibility that all three organisms share almost identical mitoribosomal assembly factor that fulfils the same function, despite the significant differences in the mitoribosomes structure, is definitely intriguing. Did the assembly factor evolved independently in these organisms to serve the same role? Or, and probably more likely, is the factor conserved from prokaryotes?

Despite the progress in our understanding of the bacterial ribosome maturation in recent years, we still cannot answer that and many other questions. Biochemical results indicate that several DEAD-box ATPases are involved in the maturation of the bacterial large subunit, but thus far none of them have been visualized interacting with an assembly intermediate. In general, our current structural data describe only late stages of both bacterial and mitoribosomal large subunit maturation. Our understating of the small subunit assembly is similarly limited. Although better understood biochemically in bacteria, high-resolution structural information for the early stages of small subunit maturation is still lacking. The only structural information available to date for the mitoribosomal small subunit comes from a handful of native assembly intermediates found in *T. brucei*²⁸⁵. Structures of early assembly intermediates from both bacteria and mitochondria would be of great interest and most likely several research groups are already undertaking efforts to visualize them.

On the other hand, multiple assembly factors identified in the presented structures do not show any homology to known prokaryotic proteins and seem to be specific to mitoribosomes.

Cryo-EM revolutionized the field of structural biology

Task of solving structures of early assembly intermediates was definitely made possible thanks to the advancement in cryo-EM over the past years. The advances in cryo-EM technology and methodology lead to a “resolution revolution”²⁸⁶ and had a great effect on structural biology opening up possibilities to elucidate structures of unknown and heterogenous protein complexes at high-resolution without the need for crystallization. Just like the X-ray crystallography gave rise to the field of structural biology, cryo-EM allowed it to mature and broaden the spectrum of targets that can be structurally analyzed. With almost 8000 atomic models solved by cryo-EM today, and only 21 at the beginning of 21th century, the exponential growth is stunning (based on Protein Data Bank statistics from 5th of June 2021).

But the impressive number of structures solved over the recent years is not the only wonderful benefit of cryo-EM. The resolution revolution, especially the data processing algorithms advancement, allowed for structural analysis of heterogenous, flexible and/or unknown protein complexes. Contrary to the X-ray crystallography, cryo-EM does not require protein crystallization, and consequently, proteins with flexible extensions and/or domain can be easily analyzed with cryo-EM. In the worst-

case scenario, if a given domain does not have a limited number of conformations, i.e. is continuously flexible, it will not be visible in a 3D reconstruction but it will still be possible to determine the structure for other parts of the molecule. However, in a crystallographic experiment such domain would hinder crystallization making it impossible to obtain any structural information. Even more significant advantage of cryo-EM is the ability to analyze heterogenous samples, even with unknown proteins being part of the complex.

Few proof-of-concept studies already showed that structural analyses of very heterogenous sample or even minimally purified cell lysate is possible^{287–289}. With further advancement in data acquisition speed as well as data processing capabilities, a whole cell lysate analysis followed by a “computational purification” by means of 2D and 3D classifications is becoming a possibility.

Cryo-EM has potential to position structural biology at the frontline of molecular biology

The ability to analyze and structurally characterize a minimally purified or unprocessed cell lysate is still rather an ambitious goal than reality, however, it is already feasible to investigate highly heterogeneous and completely or partially unknown protein complexes using cryo-EM. Combined with the ability to obtain high-resolution reconstructions, it is possible to build proteins models *de novo* and identify them directly from the experimental cryo-EM map^{42,285,290,291}.

Based on the structural analysis of the assembly intermediates of the mitoribosomal large subunit of *T. brucei* we were able to identify 28 assembly factors, many of which were not even suspected to take part in mitoribosome maturation. Selected factors have been further validated using RNA-mediated interference (RNAi) which confirmed their importance for large subunit assembly and *T. brucei* growth rate. In a way, our structural results paved a way for additional biochemical and genetical characterization and further experiments.

Structures of the human mitoribosomal large subunit assembly intermediate revealed a network of assembly factors occupying the immature regions of the large subunit. Reconstructions of multiple steps of assembly allowed us to propose a model for stepwise maturation of the peptidyl transferase region and to determine the structure of a previously unknown N-terminal domain of NSUN4 assembly factor. This, in turn, lead to a design of specific mutations and subsequent biochemical analysis

that allowed characterization of a specific role of NSUN4 in the human mitoribosomal large subunit assembly.

Mentioned examples illustrate the significance of high-resolution structures and their role in new discoveries. The fact that protein complexes do not need to be crystallized anymore, and therefore can be more heterogeneous, increases the chances of observing something unforeseen and unknown that generates new hypotheses and opens opportunities for further genetical and biochemical studies.

There are still aspects of cryo-EM that can be improved

Progress made in the cryo-EM in the past 5-6 years is astonishing. Improvements in data acquisition and data processing, introduction of direct detectors and general microscope availability made it the key method for structural studies. It is exhilarating to think where cryo-EM can be in the next 5-10 years.

An aspect of cryo-EM that has a high potential of improving in the near future is grid preparation²⁹². Currently, the commonly used method requires a small droplet of a sample placed on a copper grid followed by removal of the excess buffer with filter paper and subsequent rapid flash-freezing in the liquid ethane. Even though successfully used in many studies, the above-described blot method is rather wasteful and sub-optimal for selected fragile protein complexes. Nowadays, only a small portion of the grid is used for data acquisition and therefore there is no need to deposit the sample throughout the entire grid. Indeed, an alternative method is being developed where only a thin line of a sample is layered onto the copper grid^{293,294}. Such method would allow for not only a significantly smaller amounts of sample to be used, but also for multiple samples to be deposited on the same grid, enabling data collection from different samples without a need to exchange grids and effectively saving time during data acquisition.

Despite the fact that cryo-EM broadened the range of protein complexes that can be structurally studied, there are still some that are either too fragile to be investigated by this method or too transient to be successfully purified. Cryo-EM approach requires the sample to be immobilized in thin layer (<100 nm) of vitrified ice and despite the automatization and exceptionally short time necessary for grid preparation, the proteins are during this process unavoidably exposed to the air-water interface multiple times²⁹⁵. Such exposure often causes protein denaturation and protein complex dissociation, effectively limiting or completely preventing any high-

resolution structural characterization of fragile protein targets. Over the years, various methods have been developed to overcome that problem, however, many of them seem to be sample specific and often need to be tested thoroughly in a manner, ironically similar to the crystallization screens employed in X-ray crystallography.

Subtomogram averaging cryo-ET allows for structural investigation of protein complexes without the need for purification

While cryo-EM is used to analyze single particles, cryo-electron tomography (cryo-ET) visualizes a flash frozen thin cross-section of cell, tissue or whole organism²⁹⁶. As such, it allows for investigation of protein complexes in their native environment. Moreover, lack of necessity to purify the complex of interest permits analysis of transient or difficult to isolate targets. Furthermore, the ability of cryo-ET to look at protein complexes in their native environment has a potential to provide information about binding partners and their mode of interaction.

Of course, a single tomographic map is insufficient for detailed structural interpretation. However, subtomogram averaging allows for individual protein complexes to be picked, extracted, aligned and averaged, leading to a 3D reconstruction²⁹⁷. Nowadays, majority of subtomogram averaging reconstructions result in maps resolved to 30-50 Å, nevertheless several protein complexes were already resolved to a higher resolution. Probably the most astonishing is the reconstruction of a bacterial ribosome with bound antibiotic resolved at 3.5 Å resolution²⁹⁸.

For cryo-ET subtomogram averaging the ribosome is almost the ideal sample. Not only is it a relatively big complex, it is also present within the cell in multiple copies and gives a strong signal under the electron microscope due to the presence of nucleic acids. Furthermore, with a bound antibiotic it is relatively rigid. Nevertheless, the example with the ribosome shows that the technique is in principle able to produce maps that in terms of resolution can rival those obtained by single particle cryo-EM.

Ability to investigate proteins in their native environment without the need for purification makes cryo-ET an especially interesting method for structural biologists. Despite the inability of the technique to produce high-resolution maps for majority of the targets, the subtomogram averaging reconstructions are already sufficient to interpret protein complex composition and positions of individual protein domains, especially if structures of the individual proteins have already been solved by other

means, like cryo-EM, X-ray crystallography or NMR. Solving structures of protein complexes solely from cryo-ET subtomogram averaged maps is still not possible in most of the cases.

One of the reasons behind the limited resolution is the time required for both data acquisition and data processing. Recording of a single tomogram takes much longer than recording of a single micrograph and the data processing involves many lengthy additional steps. Still, with the constant improvements of the data processing software and advances in data collection strategies, it is more than likely that cryo-ET will become much faster and more automated in the near future. Perhaps that will be enough to routinely reach 10 Å resolution and beyond.

Regardless of the hypothetical progress, cryo-ET will probably remain a technique suitable only for big complexes. Even with the potential improvements, the technique most likely will not be able to rival structural analysis of medium size (100-500 kDa) protein complexes performed by single particle cryo-EM. Though it may seem like a pessimistic view, so is the cryo-EM still unable to compete with X-ray crystallography when it comes to small proteins (<150 kDa) and/or serial protein complexes done for example in drug discovery/screening process.

The future of structural biology is full of exciting possibilities

Structural biology is still a very young field that emerged in the 1930s. Nevertheless, in just a century the field made a stunning progress. Passion, hard work and relentless efforts of many structural biologists allowed us to glimpse into the unknown and see the world at a scale of molecules. Thinking about the future of such a rapidly developing field is exhilarating.

Will the structural biology lead the way? Will we first observe a biological phenomenon and later try to understand and explain it by means of biophysics, biochemistry and genetics? Will the cryo-ET improve to the stage that allows us to solve structures of protein complexes *in vivo*? Or perhaps yet another method will take the stage and revolutionize the field of structural biology just like the cryo-EM did? It will be exciting to see what the future holds.

Appendix I

Cryo-electron microscopy

Invention and the design of electron microscope

Electron microscope was developed in 1931 by group of Max Knoll at the Technical University of Berlin. Two years later, in 1933, it was already capable of achieving a higher magnification than the light microscope. In 1938 first commercially available electron microscope was produced by Siemens. Following that came a number of groundbreaking studies, which used the electron microscope to look at various biomacromolecules. Discovery of the ribosomes², mentioned in the introduction, is just one such example. Invention of the electron microscope had such a big impact on multiple fields of science, including biology, that in 1986 Ernst Ruska, who co-invented the electron microscope in the Max Knoll's research group and continued to work on it afterwards, was awarded the Nobel Prize in Physics "for his fundamental work in electron optics, and for the design of the first electron microscope". Max Knoll unfortunately could not be considered for the Nobel prize under the rules of the Royal Swedish Academy of Science, as he passed away in 1969.

Both light and electron microscopes are similar in design. Where in the light microscope the photons produced by a light source are guided through the specimen by an array of glass optical lenses, so are the electrons in an electron source directed through the sample by a set of electromagnetic lenses in the electron microscope. The electron source, often called an electron gun, releases electrons in either a thermionic emission or a cold field electron emission. In the thermionic emission a tungsten filament, a lanthanum hexaboride crystal or a ZrO/W Schottky emitter is heated by an electrical current leading to electrons release. In the cold field electron emission, electrons can be induced from a tungsten filament at room temperature by applying an electrostatic field. The cold field electron emission produces higher yield of electrons characterized by a significantly lower chromatic aberration, which makes it possible to achieve much higher resolution. However, it does require a higher vacuum to work. High vacuum is needed at the electron gun to prevent burning of the heated electron source or oxidation of the filament. Regardless of the method of emission, electrons leaving the source have a very low energy and need to be accelerated. That

is achieved by applying a high voltage between the electron source, which acts as a cathode, and an anode plate. Nowadays, most commonly used microscopes operate at 200 or 300 kV voltage.

Accelerated electrons leaving the electron gun are guided through the sample onto the detector by a set of electromagnetic lenses positioned within the microscope column. Electromagnetic lens is usually made of a solenoid coil which produces a magnetic field once electric current pass through it. Electrons entering such a lens are influenced by the Lorentz force and can be focused at a certain point. As such, electromagnetic lenses fulfill the same role as the glass lenses in an optic microscope. However, what gives the electron microscope such flexibility, is the ability to adjust the strength of the magnetic field by adjusting the electric current running through the solenoid coil. While a given glass lens has a specific, set focusing power, an electromagnetic lens' power can simply be changed by adjustment of the current. Multiple sets of electromagnetic lenses, positioned at different places throughout the microscope column provide additional flexibility. First the electron beam is condensed by a condenser lenses system, by which the electron beam brightness (strength) can be controlled. Once adjusted, the electrons pass through the sample and enter an objective lenses system used for primary image formation. Adjustment of the magnetic field of the objective lens affects focus of the image. Finally, electrons are guided through a system of intermediate and projection lenses, which further magnifies the image and projects it onto a fluorescent screen, a photosensitive field or a camera.

Path of the electron beam and consequently the whole column of the microscope needs to be kept under a high vacuum. Even though the vacuum does not need to be so stringent as at the electron gun, any gas molecule present within the column can potentially collide with the electrons and lead to scattering, effectively lowering the resolution of the microscope. High vacuum at the column also affects the sample inserted into the microscope. Most biological specimens, like tissues, cells or proteins, do not behave well under a high vacuum, which quickly leads to their dehydration. Thus, biological samples need to be properly prepared before analysis. In room temperature electron microscopy, the biological sample is therefore chemically fixated, dehydrated and embedded in a solid, transparent material. Such prepared sample is then inserted into the microscope on a small metal grid usually made out of copper, although available out of other materials, like gold or platinum. With a side-entry electron microscope the grid is placed on a long metal rod that

functions as a holder and slid into the column through a vacuum lock. In order for the electrons to be able to pass through the sample, the specimen should not be thicker than approximately 100 nm, although that depends on the energy of the electrons. The higher the voltage at which the microscope operates, the higher the acceleration of electrons and the thicker the sample can be examined. Biological samples prepared in such a way unfortunately provide low contrast in the electron microscope, as the elements building the organic matter like carbon, oxygen, hydrogen and nitrogen interact poorly with the electrons.

Contrast in the transmission electron microscopy is created by either local differences in the intensity of the electron beam (amplitude contrast) or a shift in the electron wavelength (phase contrast). Electrons passing through the sample may stay unaffected or interact with either the atomic nucleus or its electron cloud.

The interaction with the positively charged nucleus is electrostatic in nature and yields an elastically scattered electron or, when the electron is deflected by more than 90° , a backscattered electron. In both cases the affected electron does not lose any significant amount of its kinetic energy. Majority of the scattered electrons are stopped by an objective apparatus - a solid metal plate with a small hole - located below the sample within the microscope, which leads to a local difference in the "concentration" of electrons, thus amplitude contrast formation. In addition to the amplitude contrast generated by absorption of electrons, the elastically scattered electrons experience a phase shift in their wavelength and the interference between the shifted wavelength and the unchanged wavelength of the unscattered electrons leads to the phase contrast formation.

Contrary to the elastic scattering, electrons interacting the electron cloud lose a portion of their kinetic energy and are called inelastically scattered electrons. Deflected at low angles, they are not stopped by the objective apparatus and, having lower kinetic energy, interact with the electromagnetic lenses differently leading to blurring of the image. Nowadays though an energy filter is often used to filter them out.

Contrast formation in the electron microscopy depends on the interactions between the negatively charged electrons and the positively charged nucleus, which is referred to as the Coulomb force. Consequently, the more positively charged protons the nucleus has, the stronger is its interaction with the electrons. This is the reason why heavier atoms, the ones with larger atomic number Z , give rise to the larger amplitude contrast, whereas weaker elements building the organic matter, like

carbon, oxygen, nitrogen and hydrogen, generate less contrast since they interact poorly with the electrons.

To overcome the issue of the low contrast when visualizing biological samples, scientist started staining them with the heavy atoms' solutions, like ammonium molybdate, uranyl formate or uranyl acetate. These solutions absorb well to the biological matter and, because of high number of protons, scatter electrons strongly. As a result, the stained background appears dark under the transmission electron microscope, while the sample remains visible. Thus, the method is called negative staining. It is a simple sample preparation method characterized by a good signal-to-noise ratio and high radiation resistance. It has been used successfully for many years and remains to be one of the main methods at an early stage of many structural studies. It nevertheless has its drawbacks and limitations that one needs to be aware of. First of all, dehydration and staining of the sample may lead to structural artefacts. Furthermore, because of these two processes, the sample is in a non-native environment. Consequently, for this method, the maximal obtainable resolution of the 3D reconstructions is limited to approximately 15 Å.

Single particle cryo-EM

A method that preserves the native hydrated state of the purified molecules is referred to as cryogenic electron microscopy (cryo-EM). This method was pioneered by Jacques Dubochet and his colleague Alasdair McDowell in 1981, when they presented a rapid freezing method which allowed for trapping proteins in a layer of vitreous (non-crystalline) ice²⁹⁹. Not only did this allow for proteins to be inspected in their native state, as it solved the dehydration problem for samples inserted in the evacuated microscope column, freezing also lowered the radiation damage that the sample was exposed to.

Still, the contrast of the sample was too low to allow direct visualization and it was clear that averaging of multiple views of the same particles, according to the mathematical principles established by Aaron Klug and Richard Crowther would be necessary to extract useful information³⁰⁰. In 1980s, Joachim Frank together with Marin van Heel presented a method that allowed for extraction of multiple images of the same protein and their classification based on their structural features and orientation³⁰¹. Created 2D classes composed of multiple images of the same protein significantly improved the signal to noise ratio. Using these 2D projections it became

possible to reconstruct a 3D structure of that protein or protein complex³⁰². In 1999, a year before the structures of the bacterial ribosomal subunits were obtained at high resolution using X-ray crystallography, a cryo-EM structure of the 50S large subunit of *Escherichia coli* ribosome reached 7.5 Å²⁰.

Initially the images were recorded on a photographic film. With the introduction of the software to process the single particles data, the film needed to be digitalized. And so, in 1980s specialized cameras started to be introduced into the electron microscopy. While initially inferior to the photographic film in terms of image quality and attainable maximum resolution, they allowed for an automatization of data acquisition and thus collection of larger datasets³⁰³.

At first, a charge coupled devices (CCD) were used. In electron microscopes these detectors need to be coupled with a scintillator layer, which converts absorbed electrons into photons, as a direct exposure to the high energy electrons damages the device. Because of the necessary conversion though, an additional noise was introduced into the images. In the beginning of 2013, however, direct electron detectors were designed for use in electron microscopy. These cameras were able to detect the electrons directly and record the images with high frame rate. As a consequence, the direct electron detectors are able to operate in a “counting” mode, in which impact of every detected electron is measured. That allows for elimination of a Landau noise originating from a different energy amount deposited by each electron. High frame rate additionally allows for recording of multiple exposures of the same area and creation of so-called “movies”, which allows for correction of the beam-induced movement of the sample.

Overall, the advancement in the data processing software, development of new direct detectors, more advanced microscopes and the increase of computational power over the years lead to what is referred to a “resolution revolution”²⁸⁶. These advancements allowed for calculation of maps of asymmetric molecular complexes at sufficiently high resolution to allow *de novo* structure determination, some examples include structures of the mitoribosomal large subunit solved at 3.4 Å³⁰⁴ and the complete mitoribosome at 3.8 Å³⁹, a structure of the F₄₂₀-reducing [NiFe] hydrogenase at 3.4 Å³⁰⁵ and a structure of the TRPV1 ion channel at 3.4 Å³⁰⁶.

In recognition of their pioneering contributions to the development of cryo-EM methods and their impact on life science studies, Jacques Dubochet, Joachim Frank and Richard Henderson were awarded the Nobel Prize in chemistry in 2017.

Use of cryo-EM and its limitations

The boundaries of what is possible with the cryo-EM are still being pushed. Herzik and colleagues showed in 2019 that it is possible to obtain a structure of 82 kDa protein at 2.7 Å resolution. Furthermore, they also presented a sub-nanometer (<10 Å) resolution structure of a 43 kDa protein³⁰⁷. And not even a year later two structures of apoferritin were reported at 1.25 Å and 1.22 Å resolution^{308,309}.

As every method, cryo-EM also has its limitations. It is still a more expensive technique than X-ray crystallography. And the time required to collect enough images for a high-resolution structure reconstruction is still much longer than with X-ray crystallography³¹⁰. Even with the newest cameras characterized by very high frame rates it is usually necessary to collect for more than 2 days. Despite the fact that proteins crystals are not needed for cryo-EM, the sample preparation is not entirely straightforward. Both the ice thickness and the particle distribution need to be optimized. It often takes several short sessions on the electron microscope to screen for optimal grid preparation conditions for the main data collection. Some proteins or protein complexes can be preferential orientated, making the 3D reconstruction almost impossible and demanding an adjustment in the data collection strategy. Some protein complexes also require an adjustment in the grid preparation procedure, as they tend to fall apart during freezing, most likely because of the contacts with a water-air interface. And even when the sample preparation and data collection are optimized, averaged cryo-EM maps will still not resolve highly flexible fragments of proteins or loosely bound factors.

Despite these limitations, the number of structures solved by cryo-EM is growing exponentially. In 2013, a year of resolution revolution, there were “only” 28 cryo-EM maps at a <5 Å resolution deposited to the Electron Microscopy Data Bank (EMDB). Already in 2018 the number increased 10-fold higher, with 230 maps deposited³¹⁰. According to statistics of the Protein Data Bank (PDB) which holds more than 174 thousand atomic models, 3.94% were solved with cryo-EM, 7.62% with NMR and 88.3% with X-ray crystallography (as of 1/2/2021). While the percentage for cryo-EM structures may seem small, it is important to note that most of these structures are typically much more complex than X-ray structures and were deposited only recently.

References

1. Labeit, S., Kolmerer, B. & Linke, W. A. The Giant Protein Titin: Emerging Roles in Physiology and Pathophysiology. *Circ. Res.* **80**, 290–294 (1997).
2. Palade, G. E. A SMALL PARTICULATE COMPONENT OF THE CYTOPLASM. *J. Cell Biol.* **1**, 59–68 (1955).
3. Noller, H. F. & Herr, W. Nucleotide sequence of the 3' terminus of E. coli 16S ribosomal RNA. *Mol. Biol. Rep.* **1**, 437–439 (1974).
4. Brosius, J., Palmer, M. L., Kennedy, P. J. & Noller, H. F. Complete nucleotide sequence of a 16S ribosomal RNA gene from Escherichia coli. *Proc. Natl. Acad. Sci.* **75**, 4801–4805 (1978).
5. Herr, W. & Noller, H. F. A fragment of 23S RNA containing a nucleotide sequence complementary to a region of 5S RNA. *FEBS Lett.* **53**, 248–252 (1975).
6. Moore, P. B., Traut, R. R., Noller, H., Pearson, P. & Delius, H. Ribosomal proteins of Escherichia coli II. Proteins from the 30 s subunit. *J. Mol. Biol.* **31**, 441–461 (1968).
7. Tischendorf, G. W., Zeichhardt, H. & Stöffler, G. Determination of the location of proteins L14, L17, L18, L19, L22 and L23 on the surface of the 50S ribosomal subunit of Escherichia coli by immune electron microscopy. *Mol. Gen. Genet. MGG* **134**, 187–208 (1974).
8. Tischendorf, G. W., Zeichhardt, H. & Stöffler, G. Location of proteins S5, S13 and S14 on the surface of the 30S ribosomal subunit from Escherichia coli as determined by immune electron microscopy. *Mol. Gen. Genet. MGG* **134**, 209–223 (1974).
9. Möller, K. & Brimacombe, R. Specific cross-linking of proteins S7 and L4 to ribosomal RNA, by UV irradiation of Escherichia coli ribosomal subunits. *Mol. Gen. Genet. MGG* **141**, 343–355 (1975).
10. Moore, P. B. How should we think about the ribosome? *Annu. Rev. Biophys.* **41**, 1–19 (2012).
11. Bernabeu, C. & Lake, J. A. Nascent polypeptide chains emerge from the exit domain of the large ribosomal subunit: immune mapping of the nascent chain. *Proc. Natl. Acad. Sci.* **79**, 3111–3115 (1982).
12. Orlova, E. V. Structural analysis of non-crystalline macromolecules: the ribosome. *Acta Crystallogr. Sect. D Biol. Crystallogr.* **56**, 1253–1258 (2000).
13. Yonath, A., Leonard, K. R. & Wittmann, H. G. A tunnel in the large ribosomal subunit revealed by three-dimensional image reconstruction. *Science (80-.)*. **236**, 813–816 (1987).
14. Makowski, I. *et al.* Single crystals of large ribosomal particles from Halobacterium marismortui diffract to 6 Å. *J. Mol. Biol.* **193**, 819–822 (1987).
15. Wimberly, B. T. *et al.* Structure of the 30S ribosomal subunit. *Nature* **407**, 327–339 (2000).
16. Ban, N., Nissen, P., Hansen, J., Moore, P. B. & Steitz, T. A. The Complete Atomic Structure of the Large Ribosomal Subunit at 2.4 Å Resolution. *Science (80-.)*. **289**, 905–920 (2000).
17. Agrawal, R. K., Penczek, P., Grassucci, R. A. & Frank, J. Visualization of elongation factor G on the Escherichia coli 70S ribosome: The mechanism of translocation. *Proc. Natl. Acad. Sci.* **95**, 6134–6138 (1998).
18. Malhotra, A. *et al.* Escherichia coli 70 S ribosome at 15 Å resolution by cryo-electron microscopy: localization of fmet-tRNA^{fMet} and fitting of L1 protein¹¹Edited by D. Draper. *J. Mol. Biol.* **280**, 103–116 (1998).

19. Stark, H. *et al.* Visualization of elongation factor Tu on the Escherichia coli ribosome. *Nature* **389**, 403–406 (1997).
20. Matadeen, R. *et al.* The Escherichia coli large ribosomal subunit at 7.5 Å resolution. *Structure* **7**, 1575–1583 (1999).
21. Dennis, P. P. & Bremer, H. Macromolecular Composition During Steady-State Growth of Escherichia coli B/r. *J. Bacteriol.* **119**, 270–281 (1974).
22. Karnkowska, A. *et al.* A Eukaryote without a Mitochondrial Organelle. *Curr. Biol.* **26**, 1274–1284 (2016).
23. Spinelli, J. B. & Haigis, M. C. The multifaceted contributions of mitochondria to cellular metabolism. *Nat. Cell Biol.* **20**, 745–754 (2018).
24. Ferrari, A., Del’Olio, S. & Barrientos, A. The Diseased Mitoribosome. *FEBS Lett.* **595**, 1025–1061 (2021).
25. Palade, G. E. AN ELECTRON MICROSCOPE STUDY OF THE MITOCHONDRIAL STRUCTURE. *J. Histochem. Cytochem.* **1**, 188–211 (1953).
26. McLean, J. R., Cohn, G. L., Brandt, I. K. & Simpson, M. V. Incorporation of Labeled Amino Acids into the Protein of Muscle and Liver Mitochondria. *J. Biol. Chem.* **233**, 657–663 (1958).
27. Rendi, R. On the occurrence of intramitochondrial ribonucleoprotein particles. *Exp. Cell Res.* **17**, 585–587 (1959).
28. Swift, H. Nucleic Acids of Mitochondria and Chloroplasts. *Am. Nat.* **99**, 201–227 (1965).
29. Küntzel, H. & Noll, H. Mitochondrial and cytoplasmic polysomes from Neurospora crassa. *Nature* **215**, 1340–1345 (1967).
30. O’Brien, T. W. & Kalf, G. F. Ribosomes from Rat Liver Mitochondria I. ISOLATION PROCEDURE AND CONTAMINATION STUDIES. *J. Biol. Chem.* **242**, 2172–2179 (1967).
31. Sagan, L. On the origin of mitosing cells. *J. Theor. Biol.* **14**, 225–IN6 (1967).
32. Gray, M. W., Burger, G. & Lang, F. B. Mitochondrial Evolution. *Science (80-.)*. **283**, 1476–1481 (1999).
33. Martijn, J., Vosseberg, J., Guy, L., Offre, P. & Ettema, T. J. G. Deep mitochondrial origin outside the sampled alphaproteobacteria. *Nature* **557**, 101–105 (2018).
34. Gray, M. W. Mosaic nature of the mitochondrial proteome: Implications for the origin and evolution of mitochondria. *Proc. Natl. Acad. Sci.* **112**, 10133–10138 (2015).
35. Burger, G., Gray, M. W., Forget, L. & Lang, B. F. Strikingly Bacteria-Like and Gene-Rich Mitochondrial Genomes throughout Jakobid Protists. *Genome Biol. Evol.* **5**, 418–438 (2013).
36. Feagin, J. E. *et al.* The Fragmented Mitochondrial Ribosomal RNAs of Plasmodium falciparum. *PLoS One* **7**, e38320 (2012).
37. Taanman, J.-W. The mitochondrial genome: structure, transcription, translation and replication. *Biochim. Biophys. Acta - Bioenerg.* **1410**, 103–123 (1999).
38. Sharma, M. R. *et al.* Structure of the Mammalian Mitochondrial Ribosome Reveals an Expanded Functional Role for Its Component Proteins. *Cell* **115**, 97–108 (2003).
39. Greber, B. J. *et al.* The complete structure of the 55S mammalian mitochondrial ribosome. *Science (80-.)*. **348**, 303–308 (2015).

40. Amunts, A., Brown, A., Toots, J., Scheres, S. H. W. & Ramakrishnan, V. The structure of the human mitochondrial ribosome. *Science* (80-.). **348**, 95–98 (2015).
41. Desai, N., Brown, A., Amunts, A. & Ramakrishnan, V. The structure of the yeast mitochondrial ribosome. *Science* (80-.). **355**, 528–531 (2017).
42. Ramrath, D. J. F. *et al.* Evolutionary shift toward protein-based architecture in trypanosomal mitochondrial ribosomes. *Science* (80-.). **362**, (2018).
43. Tobiasson, V. & Amunts, A. Ciliate mitoribosome illuminates evolutionary steps of mitochondrial translation. *Elife* **9**, 1–15 (2020).
44. Waltz, F. *et al.* Cryo-EM structure of the RNA-rich plant mitochondrial ribosome. *nature.com*.
45. Noeske, J. *et al.* High-resolution structure of the Escherichia coli ribosome. *Nat. Struct. & Mol. Biol.* **22**, 336–341 (2015).
46. Rodnina, M. V. Translation in Prokaryotes. *Cold Spring Harb. Perspect. Biol.* **10**, a032664 (2018).
47. Javed, A. & Orlova, E. V. Unravelling Ribosome Function Through Structural Studies. *Subcell. Biochem.* **93**, 53–81 (2019).
48. Freed, E. F., Bleichert, F., Dutca, L. M. & Baserga, S. J. When ribosomes go bad: diseases of ribosome biogenesis. *Mol. Biosyst.* **6**, 481–493 (2010).
49. Neidhardt, F. C., Ingraham, J. L. & Schaechter, M. *Physiology of the bacterial cell; a molecular approach.* (Sinauer associates).
50. Sachla, A. J. & Helmann, J. D. A bacterial checkpoint protein for ribosome assembly moonlights as an essential metabolite-proofreading enzyme. *Nat. Commun.* **10**, 1–12 (2019).
51. Lindahl, L. Intermediates and Time Kinetics of the in vivo Assembly of Escherichia coli Ribosomes. *J. Mol. Biol.* **92**, 15–37 (1975).
52. Traub, P. & Nomura, M. Structure and function of E. coli ribosomes. V. Reconstitution of functionally active 30S ribosomal particles from RNA and proteins. *Proc. Natl. Acad. Sci.* **59**, 777–784 (1968).
53. Mizushima, S. & Nomura, M. Assembly Mapping of 30S Ribosomal Proteins from E. coli. *Nature* **226**, 2261214a0 (1970).
54. Nomura, M., Traub, P., Guthrie, C. & Nashimoto, H. The assembly of ribosomes. *J. Cell. Physiol.* **74**, 241–251 (1969).
55. Weitzmann, C. J., Cunningham, P. R., Nurse, K. & Ofengand, J. Chemical evidence for domain assembly of the Escherichia coli 30S ribosome. *FASEB J.* **7**, 177–180 (1993).
56. Samaha, R. R., O'Brien, B., O'Brien, T. W. & Noller, H. F. Independent in vitro assembly of a ribonucleoprotein particle containing the 3' domain of 16S rRNA. *Proc. Natl. Acad. Sci.* **91**, 7884–7888 (1994).
57. Agalarov, S. C. *et al.* In vitro assembly of a ribonucleoprotein particle corresponding to the platform domain of the 30S ribosomal subunit. *Proc. Natl. Acad. Sci.* **95**, 999–1003 (1998).
58. Nierhaus, K. H. & Dohme, F. Total Reconstitution of Functionally Active 50S Ribosomal Subunits from Escherichia coli. *Proc. Natl. Acad. Sci.* **71**, 4713–4717 (1974).
59. Rohl, R. & Nierhaus, K. H. Assembly map of the large subunit (50S) of Escherichia coli ribosomes. *Proc. Natl. Acad. Sci. U. S. A.* **79**, 729–733 (1982).

60. Sieber, G. & Nierhaus, K. H. Kinetic and Thermodynamic Parameters of the Assembly in Vitro of the Large Subunit from Escherichia coli Ribosomes. *Biochemistry* **17**, 3505–3511 (1978).
61. Srivastava, A. K. & Schlessinger, D. Mechanism and regulation of bacterial ribosomal RNA processing. *Annual Review of Microbiology* vol. 44 105–129 (1990).
62. Lindahl, L. Two new ribosomal precursor particles in E. coli. *Nat. New Biol.* **243**, 170–172 (1973).
63. Wireman, J. W. & Sypherd, P. S. In vitro assembly of 30S ribosomal particles from precursor 16S RNA of escherichia coli. *Nature* **247**, 552–554 (1974).
64. Comartin, D. J. & Brown, E. D. Non-ribosomal factors in ribosome subunit assembly are emerging targets for new antibacterial drugs. *Curr. Opin. Pharmacol.* **6**, 453–458 (2006).
65. Klinge, S. & Woolford, J. L. Ribosome assembly coming into focus. *Nat. Rev. Mol. Cell Biol.* **20**, 116–131 (2018).
66. Silva, D. De *et al.* Mitochondrial ribosome assembly in health and disease. *Cell Cycle* **14**, 2226–2250 (2015).
67. Fatica, A. & Tollervey, D. Making ribosomes. *Current Opinion in Cell Biology* vol. 14 313–318 (2002).
68. Woolford, J. L. & Baserga, S. J. Ribosome Biogenesis in the Yeast *Saccharomyces cerevisiae*. *Genetics* **195**, 643–681 (2013).
69. Kaczanowska, M. & Rydén-Aulin, M. Ribosome Biogenesis and the Translation Process in Escherichia coli. *Microbiol. Mol. Biol. Rev.* **71**, 477–494 (2007).
70. Sergeeva, O. V., Sergiev, P. V., Bogdanov, A. A. & Dontsova, O. A. Ribosome: Lessons of a molecular factory construction. *Mol. Biol.* **48**, 468–484 (2014).
71. Krzyzosiak, W. *et al.* In vitro synthesis of 16S ribosomal RNA containing single base changes and assembly into a functional 30S ribosome. *Biochemistry* **26**, 2353–2364 (1987).
72. Green, R. & Noller, H. F. In vitro complementation analysis localizes 23S rRNA posttranscriptional modifications that are required for Escherichia coli 50S ribosomal subunit assembly and function. *RNA* **2**, 1011–1021 (1996).
73. Alix, J. H., Hayes, D. & Nierhaus, K. H. Properties of ribosomes and RNA synthesized by Escherichia coli grown in the presence of ethionine. V. Methylation dependence of the assembly of E. coli 50 S ribosomal subunits. *J. Mol. Biol.* **127**, 375–395 (1979).
74. Sergeeva, O. V, Bogdanov, A. A. & Sergiev, P. V. What do we know about ribosomal RNA methylation in Escherichia coli? *Biochimie* **117**, 110–118 (2015).
75. Garcia, I., Albring, M. J. & Uhlenbeck, O. C. Duplex destabilization by four ribosomal DEAD-box proteins. *Biochemistry* **51**, 10109–10118 (2012).
76. Fairman-Williams, M., ... U. G.-C. opinion in & 2010, undefined. SF1 and SF2 helicases: family matters. *Elsevier*.
77. Linder, P., biology, E. J.-N. reviews M. cell & 2011, undefined. From unwinding to clamping—the DEAD box RNA helicase family. *nature.com*.
78. Jagessar, K. L. & Jain, C. Functional and molecular analysis of Escherichia coli strains lacking multiple DEAD-box helicases. *RNA* **16**, 1386–1392 (2010).
79. Shajani, Z., Sykes, M. T. & Williamson, J. R. Assembly of Bacterial Ribosomes. *Annu. Rev.*

- Biochem.* **80**, 501–526 (2011).
80. Verstraeten, N., Fauvart, M., Versées, W. & Michiels, J. The Universally Conserved Prokaryotic GTPases. *Microbiol. Mol. Biol. Rev.* **75**, 507–542 (2011).
 81. Britton, R. A. Role of GTPases in Bacterial Ribosome Assembly. *Annu. Rev. Microbiol.* **63**, 155–176 (2009).
 82. El Hage, A. *et al.* The chaperonin GroEL and other heat-shock proteins, besides DnaK, participate in ribosome biogenesis in *Escherichia coli*. **264**, 796–808 (2001).
 83. Maki, J. A., Schnobrich, D. J. & Culver, G. M. The DnaK chaperone system facilitates 30S ribosomal subunit assembly. *Mol. Cell* **10**, 129–138 (2002).
 84. Alix, J. H. & Guerin, M. F. Mutant DnaK chaperones cause ribosome assembly defects in *Escherichia coli*. *Proc. Natl. Acad. Sci. U. S. A.* **90**, 9725–9729 (1993).
 85. Alix, J.-H. & Nierhaus, K. H. DnaK-facilitated ribosome assembly in *Escherichia coli* revisited. *rnajournal.cshlp.org* **9**, 787–793 (2003).
 86. Al Refaii, A. & Alix, J. H. Ribosome biogenesis is temperature-dependent and delayed in *Escherichia coli* lacking the chaperones DnaK or DnaJ. *Mol. Microbiol.* **71**, 748–762 (2009).
 87. Jones, P. G. & Inouye, M. RbfA, a 30S ribosomal binding factor, is a cold-shock protein whose absence triggers the cold-shock response. *Mol. Microbiol.* **21**, 1207–1218 (1996).
 88. Dammel, C. S. & Noller, H. F. Suppression of a cold-sensitive mutation in 16S rRNA by overexpression of a novel ribosome-binding factor, RbfA. *Genes Dev.* **9**, 626–637 (1995).
 89. Huang, Y. J. *et al.* Solution NMR structure of ribosome-binding factor A (RbfA), a cold-shock adaptation protein from *Escherichia coli*. *J. Mol. Biol.* **327**, 521–536 (2003).
 90. Datta, P. P. *et al.* Structural Aspects of RbfA Action during Small Ribosomal Subunit Assembly. *Mol. Cell* **28**, 434–445 (2007).
 91. Bylund, G. O., Wipemo, L. C., Lundberg, L. A. C. & Wikström, P. M. RimM and RbfA are essential for efficient processing of 16S rRNA in *Escherichia coli*. *J. Bacteriol.* **180**, 73–82 (1998).
 92. Xia, B., Ke, H., Shinde, U. & Inouye, M. The role of RbfA in 16 S rRNA processing and cell growth at low temperature in *Escherichia coli*. *J. Mol. Biol.* **332**, 575–584 (2003).
 93. Lövgren, J. M. *et al.* The PRC-barrel domain of the ribosome maturation protein RimM mediates binding to ribosomal protein S19 in the 30S ribosomal subunits. *RNA* **10**, 1798–1812 (2004).
 94. Bylund, G. O., Persson, B. C., Lundberg, L. A. C. & Wikström, P. M. A novel ribosome-associated protein is important for efficient translation in *Escherichia coli*. *J. Bacteriol.* **179**, 4567–4574 (1997).
 95. Nord, S., Bylund, G. O., Lövgren, J. M. & Wikström, P. M. The RimP Protein Is Important for Maturation of the 30S Ribosomal Subunit. *J. Mol. Biol.* **386**, 742–753 (2009).
 96. Roy-Chaudhuri, B., Kirthi, N., Kelley, T. & Culver, G. M. Suppression of a cold-sensitive mutation in ribosomal protein S5 reveals a role for RimJ in ribosome biogenesis. *Mol. Microbiol.* **68**, 1547–1559 (2008).
 97. Boehringer, D., O'Farrell, H. C., Rife, J. P. & Ban, N. Structural insights into methyltransferase KsgA function in 30S ribosomal subunit biogenesis. *J. Biol. Chem.* **287**, 10453–10459 (2012).

98. Stephan, N. C., Ries, A. B., Boehringer, D. & Ban, N. Structural basis of successive adenosine modifications by the conserved ribosomal methyltransferase KsgA. *Nucleic Acids Res.* gkab430- (2021) doi:10.1093/nar/gkab430 PMID - 34086932.
99. Connolly, K., Rife, J. P. & Culver, G. Mechanistic insight into the ribosome biogenesis functions of the ancient protein KsgA. *Mol. Microbiol.* **70**, 1062–1075 (2008).
100. Demirci, H. *et al.* Modification of 16S ribosomal RNA by the KsgA methyltransferase restructures the 30S subunit to optimize ribosome function. *RNA* **16**, 2319–2324 (2010).
101. Sunita, S. *et al.* Functional specialization of domains tandemly duplicated within 16S rRNA methyltransferase RsmC. *Nucleic Acids Res.* **35**, 4264–4274 (2007).
102. Tscherne, J. S., Nurse, K., Popienick, P. & Ofengand, J. Purification, cloning, and characterization of the 16 S RNA m2G1207 methyltransferase from *Escherichia coli*. *J. Biol. Chem.* **274**, 924–929 (1999).
103. Bijpuria, S., Sharma, R. & Taneja, B. Loss of U1498 methylation in 16S rRNA by RsmE methyltransferase associates its role with aminoglycoside resistance in mycobacteria. *J. Glob. Antimicrob. Resist.* **23**, 359–369 (2020).
104. Hallberg, B. M. *et al.* The Structure of the RNA m5C Methyltransferase YebU from *Escherichia coli* Reveals a C-terminal RNA-recruiting PUA Domain. *J. Mol. Biol.* **360**, 774–787 (2006).
105. Andersen, N. M. & Douthwaite, S. YebU is a m5C Methyltransferase Specific for 16 S rRNA Nucleotide 1407. *J. Mol. Biol.* **359**, 777–786 (2006).
106. Benítez-Páez, A., Villarroya, M. & Armengod, M. E. Regulation of expression and catalytic activity of *Escherichia coli* RsmG methyltransferase. *RNA* **18**, 795–806 (2012).
107. Gregory, S. T. *et al.* Structural and functional studies of the *Thermus thermophilus* 16S rRNA methyltransferase RsmG. *RNA* **15**, 1693–1704 (2009).
108. Nishimura, K. *et al.* Identification of the RsmG methyltransferase target as 16S rRNA nucleotide G527 and characterization of *Bacillus subtilis* rsmG mutants. *J. Bacteriol.* **189**, 6068–6073 (2007).
109. Abedeera, S. M., Hawkins, C. M., Hawkins, C. M. & Abeyvirigunawardena, S. C. RsmG forms stable complexes with premature small subunit rRNA during bacterial ribosome biogenesis. *RSC Adv.* **10**, 22361–22369 (2020).
110. Foster, P. G., Nunes, C. R., Greene, P., Moustakas, D. & Stroud, R. M. The First Structure of an RNA m5C Methyltransferase, Fmu, Provides Insight into Catalytic Mechanism and Specific Binding of RNA Substrate. *Structure* **11**, 1609–1620 (2003).
111. Gu, X. R., Gustafsson, C., Ku, J., Yu, M. & Santi, D. V. Identification of the 16S rRNA m5C967 methyltransferase from *Escherichia coli*. *Biochemistry* **38**, 4053–4057 (1999).
112. Keshav, G. C., Gyawali, P., Balci, H. & Abeyvirigunawardena, S. Ribosomal RNA Methyltransferase RsmC Moonlights as an RNA Chaperone. *ChemBioChem* **21**, 1885–1892 (2020).
113. Lesnyak, D. V. *et al.* Methyltransferase that modifies guanine 966 of the 16 S rRNA: Functional identification and tertiary structure. *J. Biol. Chem.* **282**, 5880–5887 (2007).
114. Sergeeva, O. V. *et al.* Properties of small rRNA methyltransferase RsmD: Mutational and kinetic study. *RNA* **18**, 1178–1185 (2012).
115. Zhang, H. *et al.* Insights into the Catalytic Mechanism of 16S rRNA Methyltransferase RsmE (m3U1498) from Crystal and Solution Structures. *J. Mol. Biol.* **423**, 576–589 (2012).

116. Basturea, G. N. & Deutscher, M. P. Substrate specificity and properties of the Escherichia coli 16S rRNA methyltransferase, RsmE. *RNA* **13**, 1969–1976 (2007).
117. Basturea, G. N., Rudd, K. E. & Deutscher, M. P. Identification and characterization of RsmE, the founding member of a new RNA base methyltransferase family. *RNA* **12**, 426–434 (2006).
118. Jayalath, K., Frisbie, S., To, M. & Abeysirigunawardena, S. Pseudouridine synthase rsua captures an assembly intermediate that is stabilized by ribosomal protein S17. *Biomolecules* **10**, 841 (2020).
119. Sivaraman, J. *et al.* Structure of the 16S rRNA pseudouridine synthase, RsuA bound to uracil and UMP. *Nat. Struct. Biol.* **9**, 353–358 (2002).
120. Conrad, J., Niu, L., Rudd, K., Lane, B. G. & Ofengand, J. 16S ribosomal RNA pseudouridine synthase RsuA of Escherichia coli: Deletion, mutation of the conserved Asp102 residue, and sequence comparison among all other pseudouridine synthases. *RNA* **5**, 751–763 (1999).
121. Wrzesinski, J., Bakin, A., Nurse, K., Lane, B. G. & Ofengand, J. Purification, Cloning, and Properties of the 16S RNA Pseudouridine 516 Synthase from Escherichia coli. *Biochemistry* **34**, 8904–8913 (1995).
122. Das, K. *et al.* Crystal structure of RlmAI: Implications for understanding the 23S rRNA G745/G748-methylation at the macrolide antibiotic-binding site. *Proc. Natl. Acad. Sci. U. S. A.* **101**, 4041–4046 (2004).
123. Gustafsson, C. & Persson, B. C. Identification of the rrmA gene encoding the 23S rRNA m1G745 methyltransferase in Escherichia coli and characterization of an m1G745- deficient mutant. *J. Bacteriol.* **180**, 359–365 (1998).
124. Hansen, L. H., Kirpekar, F. & Douthwaite, S. Recognition of nucleotide G745 in 23 S ribosomal RNA by the RrmA methyltransferase. *J. Mol. Biol.* **310**, 1001–1010 (2001).
125. Wang, K. T. *et al.* Structure of the bifunctional methyltransferase YcbY (RlmKL) that adds the m⁷G2069 and m²G2445 modifications in Escherichia coli 23S rRNA. *Nucleic Acids Res.* **40**, 5138–5148 (2012).
126. Lesnyak, D. V., Sergiev, P. V., Bogdanov, A. A. & Dontsova, O. A. Identification of Escherichia coli m²G methyltransferases: I. The ycbY Gene Encodes a Methyltransferase Specific for G2445 of the 23 S rRNA. *J. Mol. Biol.* **364**, 20–25 (2006).
127. Pletnev, P. *et al.* Comprehensive Functional Analysis of Escherichia coli Ribosomal RNA Methyltransferases. *Front. Genet.* **11**, 97 (2020).
128. Michel, G. *et al.* The structure of the RlmB 23S rRNA methyltransferase reveals a new methyltransferase fold with a unique knot. *Structure* **10**, 1303–1315 (2002).
129. Lövgren, J. M. & Wikström, P. M. The rlmB gene is essential for formation of Gm2251 in 23S rRNA but not for ribosome maturation in Escherichia coli. *J. Bacteriol.* **183**, 6957–6960 (2001).
130. Zhang, H. *et al.* Structural insights into the function of 23S rRNA methyltransferase RlmG (m²G1835) from Escherichia coli. *RNA* **18**, 1500–1509 (2012).
131. Sergiev, P. V., Lesnyak, D. V., Bogdanov, A. A. & Dontsova, O. A. Identification of Escherichia coli m²G methyltransferases: II. The ygjO Gene Encodes a Methyltransferase Specific for G1835 of the 23 S rRNA. *J. Mol. Biol.* **364**, 26–31 (2006).
132. Osterman, I. A. *et al.* Methylated 23S rRNA nucleotide m²G1835 of Escherichia coli ribosome facilitates subunit association. *Biochimie* **93**, 725–729 (2011).
133. Arai, T. *et al.* Single methylation of 23S rRNA triggers late steps of 50S ribosomal subunit

- assembly. *Proc. Natl. Acad. Sci. U. S. A.* **112**, E4707–E4716 (2015).
134. Agarwalla, S., Kealey, J. T., Santi, D. V. & Stroud, R. M. Characterization of the 23 S ribosomal RNA m5U1939 methyltransferase from *Escherichia coli*. *J. Biol. Chem.* **277**, 8835–8840 (2002).
 135. Lee, T. T., Agarwalla, S. & Stroud, R. M. A unique RNA fold in the RumA-RNA-cofactor ternary complex contributes to substrate selectivity and enzymatic function. *Cell* **120**, 599–611 (2005).
 136. Lee, T. T., Agarwalla, S. & Stroud, R. M. Crystal structure of RumA, an iron-sulfur cluster containing *E. coli* ribosomal RNA 5-methyluridine methyltransferase. *Structure* **12**, 397–407 (2004).
 137. Madsen, C. T., Mengel-Jørgensen, J., Kirpekar, F. & Douthwaite, S. Identifying the methyltransferases for m5U747 and m5U1939 in 23S rRNA using MALDI mass spectrometry. *Nucleic Acids Res.* **31**, 4738–4746 (2003).
 138. Addepalli, B. & Limbach, P. A. Pseudouridine in the anticodon of *Escherichia coli* tRNA^{Tyr}(QΨA) is catalyzed by the dual specificity enzyme RluF. *J. Biol. Chem.* **291**, 22327–22337 (2016).
 139. Sunita, S. *et al.* Domain Organization and Crystal Structure of the Catalytic Domain of *E. coli* RluF, a Pseudouridine Synthase that Acts on 23S rRNA. *J. Mol. Biol.* **359**, 998–1009 (2006).
 140. Mizutani, K., Machida, Y., Unzai, S., Park, S. Y. & Tame, J. R. H. Crystal Structures of the Catalytic Domains of Pseudouridine Synthases RluC and RluD from *Escherichia coli*. *Biochemistry* **43**, 4454–4463 (2004).
 141. Czudnochowski, N. *et al.* The mechanism of pseudouridine synthases from a covalent complex with RNA, and alternate specificity for U2605 versus U2604 between close homologs. *Nucleic Acids Res.* **42**, 2037–2048 (2014).
 142. Raychaudhuri, S., Conrad, J., Hall, B. G. & Ofengand, J. A pseudouridine synthase required for the formation of two universally conserved pseudouridines in ribosomal RNA is essential for normal growth of *Escherichia coli*. *RNA* **4**, 1407–1417 (1998).
 143. Alian, A., DeGiovanni, A., Griner, S. L., Finer-Moore, J. S. & Stroud, R. M. Crystal Structure of an RluF-RNA Complex: A Base-Pair Rearrangement Is the Key to Selectivity of RluF for U2604 of the Ribosome. *J. Mol. Biol.* **388**, 785–800 (2009).
 144. Hoang, C. *et al.* Crystal structure of pseudouridine synthase RluA: Indirect sequence readout through protein-induced RNA structure. *Mol. Cell* **24**, 535–545 (2006).
 145. Raychaudhuri, S., Niu, L., Conrad, J., Lane, B. G. & Ofengand, J. Functional effect of deletion and mutation of the *Escherichia coli* ribosomal RNA and tRNA pseudouridine synthase RluA. *J. Biol. Chem.* **274**, 18880–18886 (1999).
 146. Ofengand, J. Ribosomal RNA pseudouridines and pseudouridine synthases. in *FEBS Letters* vol. 514 17–25 (No longer published by Elsevier, 2002).
 147. Tillault, A. S., Schultz, S. K., Wieden, H. J. & Kothe, U. Molecular Determinants for 23S rRNA Recognition and Modification by the *E. coli* Pseudouridine Synthase RluE. *J. Mol. Biol.* **430**, 1284–1294 (2018).
 148. Pan, H., Ho, J. D., Stroud, R. M. & Finer-Moore, J. The Crystal Structure of *E. coli* rRNA Pseudouridine Synthase RluE. *J. Mol. Biol.* **367**, 1459–1470 (2007).
 149. Wrzesinski, J., Bakin, A., Ofengand, J. & Lane, B. G. Isolation and properties of *Escherichia coli* 23S-RNA pseudouridine 1911, 1915, 1917 synthase (RluD). *IUBMB Life* **50**, 33–37 (2000).

150. Leppik, M., Peil, L., Kipper, K., Liiv, A. & Remme, J. Substrate specificity of the pseudouridine synthase RluD in *Escherichia coli*. *FEBS J.* **274**, 5759–5766 (2007).
151. Gutsell, N. S., Deutscher, M. P. & Ofengand, J. The pseudouridine synthase RluD is required for normal ribosome assembly and function in *Escherichia coli*. *RNA* **11**, 1141–1152 (2005).
152. A pseudouridine synthase required for the formation of two universally conserved pseudouridines in ribosomal RNA is essential for normal growth of *Escherichia coli*. <https://rnajournal.cshlp.org/content/4/11/1407.short>.
153. Conrad, J., Sun, D., Englund, N. & Ofengand, J. The rluC gene of *Escherichia coli* codes for a pseudouridine synthase that is solely responsible for synthesis of pseudouridine at positions 955, 2504, and 2580 in 23 S ribosomal RNA. *J. Biol. Chem.* **273**, 18562–18566 (1998).
154. Toone, W. M., Rudd, K. E. & Friesen, J. D. deaD, a new *Escherichia coli* gene encoding a presumed ATP-dependent RNA helicase, can suppress a mutation in rpsB, the gene encoding ribosomal protein S2. *J. Bacteriol.* **173**, 3291–3302 (1991).
155. Jones, P. G., Mitta, M., Kim, Y., Jiang, W. & Inouye, M. Cold shock induces a major ribosomal-associated protein that unwinds double-stranded RNA in *Escherichia coli*. *Proc. Natl. Acad. Sci. U. S. A.* **93**, 76–80 (1996).
156. Charollais, J., Dreyfus, M. & Iost, I. CsdA, a cold-shock RNA helicase from *Escherichia coli*, is involved in the biogenesis of 50S ribosomal subunit. *Nucleic Acids Res.* **32**, 2751–2759 (2004).
157. Peil, L., Virumäe, K. & Remme, J. Ribosome assembly in *Escherichia coli* strains lacking the RNA helicase DeaD/CsdA or DbpA. *FEBS J.* **275**, 3772–3782 (2008).
158. Moore, A. F. T., Gentry, R. C. & Koculi, E. DbpA is a region-specific RNA helicase. *Biopolymers* **107**, e23001 (2017).
159. Sharpe Elles, L. M., Sykes, M. T., Williamson, J. R. & Uhlenbeck, O. C. A dominant negative mutant of the *E. coli* RNA helicase DbpA blocks assembly of the 50S ribosomal subunit. *Nucleic Acids Res.* **37**, 6503–6514 (2009).
160. Henn, A. *et al.* Pathway of ATP utilization and duplex rRNA unwinding by the DEAD-box helicase, DbpA. *Proc. Natl. Acad. Sci. U. S. A.* **107**, 4046–4050 (2010).
161. The *Escherichia coli* DEAD protein DbpA recognizes a small RNA hairpin in 23S rRNA. <https://rnajournal.cshlp.org/content/7/5/702.short>.
162. Fuller-Space, F. V., Nicol, S. M., Reid, A. D. & Lane, D. P. DbpA: A DEAD box protein specifically activated by 23S rRNA. *EMBO J.* **12**, 3619–3626 (1993).
163. Diges, C. M. & Uhlenbeck, O. C. *Escherichia coli* DbpA is an RNA helicase that requires hairpin 92 of 23S rRNA. *EMBO J.* **20**, 5503–5512 (2001).
164. Diges, C. M. & Uhlenbeck, O. C. *Escherichia coli* DbpA is a 3' → 5' RNA helicase. *Biochemistry* **44**, 7903–7911 (2005).
165. Nishi, K., Morel-Deville, F., Hershey, J. W. B., Leighton, T. & Schnier, J. An eIF-4A-like protein is a suppressor of an *Escherichia coli* mutant defective in 50S ribosomal subunit assembly. *Nature* **336**, 496–498 (1988).
166. Rabuck-Gibbons, J. N. *et al.* SrmB Rescues Trapped Ribosome Assembly Intermediates. *J. Mol. Biol.* **432**, 978–990 (2020).
167. Proux, F., Dreyfus, M. & Iost, I. Identification of the sites of action of SrmB, a DEAD-box RNA helicase involved in *Escherichia coli* ribosome assembly. *Mol. Microbiol.* **82**, 300–311 (2011).

168. Trubetsky, D., Proux, F., Allemand, F., Dreyfus, M. & Iost, I. SrmB, a DEAD-box helicase involved in Escherichia coli ribosome assembly, is specifically targeted to 23S rRNA in vivo. *Nucleic Acids Res.* **37**, 6540–6549 (2009).
169. Charollais, J., Pflieger, D., Vinh, J., Dreyfus, M. & Iost, I. The DEAD-box RNA helicase SrmB is involved in the assembly of 50S ribosomal subunits in Escherichia coli. *Mol. Microbiol.* **48**, 1253–1265 (2003).
170. Jain, C. The E. coli RhlE RNA helicase regulates the function of related RNA helicases during ribosome assembly. *RNA* **14**, 381–389 (2008).
171. Seffouh, A. *et al.* Structural consequences of the interaction of RbgA with a 50S ribosomal subunit assembly intermediate. *Nucleic Acids Res.* **47**, 10414–10425 (2019).
172. Achila, D., Gulati, M., Jain, N. & Britton, R. A. Biochemical characterization of ribosome assembly gtpase RbgA in Bacillus subtilis. *J. Biol. Chem.* **287**, 8417–8423 (2012).
173. Gulati, M., Jain, N., Anand, B., Prakash, B. & Britton, R. A. Mutational analysis of the ribosome assembly GTPase RbgA provides insight into ribosome interaction and ribosome-stimulated GTPase activation. *Nucleic Acids Res.* **41**, 3217–3227 (2013).
174. Jomaa, A. *et al.* Functional domains of the 50S subunit mature late in the assembly process. *Nucleic Acids Res.* **42**, 3419–3435 (2014).
175. Gulati, M., Jain, N., Davis, J. H., Williamson, J. R. & Britton, R. A. Functional Interaction between Ribosomal Protein L6 and RbgA during Ribosome Assembly. *PLoS Genet.* **10**, e1004694 (2014).
176. Pausch, P. *et al.* Structural basis for (p)ppGpp-mediated inhibition of the GTPase RbgA. *J. Biol. Chem.* **293**, 19699–19709 (2018).
177. Matsuo, Y. *et al.* The GTP-binding protein YlqF participates in the late step of 50 S ribosomal subunit assembly in Bacillus subtilis. *J. Biol. Chem.* **281**, 8110–8117 (2006).
178. Uicker, W. C., Schaefer, L. & Britton, R. A. The essential GTPase RbgA (YlqF) is required for 50S ribosome assembly in Bacillus subtilis. *Mol. Microbiol.* **59**, 528–540 (2006).
179. Feng, B. *et al.* Structural and Functional Insights into the Mode of Action of a Universally Conserved Obg GTPase. *PLoS Biol.* **12**, 1001866 (2014).
180. Sato, A. *et al.* The GTP binding protein Obg homolog ObgE is involved in ribosome maturation. *Genes to Cells* **10**, 393–408 (2005).
181. Wout, P. *et al.* The Escherichia coli GTPase CgtAE cofractionates with the 50S ribosomal subunit and interacts with spot, a ppGpp synthetase/hydrolase. *J. Bacteriol.* **186**, 5249–5257 (2004).
182. Jiang, M. *et al.* The Escherichia coli GTPase CgtAE is involved in late steps of large ribosome assembly. *J. Bacteriol.* **188**, 6757–6770 (2006).
183. Ruzheinikov, S. N. *et al.* Analysis of the open and closed conformations of the GTP-binding protein YsxC from Bacillus subtilis. *J. Mol. Biol.* **339**, 265–278 (2004).
184. Wicker-Planquart, C., Ceres, N. & Jault, J. M. The C-terminal α -helix of YsxC is essential for its binding to 50S ribosome and rRNAs. *FEBS Lett.* **589**, 2080–2086 (2015).
185. Ni, X. *et al.* YphC and YsxC GTPases assist the maturation of the central protuberance, GTPase associated region and functional core of the 50S ribosomal subunit. *Nucleic Acids Res.* **44**, 8442–8455 (2016).

186. Cooper, E. L., García-Lara, J. & Foster, S. J. YsxC, an essential protein in *Staphylococcus aureus* crucial for ribosome assembly/stability. *BMC Microbiol.* **9**, 1–12 (2009).
187. Wicker-Planquart, C. & Jault, J. M. Interaction between *Bacillus subtilis* YsxC and ribosomes (or rRNAs). *FEBS Lett.* **589**, 1026–1032 (2015).
188. da Silveira Tomé, C., Foucher, A. E., Jault, J. M. & Housset, D. High concentrations of GTP induce conformational changes in the essential bacterial GTPase EngA and enhance its binding to the ribosome. *FEBS J.* **285**, 160–177 (2018).
189. Zhang, X. *et al.* Structural insights into the function of a unique tandem GTPase EngA in bacterial ribosome assembly. *Nucleic Acids Res.* **42**, 13430–13439 (2014).
190. Bharat, A. & Brown, E. D. Phenotypic investigations of the depletion of EngA in *Escherichia coli* are consistent with a role in ribosome biogenesis. *FEMS Microbiology Letters* vol. 353 26–32 (2014).
191. Bharat, A., Jiang, M., Sullivan, S. M., Maddock, J. R. & Brown, E. D. Cooperative and critical roles for both G domains in the GTPase activity and cellular function of ribosome-associated *Escherichia coli* EngA. *J. Bacteriol.* **188**, 7992–7996 (2006).
192. Tomar, S. K., Dhimole, N., Chatterjee, M. & Prakash, B. Distinct GDP/GTP bound states of the tandem G-domains of EngA regulate ribosome binding. *Nucleic Acids Res.* **37**, 2359–2370 (2009).
193. Majumdar, S., Acharya, A., Tomar, S. K. & Prakash, B. Disrupting domain-domain interactions is indispensable for EngA-ribosome interactions. *Biochim. Biophys. Acta - Proteins Proteomics* **1865**, 289–303 (2017).
194. Muench, S. P., Xu, L., Sedelnikova, S. E. & Rice, D. W. The essential GTPase YphC displays a major domain rearrangement associated with nucleotide binding. *Proc. Natl. Acad. Sci. U. S. A.* **103**, 12359–12364 (2006).
195. Inoue, K., Alsina, J., Chen, J. & Inouye, M. Suppression of defective ribosome assembly in a *rbfA* deletion mutant by overexpression of Era, an essential GTPase in *Escherichia coli*. *Mol. Microbiol.* **48**, 1005–1016 (2003).
196. Sayed, A., Matsuyama, S. I. & Inouye, M. Era, an essential *Escherichia coli* small G-protein, binds to the 30S ribosomal subunit. *Biochem. Biophys. Res. Commun.* **264**, 51–54 (1999).
197. Razi, A., Guarné, A. & Ortega, J. The cryo-EM structure of YjeQ bound to the 30S subunit suggests a fidelity checkpoint function for this protein in ribosome assembly. *Proc. Natl. Acad. Sci. U. S. A.* **114**, E3396–E3403 (2017).
198. Daigle, D. M. *et al.* YjeQ, an essential, conserved, uncharacterized protein from *Escherichia coli*, is an unusual GTPase with circularly permuted G-motifs and marked burst kinetics. *Biochemistry* **41**, 11109–11117 (2002).
199. Daigle, D. M. & Brown, E. D. Studies of the Interaction of *Escherichia coli* YjeQ with the Ribosome In Vitro. *J. Bacteriol.* **186**, 1381–1387 (2004).
200. Pedro Lopez-Alonso, J. *et al.* RsgA couples the maturation state of the 30S ribosomal decoding center to activation of its GTPase pocket. *Nucleic Acids Res.* **45**, 6945–6959 (2017).
201. Rocchio, S. *et al.* Structural and functional investigation of the Small Ribosomal Subunit Biogenesis GTPase A (RsgA) from *Pseudomonas aeruginosa*. *FEBS J.* **286**, 4245–4260 (2019).
202. Guo, Q. *et al.* Structural basis for the function of a small GTPase RsgA on the 30S ribosomal subunit maturation revealed by cryoelectron microscopy. *Proc. Natl. Acad. Sci. U. S. A.* **108**,

- 13100–13105 (2011).
203. Goto, S., Kato, S., Kimura, T., Muto, A. & Himeno, H. RsgA releases RbfA from 30S ribosome during a late stage of ribosome biosynthesis. *EMBO J.* **30**, 104–114 (2011).
 204. Campbell, T. L. & Brown, E. D. Genetic interaction screens with ordered overexpression and deletion clone sets implicate the Escherichia coli GTPase YjeQ in late ribosome biogenesis. *J. Bacteriol.* **190**, 2537–2545 (2008).
 205. Himeno, H., Hanawa-Suetsugu, K., ... T. K.-N. A. & 2004, undefined. A novel GTPase activated by the small subunit of ribosome. *academic.oup.com*.
 206. Anand, B., Surana, P., Bhogaraju, S., Pahari, S. & Prakash, B. Circularly permuted GTPase YqeH binds 30S ribosomal subunit: Implications for its role in ribosome assembly. *Biochem. Biophys. Res. Commun.* **386**, 602–606 (2009).
 207. Uicker, W. C., Schaefer, L., Koenigsnecht, M. & Britton, R. A. The essential GTPase YqeH is required for proper ribosome assembly in Bacillus subtilis. *J. Bacteriol.* **189**, 2926–2929 (2007).
 208. Guo, Q. *et al.* Dissecting the in vivo assembly of the 30S ribosomal subunit reveals the role of RimM and general features of the assembly process. *Nucleic Acids Res.* **41**, 2609–2620 (2013).
 209. Leong, V., Kent, M., Jomaa, A. & Ortega, J. Escherichia coli rimM and yjeQ null strains accumulate immature 30S subunits of similar structure and protein complement. *RNA* **19**, 789–802 (2013).
 210. Thurlow, B. *et al.* Binding properties of YjeQ (RsgA), RbfA, RimM and Era to assembly intermediates of the 30S subunit. *Nucleic Acids Res.* **44**, 9918–9932 (2016).
 211. Bryant, R. E. & Sypherd, P. S. Genetic analysis of cold sensitive ribosome maturation mutants of Escherichia coli. *J. Bacteriol.* **117**, 1082–1092 (1974).
 212. Caldas, T. *et al.* The FtsJ/RrmJ heat shock protein of Escherichia coli is a 23 S ribosomal RNA methyltransferase. *J. Biol. Chem.* **275**, 16414–16419 (2000).
 213. Bügl, H. *et al.* RNA methylation under heat shock control. *Mol. Cell* **6**, 349–360 (2000).
 214. Caldas, T., Binet, E., Bouloc, P. & Richarme, G. Translational defects of Escherichia coli mutants deficient in the Um2552 23S ribosomal RNA methyltransferase RrmJ/FTSJ. *Biochem. Biophys. Res. Commun.* **271**, 714–718 (2000).
 215. Pardo, D. & Rosset, R. A new ribosomal mutation which affects the two ribosomal subunits in Escherichia coli. *MGG Mol. Gen. Genet.* **153**, 199–204 (1977).
 216. Davis, J. H. *et al.* Modular Assembly of the Bacterial Large Ribosomal Subunit. *Cell* **167**, 1610–1622.e15 (2016).
 217. Jiang, M. *et al.* Identification of novel Escherichia coli ribosome-associated proteins using isobaric tags and multidimensional protein identification techniques. *J. Bacteriol.* **189**, 3434–3444 (2007).
 218. Hayes, F. & Hayes, D. H. Biosynthesis of ribosomes in E. coli. I. - Properties of ribosomal precursor particles and their RNA components. *Biochimie* **53**, 369–382 (1971).
 219. Mulder, A. M. *et al.* Visualizing ribosome biogenesis: Parallel assembly pathways for the 30S subunit. *Science (80-.)*. **330**, 673–677 (2010).
 220. Nikolay, R. *et al.* Structural Visualization of the Formation and Activation of the 50S Ribosomal

- Subunit during In Vitro Reconstitution. *Mol. Cell* **70**, 881-893.e3 (2018).
221. Jomaa, A. *et al.* Understanding ribosome assembly: The structure of in vivo assembled immature 30S subunits revealed by cryo-electron microscopy. *RNA* **17**, 697–709 (2011).
 222. Jomaa, A. *et al.* Cryo-electron microscopy structure of the 30S subunit in complex with the YjeQ biogenesis factor. *RNA* **17**, 2026–2038 (2011).
 223. Yang, Z. *et al.* Structural insights into the assembly of the 30S ribosomal subunit in vivo: functional role of S5 and location of the 17S rRNA precursor sequence. doi:10.1007/s13238-014-0044-1.
 224. Sharma, M. R. *et al.* Interaction of Era with the 30S ribosomal subunit: Implications for 30S subunit assembly. *Mol. Cell* **18**, 319–329 (2005).
 225. Stokes, J. M., Davis, J. H., Mangat, C. S., Williamson, J. R. & Brown, E. D. Discovery of a small molecule that inhibits bacterial ribosome biogenesis. *Elife* **3**, e03574 (2014).
 226. Kummer, E. & Ban, N. Mechanisms and regulation of protein synthesis in mitochondria. *Nat. Rev. Mol. Cell Biol.* **0123456789**, 1–19 (2021).
 227. Antonicka, H. & Shoubridge, E. A. Mitochondrial RNA Granules Are Centers for Posttranscriptional RNA Processing and Ribosome Biogenesis. *Cell Rep.* **10**, 920–932 (2015).
 228. Bogenhagen, D. F., Martin, D. W. & Koller, A. Initial steps in RNA processing and ribosome assembly occur at mitochondrial DNA nucleoids. *Cell Metab.* **19**, 618–629 (2014).
 229. Rackham, O. *et al.* Hierarchical RNA Processing Is Required for Mitochondrial Ribosome Assembly. *Cell Rep.* **16**, 1874–1890 (2016).
 230. Bogenhagen, D. F., Ostermeyer-Fay, A. G., Haley, J. D. & Garcia-Diaz, M. Kinetics and Mechanism of Mammalian Mitochondrial Ribosome Assembly. *Cell Rep.* **22**, 1935–1944 (2018).
 231. Zeng, R., Smith, E. & Barrientos, A. Yeast Mitoribosome Large Subunit Assembly Proceeds by Hierarchical Incorporation of Protein Clusters and Modules on the Inner Membrane. *Cell Metab.* **27**, 645-656.e7 (2018).
 232. Chen, H. *et al.* The human mitochondrial 12S rRNA m4C methyltransferase METTL15 is required for mitochondrial function. *J. Biol. Chem.* **295**, 8505–8513 (2020).
 233. Haute, L. Van *et al.* METTL15 introduces N4-methylcytidine into human mitochondrial 12S rRNA and is required for mitoribosome biogenesis. *Nucleic Acids Res.* **47**, 10267–10281 (2019).
 234. Sirum-Connolly, K. & Mason, T. L. Functional requirement of a site-specific ribose methylation in ribosomal RNA. *Science (80-.).* **262**, 1886–1889 (1993).
 235. Lee, K.-W. W. & Bogenhagen, D. F. Assignment of 2'-O-Methyltransferases to Modification Sites on the Mammalian Mitochondrial Large Subunit 16 S Ribosomal RNA (rRNA)*. *J. Biol. Chem.* **289**, 24936–24942 (2014).
 236. Pintard, L., Bujnicki, J. M., Lapeyre, B. & Bonnerot, C. MRM2 encodes a novel yeast mitochondrial 21s rRNA methyltransferase. *EMBO J.* **21**, 1139–1147 (2002).
 237. Rorbacha, J. *et al.* MRM2 and MRM3 are involved in biogenesis of the large subunit of the mitochondrial ribosome. *Mol. Biol. Cell* **25**, 2542–2555 (2014).
 238. Lee, K. W., Okot-Kotber, C., La Comb, J. F. & Bogenhagen, D. F. Mitochondrial ribosomal RNA (rRNA) methyltransferase family members are positioned to modify nascent rRNA in foci

- near the mitochondrial DNA nucleoid. *J. Biol. Chem.* **288**, 31386–31399 (2013).
239. Bar-Yaacov, D. *et al.* Mitochondrial 16S rRNA Is Methylated by tRNA Methyltransferase TRMT61B in All Vertebrates. *PLoS Biol.* **14**, e1002557 (2016).
240. Liu, X. *et al.* Structural insights into dimethylation of 12S rRNA by TFB1M: indispensable role in translation of mitochondrial genes and mitochondrial function. *Nucleic Acids Res.* **47**, 7648–7665 (2019).
241. Metodiev, M. D. *et al.* Methylation of 12S rRNA Is Necessary for In Vivo Stability of the Small Subunit of the Mammalian Mitochondrial Ribosome. *Cell Metab.* **9**, 386–397 (2009).
242. Seidel-Rogol, B. L., McCulloch, V. & Shadel, G. S. Human mitochondrial transcription factor B1 methylates ribosomal RNA at a conserved stem-loop. *Nat. Genet.* **33**, 23–24 (2003).
243. Metodiev, M. D. *et al.* NSUN4 Is a Dual Function Mitochondrial Protein Required for Both Methylation of 12S rRNA and Coordination of Mitoribosomal Assembly. *PLoS Genet.* **10**, 1–11 (2014).
244. Cámara, Y. *et al.* MTERF4 Regulates Translation by Targeting the Methyltransferase NSUN4 to the Mammalian Mitochondrial Ribosome. *Cell Metab.* **13**, 527–539 (2011).
245. Zaganelli, S. *et al.* The pseudouridine synthase RPU4 is an essential component of mitochondrial RNA granules. *J. Biol. Chem.* **292**, 4519–4532 (2017).
246. Antonicka, H. *et al.* A pseudouridine synthase module is essential for mitochondrial protein synthesis and cell viability. *EMBO Rep.* **18**, 28–38 (2017).
247. Busch, J. D. *et al.* MitoRibo-Tag Mice Provide a Tool for In Vivo Studies of Mitoribosome Composition. *Cell Rep.* **29**, 1728–1738.e9 (2019).
248. Tu, Y. T. & Barrientos, A. The Human Mitochondrial DEAD-Box Protein DDX28 Resides in RNA Granules and Functions in Mitoribosome Assembly. *Cell Rep.* **10**, 854–864 (2015).
249. De Silva, D., Fontanesi, F. & Barrientos, A. The DEAD box protein Mrh4 functions in the assembly of the mitochondrial large ribosomal subunit. *Cell Metab.* **18**, 712–725 (2013).
250. Kotani, T., Akabane, S., Takeyasu, K., Ueda, T. & Takeuchi, N. Human G-proteins, ObgH1 and Mtg1, associate with the large mitochondrial ribosome subunit and are involved in translation and assembly of respiratory complexes. *Nucleic Acids Res.* **41**, 3713–3722 (2013).
251. Kim, H.-J. J. & Barrientos, A. MTG1 couples mitoribosome large subunit assembly with intersubunit bridge formation. *Nucleic Acids Res.* **46**, 8435–8453 (2018).
252. Hirano, Y., Ohniwa, R. L., Wada, C., Yoshimura, S. H. & Takeyasu, K. Human small G proteins, ObgH1, and ObgH2, participate in the maintenance of mitochondria and nucleolar architectures. *Genes to Cells* **11**, 1295–1304 (2006).
253. Datta, K., Fuentes, J. L. & Maddock, J. R. The yeast GTPase Mtg2p is required for mitochondrial translation and partially suppresses an rRNA methyltransferase mutant, mrm2. *Mol. Biol. Cell* **16**, 954–963 (2005).
254. Kehrein, K. *et al.* Organization of Mitochondrial Gene Expression in Two Distinct Ribosome-Containing Assemblies. *Cell Rep.* **10**, 843–853 (2015).
255. Maiti, P., Antonicka, H., Gingras, A. C., Shoubbridge, E. A. & Barrientos, A. Human GTPBP5 (MTG2) fuels mitoribosome large subunit maturation by facilitating 16S rRNA methylation. *Nucleic Acids Res.* **48**, 7924–7943 (2020).
256. Cipullo, M. *et al.* Human GTPBP5 is involved in the late stage of mitoribosome large subunit

- assembly. *Nucleic Acids Res.* **49**, gkaa1131-- (2020).
257. Lavdovskaia, E. *et al.* Dual function of GTPBP6 in biogenesis and recycling of human mitochondrial ribosomes. *Nucleic Acids Res.* **48**, 12929–12942 (2020).
258. Maiti, P., Kim, H.-J. J., Tu, Y.-T. T. & Barrientos, A. Human GTPBP10 is required for mitoribosome maturation. *Nucleic Acids Res.* **46**, 11423–11437 (2018).
259. Lavdovskaia, E. *et al.* The human Obg protein GTPBP10 is involved in mitoribosomal biogenesis. *Nucleic Acids Res.* **46**, gky701-- (2018).
260. Kolanczyk, M. *et al.* NOA1 is an essential GTPase required for mitochondrial protein synthesis. *Mol. Biol. Cell* **22**, 1–11 (2011).
261. He, J. *et al.* Human C4orf14 interacts with the mitochondrial nucleoid and is involved in the biogenesis of the small mitochondrial ribosomal subunit. *Nucleic Acids Res.* **40**, 6097–6108 (2012).
262. Paul, M. F., Alushin, G. M., Barros, M. H., Rak, M. & Tzagoloff, A. The putative GTPase encoded by MTG3 functions in a novel pathway for regulating assembly of the small subunit of yeast mitochondrial ribosomes. *J. Biol. Chem.* **287**, 24346–24355 (2012).
263. Uchiumi, T. *et al.* ERAL1 is associated with mitochondrial ribosome and elimination of ERAL1 leads to mitochondrial dysfunction and growth retardation. *Nucleic Acids Res.* **38**, 5554–5568 (2010).
264. Dennerlein, S., Rozanska, A., Wydro, M., Chrzanowska-Lightowlers, Z. M. A. & Lightowlers, R. N. Human ERAL1 is a mitochondrial RNA chaperone involved in the assembly of the 28S small mitochondrial ribosomal subunit. *Biochem. J.* **430**, 551–558 (2010).
265. Rozanska, A. *et al.* The human RNA-binding protein RBFA promotes the maturation of the mitochondrial ribosome. *Biochem. J.* **474**, 2145–2158 (2017).
266. Rorbach, J., Gammage, P. A. & Minczuk, M. C7orf30 is necessary for biogenesis of the large subunit of the mitochondrial ribosome. *Nucleic Acids Res.* **40**, 4097–4109 (2012).
267. Wanschers, B. F. J. *et al.* C7orf30 specifically associates with the large subunit of the mitochondrial ribosome and is involved in translation. *Nucleic Acids Res.* **40**, 4040–4051 (2012).
268. Brown, A. *et al.* Structures of the human mitochondrial ribosome in native states of assembly. *Nat. Struct. Mol. Biol.* **24**, 866–869 (2017).
269. Wredenberg, A. *et al.* MTERF3 Regulates Mitochondrial Ribosome Biogenesis in Invertebrates and Mammals. *PLoS Genet.* **9**, (2013).
270. Perks, K. L. *et al.* PTCD1 Is Required for 16S rRNA Maturation Complex Stability and Mitochondrial Ribosome Assembly. *Cell Rep.* **23**, 127–142 (2018).
271. Summer, S. *et al.* YBEY is an essential biogenesis factor for mitochondrial ribosomes. *Nucleic Acids Res.* **48**, 9762–9786 (2020).
272. Hillman, G. A. & Henry, M. F. The yeast protein Mam33 functions in the assembly of the mitochondrial ribosome. *J. Biol. Chem.* **294**, 9813–9829 (2019).
273. Roloff, G. A. & Henry, M. F. Mam33 promotes cytochrome c oxidase subunit i translation in *Saccharomyces cerevisiae* mitochondria. *Mol. Biol. Cell* **26**, 2885–2894 (2015).
274. Dalla Rosa, I. *et al.* MPV17L2 is required for ribosome assembly in mitochondria. *Nucleic Acids Res.* **42**, 8500–8515 (2014).

275. Szczepanowska, K. *et al.* CLPP coordinates mitoribosomal assembly through the regulation of ERAL 1 levels. *EMBO J.* **35**, 2566–2583 (2016).
276. Rötig, A. Human diseases with impaired mitochondrial protein synthesis. *Biochimica et Biophysica Acta - Bioenergetics* vol. 1807 1198–1205 (2011).
277. Boczonadi, V. & Horvath, R. Mitochondria: Impaired mitochondrial translation in human disease. *Int. J. Biochem. & Cell Biol.* **48**, 77–84 (2014).
278. Boczonadi, V., Ricci, G. & Horvath, R. Mitochondrial DNA transcription and translation: Clinical syndromes. *Essays in Biochemistry* vol. 62 321–340 (2018).
279. Jacobs, H. T. & Turnbull, D. M. Nuclear genes and mitochondrial translation: A new class of genetic disease. *Trends in Genetics* vol. 21 312–314 (2005).
280. Kim, H.-J. J., Maiti, P. & Barrientos, A. Mitochondrial ribosomes in cancer. *Semin. Cancer Biol.* **47**, 67–81 (2017).
281. Singh, R., Sripada, L. & Singh, R. Side effects of antibiotics during bacterial infection: Mitochondria, the main target in host cell. *Mitochondrion* **16**, 50–54 (2014).
282. Lopez Sanchez, M. I. G., Krüger, A., Shiriaev, D. I., Liu, Y. & Rorbach, J. Human mitoribosome biogenesis and its emerging links to disease. *International Journal of Molecular Sciences* vol. 22 3827 (2021).
283. Nikolay, R. *et al.* Snapshots of native pre-50S ribosomes reveal a biogenesis factor network and evolutionary specialization. *Mol. Cell* **81**, 1200--1215.e9 (2021).
284. Cheng, J., Berninghausen, O. & Beckmann, R. A distinct assembly pathway of the human 39S late pre-mitoribosome. *bioRxiv* 2021.03.17.435838 (2021) doi:10.1101/2021.03.17.435838.
285. Saurer, M. *et al.* Mitoribosomal small subunit biogenesis in trypanosomes involves an extensive assembly machinery. *Science (80-.)*. **365**, 1144–1149 (2019).
286. Kühlbrandt, W. The resolution revolution. *Science* vol. 343 1443–1444 (2014).
287. Su, C. C. *et al.* A ‘Build and Retrieve’ methodology to simultaneously solve cryo-EM structures of membrane proteins. *Nat. Methods* **18**, 69–75 (2021).
288. Verbeke, E. J., Mallam, A. L., Drew, K., Marcotte, E. M. & Taylor, D. W. Classification of Single Particles from Human Cell Extract Reveals Distinct Structures. *CellReports* **24**, 259-268.e3 (2018).
289. Rickgauer, J. P., Grigorieff, N. & Denk, W. Single-protein detection in crowded molecular environments in cryo-EM images. *Elife* **6**, (2017).
290. Jaskolowski, M. *et al.* Structural Insights into the Mechanism of Mitoribosomal Large Subunit Biogenesis. *Mol. Cell* **79**, 629--644.e4 (2020).
291. Lenarčič, T. *et al.* Stepwise maturation of the peptidyl transferase region of human mitoribosomes. *Nat. Commun.* **12**, 3671 (2021).
292. Weissenberger, G., Henderikx, R. J. M. & Peters, P. J. Understanding the invisible hands of sample preparation for cryo-EM. *Nature Methods* vol. 18 463–471 (2021).
293. Ravelli, R. B. G. *et al.* Cryo-EM structures from sub-nl volumes using pin-printing and jet vitrification. *Nat. Commun.* **11**, 1–9 (2020).
294. Arnold, S. A. *et al.* Blotting-free and lossless cryo-electron microscopy grid preparation from nanoliter-sized protein samples and single-cell extracts. *J. Struct. Biol.* **197**, 220–226 (2017).

295. Taylor, K. A. & Glaeser, R. M. Retrospective on the early development of cryoelectron microscopy of macromolecules and a prospective on opportunities for the future. *J. Struct. Biol.* **163**, 214–223 (2008).
296. Doerr, A. Cryo-electron tomography. *Nature Methods* vol. 14 34 (2016).
297. Wan, W. & Briggs, J. A. G. Cryo-Electron Tomography and Subtomogram Averaging. in *Methods in Enzymology* vol. 579 329–367 (Academic Press Inc., 2016).
298. Tegunov, D., Xue, L., Dienemann, C., Cramer, P. & Mahamid, J. Multi-particle cryo-EM refinement with M visualizes ribosome-antibiotic complex at 3.5 Å in cells. *Nat. Methods* **18**, 186–193 (2021).
299. Dubochet, J. & McDowell, A. W. VITRIFICATION OF PURE WATER FOR ELECTRON MICROSCOPY. *J. Microsc.* **124**, 3–4 (1981).
300. Crowther RA, Derosier DJ & Klug A. Reconstruction of a Three-Dimensional Structure From Projection and Its Application To Electron Microscopy. *Proc. R. Soc. London. A. Math. Phys. Sci.* **317**, 319–340 (1970).
301. Van Heel, M. & Frank, J. Use of multivariate statistics in analysing the images of biological macromolecules. *Ultramicroscopy* **6**, 187–194 (1981).
302. Frank, J., Shimkin, B. & Dowse, H. Spider—A modular software system for electron image processing. *Ultramicroscopy* **6**, 343–357 (1981).
303. Krivanek, O. L. & Mooney, P. E. Applications of slow-scan CCD cameras in transmission electron microscopy. *Ultramicroscopy* **49**, 95–108 (1993).
304. Greber, B. J. *et al.* The complete structure of the large subunit of the mammalian mitochondrial ribosome. *Nat.* 2014 5157526 **515**, 283–286 (2014).
305. Allegretti, M., Mills, D. J., McMullan, G., Kühlbrandt, W. & Vonck, J. Atomic model of the F420-reducing [NiFe] hydrogenase by electron cryo-microscopy using a direct electron detector. *Elife* **3**, (2014).
306. Liao, M., Cao, E., Julius, D. & Cheng, Y. Structure of the TRPV1 ion channel determined by electron cryo-microscopy. *Nat.* 2013 5047478 **504**, 107–112 (2013).
307. Herzik, M. A., Wu, M. & Lander, G. C. High-resolution structure determination of sub-100 kDa complexes using conventional cryo-EM. *Nat. Commun.* **10**, 1–9 (2019).
308. Yip, K. M., Fischer, N., Paknia, E., Chari, A. & Stark, H. Atomic-resolution protein structure determination by cryo-EM. *Nature* **587**, 157–161 (2020).
309. Nakane, T. *et al.* Single-particle cryo-EM at atomic resolution. *Nature* **587**, 152–156 (2020).
310. Renaud, J. P. *et al.* Cryo-EM in drug discovery: Achievements, limitations and prospects. *Nature Reviews Drug Discovery* vol. 17 471–492 (2018).

CURRICULUM VITAE

CV removed from online version

Protection of personal data

CV removed from online version

Protection of personal data